Monitoring Global Lightning and the Lower Ionosphere with Schumann Resonances

Doctoral Dissertation

Tamás Bozóki

University of Szeged

Supervisors:

Gabriella Sátori DSc
Research Professor Emeritus, Institute of Earth Physics and Space Science (ELKH EPSS)

Gábor Szabó DSc
Professor, Department of Optics and Quantum Electronics, University of Szeged

University of Szeged, Faculty of Science and Informatics
Doctoral School of Physics

Szeged
2022

Contents

1 Introduction

1.1 The Schumann Resonance Phenomenon

The Earth's surface and the lower ionosphere together form an electromagnetic cavity resonator with resonance frequencies in the extremely low frequency (ELF, 3 Hz–3 kHz) band at ∼8, ∼14, ∼20, ∼26 Hz etc. (Balser and Wagner, 1960; Galejs, 1972; Madden and Thompson, 1965; Nickolaenko and Hayakawa, 2002; Price, 2016; Wait, 1996). These resonances are named after Winfried Otto Schumann who described them theoretically in 1952 (Schumann, 1952), 8 years before full frequency spectra were actually observed by Balser and Wagner (1960). Schumann resonances (SRs) are excited primarily by lightning-radiated electromagnetic (EM) waves and the approximate number of 30–100 lightning strokes per second worldwide (Christian et al., 2003) maintains the resonance field quasi-continuously. It follows that SRs are excellent indicators of lightning activity and distribution on global scales (e.g., Boldi et al., 2018; Dyrda et al., 2014; Satori and Zieger, 1999; Williams et al., 2021; Williams and Satori, 2004) and they are also known as important source of information about the global state of the lowest part of the ionosphere (e.g., Dyrda et al., 2015; Kudintseva et al., 2018; Nickolaenko et al., 2012; Roldugin et al., 2004b, 2003; Satori et al., 2007, 2016; Shvets et al., 2017). The possible connection between atmospheric electricity (including SRs) and biological systems is another topic with substantial scientific interest (e.g., Elhalel et al., 2019; Price et al., 2021; Sukhov et al., 2021) and recently, major scientific interest arose for SRs in connection with gravitational wave detection (e.g., Coughlin et al., 2016, 2018; Kowalska-Leszczynska et al., 2017).

Essentially, it is the very weak attenuation rate (about 0.5 dB/Mm; Chapman et al., 1966; Wait, 1996) of EM waves in the lowest part of the ELF band (<100 Hz) that enables the formation of SRs. Lightning radiated EM waves can travel a number of times around the globe before losing most of their energy and the constructive interference of the waves propagating in the opposite directions (direct and antipodal waves) form the resonance structure. Most of the lightning strokes contribute to a quasi-steady "background" field in which the overlapping pulses cannot be distinguished. On the other hand, SR transients (or Q-bursts) generated by exceptionally large lightning strokes (Boccippio et al., 1995; Guha et al., 2017; Ogawa et al., 1967) can be identified on an individual basis from ELF records in the time domain, as they can largely exceed the average background signal strength. Fig. 1 demonstrates how a typical spectrum in the lowest part of the ELF band look like.

Much published material has appeared in the literature describing the standard (recurrent) daily and seasonal variations of SR spectral parameters (modal

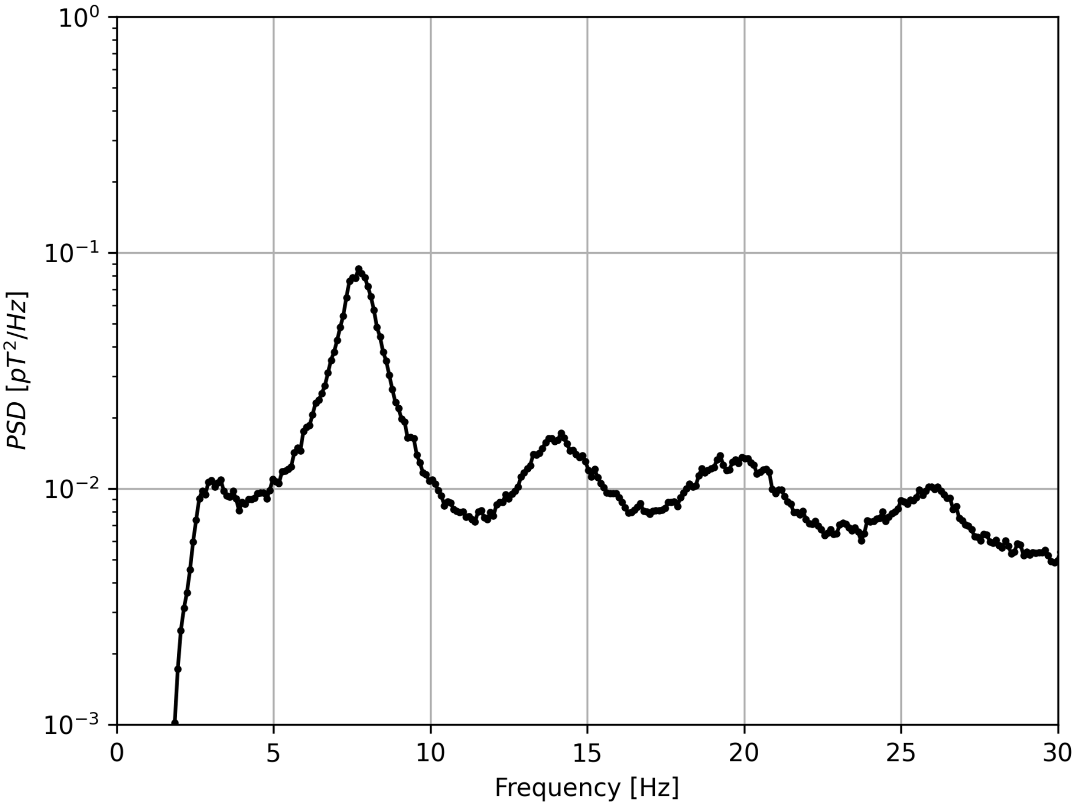

Figure 1: Power spectral density (PSD) spectrum of the magnetic field measured at Hornsund (Svalbard) on the 15^{th} of January 2019 between 2 and 3 UT.

frequency, intensity and sharpness of maxima) at different stations (e.g., Fornieles-Callejón et al., 2015; Manu et al., 2015; Musur and Beggan, 2019; Nickolaenko and Hayakawa, 2014, 2002; Ondrásková et al., 2007; Price and Melnikov, 2004; Roldugin et al., 2004a; Satori, 1996; Tatsis et al., 2020; Toledo-Redondo et al., 2012a; Zhou et al., 2013). These standard variations in SRs are mainly the consequence of the daily and seasonal variations of global lightning activity which fundamentally affect the observed SR spectral parameters (Satori, 1996). On the other hand, standard variations in SRs are also connected to the effect of the day-night terminator, i.e., to changes in the shape of the Earth–ionosphere cavity (Melnikov et al., 2004; Pracser et al., 2021; Satori et al., 2007). The cause of this asymmetry is that the ionization sources (Lyman-series, UV, EUV, X-ray) on the sunlit side are missing in the nightside hemisphere and the characteristic height of the cavity increases due to the high neutralization rate (Thomas, 1971). SR measurements demonstrated that the characteristic variations of global lightning activity are highly recurrent on a day-to-day and year-to-year basis (see e.g., Satori, 1996) which was confirmed by optical observations of lightning from space as well (Christian et al., 2003; Williams et al., 2000).

Occasional variations in SRs have also been documented, which are partly connected to transient extra-terrestrial phenomena that can modify the shape of the Earth–ionosphere cavity and thereby to "untune" its resonance frequencies. It is important to note that as a consequence of any change in the shape of the Earth–ionosphere cavity all the resonance frequencies shift in the same direction at all stations on Earth, but whether they increase or decrease depends on the actual modification of the conductivity profile in the upper atmosphere (Kudintseva et al., 2018; Satori et al., 2016; Zhou and Qiao, 2015). Solar X-ray bursts (Dyrda et al., 2015; Roldugin et al., 2004b; Satori et al., 2005, 2016; Shvets et al., 2017) and solar proton events (Roldugin et al., 2003; Schlegel and Füllekrug, 1999; Singh et al., 2014) are known to cause such changes in frequencies (of both signs). Occasional variations in SR intensity with extra-terrestrial origin have been associated only with solar proton events (Roldugin et al., 2003; Schlegel and Füllekrug, 1999), and recently, indication for periods with increased SR intensity during geomagnetic storms was demonstrated as well (Pazos et al., 2019; Salinas et al., 2016). SR measurements can be used to collect additional information about these space weather phenomena. We note that variations in SRs were also reported connected to seismic activity (e.g., Christofilakis et al., 2019; Galuk et al., 2019; Hayakawa et al., 2020).

1.2 Schumann Resonance Measurements in the SZIGO

In this section we introduce the SR measurements operating in the Széchenyi István Geophysical Observatory (SZIGO) in Hungary based on Satori et al. (1996), Satori et al. (2013) and Bor et al. (2020). The SR measurements in the SZIGO will be used in this dissertation to study the El Niño–Southern Oscillation (ENSO) phenomenon (see Section 4).

The SZIGO, also known as the Nagycenk Geophysical Observatory (NCK), was founded during the International Geophysical Year in 1957-58, as a dedicated research infrastructure for monitoring EM phenomena related to the solid Earth, upper atmosphere and near-Earth space. The observatory is situated on a sedimentary formation embedded in woodland near Lake Fertő inside the area of a nature reserve (47°38' N, 16°43′ E, 153.7 m m.s.l.).

Antal Ádám and Pál Bencze made the first efforts to study the variations of natural EM fields in the SR band at fixed frequencies (8 Hz, 21 Hz, 86 Hz) in the 1960s using an L antenna, an amplifier built by Pál Bencze and a studio tape recorder (Ádám and Bencze, 1963). At the end of the 1980s, Gabriella Sátori suggested that SRs could be observed continuously owing to the explosive development of computational capacities. Test measurements begun in 1988 aimed to observe the first SR mode in the vertical electric field (Satori, 1989). The old L antenna and the amplifier was used with a new digital data collector developed at the technical university in Budapest. Gabriella Sátori reported on the first scientific results in

1992 in Hungary (Satori, 1992) and in 1993 at the International Association of Geomagnetism and Aeronomy (IAGA) conference in Buenos Aires (Satori, 1993). Yet in 1993, a completely new recording system for SR measurements was installed with a mechanically more stable ball-antenna (Fig. 2a). This enabled the regular registration of SR spectral parameters from May onwards (Satori et al., 1996). The metal ball on the top of the antenna is an aluminium casting, weighs around 20 kg, and has a diameter of about 45 cm. It is placed on a 2.4 m high mount prepared from ceramics and a special insulating plastic material. Two large copper plates buried under the antenna assure the grounding of the system. The total weight of the antenna is quite large, around 200 kg, in order to attenuate its mechanical vibrations. The antenna was placed in an open flat area with well-kept grass, as far from the surrounding trees as was possible.

Figure 2: **On the left**: Electric ball antenna. **On the right**: The calibration of the electric ball antenna on the 20th December, 2013.

The preamplifier with an amplification coefficient of 700 can be found just at the bottom of the antenna inside a waterproof box. Here the power line frequency of 50 Hz and its third harmonic (150 Hz) are attenuated by 50 and 30 dB, respectively. The main amplifier is in the recording building with changeable settings, which makes it possible to increase the amplification further by 2 orders of magnitude. It assures an additional attenuation of 30 dB at 50 Hz which means altogether 80 dB suppression of the power line frequency. An analogue-to-digital converter transforms the signal into digital records with values between ±2.5 V. The effective bandwidth of the antenna is 5 to 30 Hz.

The so called complex demodulation algorithm has been applied as an on-site data processing method to extract the modal frequency and the amplitude of the first three resonance modes on a quasi-continuous basis (Satori et al., 1996). This spectral processing technique works in the time domain and computes the spectral parameters with high time resolution using time windows of ∼40 s. From the high-time-resolution data, the computer code determines hourly averages and corresponding standard deviations which are more often used for scientific purposes. Retrieved parameters are rejected in the case of locally disturbed conditions. Such parameters are not included in the hourly average values. In the first 10 years of operation, only the spectral parameters had been stored, and the time series were not kept due to the lack of enough storage capacity.

The electric antenna is calibrated using a wire gauze of 1 m^2 area mounted 1 m over its top (Fig. 2b). Calibration signals include monochromatic excitations with a given frequency to determine the sensitivity of the instrument. The electric field of the calibrating net is not homogeneous due to its finite size, and therefore the field appearing at the position of the ball antenna is calculated theoretically and numerically. In addition, short duration peaks are also sent to the net to determine the amplitude and phase characteristics of the recording system from the recorded impulse responses in the full frequency range.

In November 1996, the system was upgraded with induction coil magnetometers to also record the two horizontal magnetic components of the atmospheric electric field in the geographic north–south and east–west directions (Satori et al., 2007). The coils are located in a non-magnetic building of the observatory and are buried about 1 m below the ground. In order to minimize the effect of microseismic activity on the measurements, they were placed in concrete channels partially filled with sand. The applied spectral technique for signal processing is the same as for the vertical electric field component. The effective bandwidth of the whole system is roughly in the 5–30 Hz frequency range. Helmholtz coils in the "absolute house" of the observatory enable the calibration of the induction coils.

Unfortunately, due to the strong disturbing effect of railway lines which run near the observatory and have been electrified after the establishment of the observatory, the quality of the magnetic measurements is not good enough to extract high-quality spectral parameters of SRs. Nevertheless, the magnetic measurements can still be utilized to investigate SR transients. Parallel registration of the two horizontal magnetic and the vertical electric components enables the calculation of the horizontal projection of the Poynting vector, which is an important property of transient signals. It is possible to estimate the location, polarity, and charge moment change of the source discharge from these measurements. From 1998, an additional unit receiving GPS signals provides timing information for the records.

In addition to the quasi-real-time calculated SR peak parameters, the digitized raw time series of the measured field components have also been saved since 2003, thanks to enormous improvements in data storage capacity. This important development enabled the investigation not only of background SRs but also of SR transients. Analogue signals are digitized and stored at about a 500 Hz sampling rate. This high rate of sampling enables fast processing of the data series in the time domain.

Because of the ageing of the system over the decades, occasional renovations were necessary. Grounding of the electric antenna was reinforced in 2012, and the insulating lower pillar of the antenna had to be replaced in April 2019. Recently, LEMI-120 type induction coils have been purchased to replace the old magnetic antennas, which were originally built at the institute and had been inherited from early magnetosonic experiments.

1.3 Motivation and Goals

In the first few decades of research on SRs, most of the work was theoretical and few observations were available to confirm or refute the theoretical results (Satori, 2011). Since the beginning of the 1990s, the scientific interest in SRs has increased significantly, partly due to the fact that researchers began to regard SRs not only as an object of research, but also as a tool for investigating other geophysical phenomena. Owing to the rapid development of large computer capacities and motivated by a fundamental Science article (Williams, 1992) many SR stations started to operate on a continuous basis worldwide which gave a new impetus for SR-related research.

Perhaps the two most important directions of SR research are the investigation of global lightning activity and large-scale changes in the state of the lower ionosphere. These two areas of research can by no means be considered independent, as the effects associated with them are present together in the SR data (along with other additional effects). To obtain reliable results on global lightning activity, one needs to be convinced of the stability of the Earth-ionosphere cavity resonator over the period of interest (or be able to eliminate the resulting effects) and one needs to know the lightning-related variations in SR records to infer changes in the state of the lower ionosphere. The present dissertation fits well into these two research objectives.

It is a long-sought goal of SR research to reconstruct (to invert) the intensity and distribution of global lightning activity based on SR measurements. There have been many attempts in this field in the past, but the methods developed have not really reached the point of application, like the investigation of specific scientific questions or quasi-real-time data provision. Even though there is a significant interest in investigating global lightning activity with climatological purposes, this is at present severely limited by the detection efficiency of available lightning monitoring technologies Williams and Mareev (2014). A geophysical inversion consists of two basic parts: the forward model and the inversion algorithm. In the present case, the forward model determines the SRs expected from a given distribution of global lightning activity, while the inversion algorithm reconstructs the global lightning distribution through iteration steps, which would produce SR spectra closest to the actual measurements. The main strength of this approach is that it does not suffer from detection efficiency problems as, due to the extremely weak attenuation of lightning radiated ELF waves, all lightning strokes with vertical extent contribute to the measured EM fields (this makes it well suitable for climatology-related studies). Based on a few distant observation sites on the globe the inversion algorithm determines the charge moment change distribution of lightning activity in the unit of $\mathrm{C}^2\,\mathrm{km}^2/\mathrm{s}$ which can be regarded as a new parameter characterising the global climate. Furthermore, it is to be emphasized that this approach gives the intensity of the general lightning activity in terms of an absolute physical unit not biased by artificial event selection as in case of statistics based on the number density of strokes or flashes. One of the main goals of my PhD work was to develop our own SR inversion model. Our achievements in this field are presented in the first part of this dissertation. Chapter 2 describes the forward models we apply, while Chapter 3 describes our inversion algorithm. Although the inversion has not been used routinely in our case, yet, the methodological development is essentially complete, so we can concentrate on its use in the forthcoming years.

The second part of the dissertation presents two separate studies. Chapter 4 demonstrates that SRs are a powerful tool to investigate global lightning activity even without the inversion, while Chapter 5 demonstrates how SR measurements can be used to investigate space weather related changes in the properties of the lower ionosphere. These investigations fit in well with the trend towards interpreting SR data from multiple stations together (rather than individually) to disclose globally detectable changes associated with large-scale processes. The application of the inversion is an important next goal for the El Niño–Southern Oscillation related study presented in Chapter 4, while the changes in the properties of the Earth-ionosphere cavity on the solar cycle timescale described in Chapter 5 represent a challenge for the SR inversion task as SR intensity changes associated with space weather phenomena needs to be removed (corrected) to get a realistic estimation for the intensity and distribution of global lightning activity.

2 Modeling Schumann Resonances

In the first section of this chapter theoretical descriptions of SRs are introduced which were originally presented in the papers by Bozoki et al. (2019); Prácser et al. (2019) and Pracser et al. (2021) which is followed by a section about the open source python package `schupy` introduced in Bozoki et al. (2019) and by a section that presents numerical validation tests of the described models following Pracser et al. (2021). It is to be noted that our models and validation tests have been also introduced in Hungarian in Pracser and Bozoki (2021). The described SR models will be applied in the next chapter, when the aim will be to reconstruct global lightning activity based on the inversion of SR measurements.

2.1 Theoretical Descriptions

Multiple approaches have been followed in the literature to calculate the electromagnetic field of a single lightning stroke propagating in the Earth-ionosphere waveguide. Here, following Madden and Thompson (1965), we mention three possible methods for the calculation:

- to regard the Earth-ionosphere cavity as a two-dimensional (2D) transmission line and to solve the telegraph equations,
- to solve the Maxwell equations in the space between the Earth and the ionosphere,
- and to use the equivalent circuit method.

In our work we followed the transmission surface approach.

In this section first the transmission surface approach is described and the 2D telegraph equation (TDTE) is formulated which is then solved for an ideal (lossless) case. Later, the solution is modified to take into consideration losses connected to the imperfect conductivity of the ionosphere and the conductance of air. These solutions are given for the uniform Earth-ionosphere cavity which is then followed by the description of an analytical and a numerical approach that can take into consideration the day-night asymmetry of the Earth-ionosphere cavity. Finally, we show how to model the incoherently superimposed EM field of multiple lightning sources.

2.1.1 The Transmission Surface Approach

Theoretical descriptions of SRs are most naturally formulated in spherical coordinates (r, θ, ϕ). In order to make the derivations more comprehensible the following notation conventions are used in this chapter:

- standard physical quantities (i.e. voltage, V, current, I, admittance, Y, etc.) are denoted by capital letters,
- the surface densities of the same quantities are denoted by calligraphic letters (e.g. $\mathcal{I}$, $\mathcal{Y}$),
- while linear densities are denoted by lowercase letters (e.g. i).

The radius of the Earth's surface is denoted by R and the height of the ionosphere by h. The solutions described here are given in the frequency domain and are based on the assumption that the time evolution of the EM fields can be separated from their spatial dependence, and takes the form of $\exp(j\omega t)$ with various ω frequencies, where j is the imaginary unit.

We assume in our theoretical approach that the Earth-ionosphere waveguide can be modeled as a 2D transmission surface which is a valid approximation, as the wavelengths of the guided waves are much longer than the distance between the Earth's surface and the ionosphere (Madden and Thompson, 1965). In a local treatment the transmission surface can be represented by elementary circuit components. These elementary components can be described by four quantities, namely $Y_{C/L}$ (admittance) and $Z_{C/L}$ (impedance), where C and L denote the capacitive and the inductive elements, respectively, and can be expressed in the following general form:

$$\begin{aligned} Y_{C/L} &= G_{C/L} + j \cdot B_{C/L} \ , \\ Z_{C/L} &= R_{C/L} + j \cdot X_{C/L} \ , \end{aligned} \tag{1}$$

where G is the conductance, B is the susceptance, R is the Ohmic resistance and X is the reactance.

From charge conservation on the surface, the divergence of the surface current density vector in the ionosphere can be written as:

$$\nabla \mathbf{i}(\phi,\theta) = \mathcal{I}_{\mathcal{S}} - \mathcal{Y}_C V(\phi,\theta) \ , \tag{2}$$

where $\mathcal{I}_S$ is the current density of the source, $\mathcal{Y}_C$ is the admittance per unit area and V is the electric potential between the ionosphere and the Earth's surface. An additional equation can be obtained from the differential Ohm's law:

$$\nabla V(\phi,\theta) = -\mathbf{i}(\phi,\theta) Z_L \ . \tag{3}$$

It follows that the natural variables of the transmission surface approach are the voltage (V) and the surface current density vector ($\mathbf{i}$), while the the electric and magnetic field components can be expressed as:

$$E_r = V/h \ , \quad H_\phi = -i_\theta \ , \quad H_\theta = i_\phi \ , \tag{4}$$

from V and $\mathbf{i}$ (Madden and Thompson, 1965).

Eqs. (2) and (3) can be combined to arrive at the 2D telegraph equation (TDTE):

$$-\nabla \frac{1}{Z_L} \nabla V(\phi,\theta) = \mathcal{I}_S - \mathcal{Y}_C V(\phi,\theta) \; . \tag{5}$$

This equation determines the 2D distribution of the $V(\phi,\theta)$ voltage at a given ω frequency. The following straightforward solution of the TDTE was first introduced in the paper by Bozoki et al. (2019).

2.1.2 Solution for the Ideal, Uniform Cavity

If we assume that the surface of the Earth and the ionosphere are perfect conductors and there is vacuum between them, the circuit parameters become:

$$\begin{aligned} Z_L &= j\omega L_0 \; , \quad R_L = 0 \; , \\ \mathcal{Y}_C &= j\omega \mathcal{C}_0 \; , \quad G_C = 0 \; , \end{aligned} \tag{6}$$

where $\mathcal{C}_0$ and L_0 denote the capacitance per unit area and inductance in the lossless case, respectively. In this subsection we also assume that the impedance and admittance are constants on the surface, i.e. a uniform Earth-ionosphere cavity is considered. In this case Eq. (5) simplifies to:

$$\Delta V(\phi,\theta) = -Z_L \mathcal{I}_S + Z_L \mathcal{Y}_C V(\phi,\theta) \; . \tag{7}$$

In order to find the solution for this equation, first we assume that the source term can be described by a vertical Dirac-δ current impulse (representing a single lightning stroke) and construct our coordinate system in a way that its North Pole coincides with the position of the source. Since the source is symmetric under rotations around the vertical axis in this case, the solution will be independent of the coordinate ϕ. A general potential on the surface of a sphere can be expressed as a linear combination of spherical harmonics. Due to rotational symmetry, the solution can be expressed in the form of:

$$V(\theta) = \sum_{n=0}^{\infty} V_n P_n(\cos\theta) \; , \tag{8}$$

where P_n is the Legendre polynomial of degree n. The Laplacian acts on the Legendre polynomials as:

$$\frac{1}{R^2 \sin\theta} \frac{\mathrm{d}}{\mathrm{d}\theta} \left(\sin\theta \frac{\mathrm{d}P_n(\cos\theta)}{\mathrm{d}\theta} \right) = -\frac{n(n+1)}{R^2} P_n(\cos\theta) \; , \tag{9}$$

Note, that by exchanging the variable θ to $x = \cos\theta$ we arrive at Legendre's equation, which is the defining equation of the Legendre polynomials. The source term can also be expressed using Legendre polynomials (see e.g., Bronshtein and Semendyayev, 1997, on the completeness of Legendre polynomials):

$$\mathcal{I}_S = \frac{I}{2\pi R^2} \delta(\theta) = \frac{I}{2\pi R^2} \sum_{n=0}^{\infty} \frac{2n+1}{2} P_n(\cos\theta) \; , \tag{10}$$

where I is the total current, which we get when integrating for the surface of the sphere. Inserting Eqs. (8) and (10) into Eq. (7) and using Eq. (9) we arrive at:

$$0 = \sum_{n=0}^{\infty} \left[Z_L \mathcal{Y}_C V_n + \frac{n(n+1)}{R^2} V_n - Z_L I \frac{2n+1}{4\pi R^2} \right] P_n(\cos\theta) \; . \tag{11}$$

Since the Legendre polynomials are linearly independent the solution can only be achieved trivially, i.e. when all coefficients are 0. Hence, solving for V_n and inserting it back into Eq. (8) we get:

$$V(\omega,\theta) = \frac{M Z_L}{4\pi h} \sum_{n=0}^{\infty} \frac{2n+1}{n(n+1) + \mathcal{Y}_C Z_L R^2} P_n(\cos\theta) \; , \tag{12}$$

where we introduced the notation $M = Ih$, which is the current moment of the lightning source. This way M becomes the source quantity, which is more suitable for generalized uses.

The generalized formula for arbitrary source (ϕ',θ') and observation (ϕ,θ) locations can easily be acquired by replacing $\cos\theta$ with $\cos\gamma$, where γ is the angle between the source and observation positions, and $\cos\gamma$ can be expressed in the following form:

$$\cos\gamma = \cos\theta \, \cos\theta' + \sin\theta \, \sin\theta' \, \cos(\phi - \phi') \; . \tag{13}$$

Using Eqs. (3) and (4) and the $\mathbf{B} = \mu\mathbf{H}$ relation, one can derive expressions for the components of magnetic induction:

$$B_\phi(\phi,\theta) = \frac{\mu}{R Z_L} \frac{\partial}{\partial\theta} V(\phi,\theta) \; , \qquad B_\theta(\phi,\theta) = -\frac{\mu}{R Z_L \sin\theta} \frac{\partial}{\partial\phi} V(\phi,\theta) \; . \tag{14}$$

Using these expressions as well as Eqs. (4) and (12) we can obtain the general equations for E_r, B_ϕ and B_θ:

$$E_r(\omega,\phi',\theta',\phi,\theta) = \frac{M Z_L}{4\pi h^2} \sum_{n=0}^{\infty} \frac{2n+1}{n(n+1) + \mathcal{Y}_C Z_L R^2} P_n(\cos\gamma) \; , \tag{15}$$

$$B_\phi(\omega,\phi',\theta',\phi,\theta) = \frac{\mu M}{4\pi R h} \frac{\partial\gamma}{\partial\theta} \sum_{n=0}^{\infty} \frac{2n+1}{n(n+1) + \mathcal{Y}_C Z_L R^2} P_n^1(\cos\gamma) \; , \tag{16}$$

$$B_\theta(\omega,\phi',\theta',\phi,\theta) = -\frac{\mu M}{4\pi R h \sin\theta} \frac{\partial\gamma}{\partial\phi} \sum_{n=0}^{\infty} \frac{2n+1}{n(n+1) + \mathcal{Y}_C Z_L R^2} P_n^1(\cos\gamma) \; , \tag{17}$$

where $\mathrm{d}P_n(\cos\gamma)/\mathrm{d}\gamma = P_n^1(\cos\gamma)$ are the first order associated Legendre polynomials.

2.1.3 Solution for the Lossy, Uniform Cavity

In a more realistic scenario the R_L resistance of the ionosphere and the G_C conductance of the air are not equal to zero as it has been assumed in Eq. (6). However, by simply assigning them nonzero values the elegant analytical formalism of Eqs. (15), (16) and (17) would not hold anymore. Therefore, following the method of Kirillov and Kopeykin (2002), we take the losses into account by introducing two complex equivalents for the altitudes of the transmission surface called the inductive (h_L) and capacitive (h_C) heights, defined by the following relations (see Greifinger and Greifinger, 1978; Madden and Thompson, 1965; Mushtak and Williams, 2002):

$$\mathcal{C} = \frac{\varepsilon}{h_C}\,, \qquad L = \mu h_L\,, \tag{18}$$

where

$$\mathcal{C} = \mathcal{C}_0 - \frac{j\mathcal{G}_C}{\omega}\,, \qquad L = L_0 - \frac{jR_L}{\omega}\,. \tag{19}$$

It follows that the capacitive admittance and the inductive impedance is also modified:

$$\mathcal{Y}_C = j\omega\mathcal{C}\,, \qquad Z_L = j\omega L\,, \tag{20}$$

and hence, the following relation holds:

$$\mathcal{Y}_C Z_L R^2 = -\omega^2\mu\epsilon\frac{h_L}{h_C}R^2\,. \tag{21}$$

Thus, in Eq. (12) and all other equations that follow from this one, h is replaced by h_C, and Eq. (21) has to be inserted in the denominator. Hereby Eqs. (15), (16) and (17) become:

$$E_r(\omega,\phi',\theta',\phi,\theta) = \frac{MZ_L}{4\pi h_C^2}\sum_{n=0}^{\infty}\frac{2n+1}{n(n+1)-\omega^2\mu\epsilon\frac{h_L}{h_C}R^2}P_n(\cos\gamma)\,, \tag{22}$$

$$B_\phi(\omega,\phi',\theta',\phi,\theta) = \frac{\mu M}{4\pi R h_C}\frac{\partial\gamma}{\partial\theta}\sum_{n=0}^{\infty}\frac{2n+1}{n(n+1)-\omega^2\mu\epsilon\frac{h_L}{h_C}R^2}P_n^1(\cos\gamma)\,, \tag{23}$$

$$B_\theta(\omega,\phi',\theta',\phi,\theta) = -\frac{\mu M}{4\pi R h_C\sin\theta}\frac{\partial\gamma}{\partial\phi}\sum_{n=0}^{\infty}\frac{2n+1}{n(n+1)-\omega^2\mu\epsilon\frac{h_L}{h_C}R^2}P_n^1(\cos\gamma)\,. \tag{24}$$

For the uniform calculations we use the complex, frequency dependent heights from Mushtak and Williams (2002) (Fig.3) which is often refereed as a two-height two-scale-height description of ELF wave propagation.

For the evaluation of the (associated) Legendre polynomials in practical applications (Eqs. 22, 23 and 24), it is convenient to use the following recursive formula:

$$(n+1-m)P_{n+1}^m(x) = (2n+1)xP_n^m - (n+m)P_{n-1}^m(x)\,, \tag{25}$$

where $x = \cos\theta$, and $P_n^0 \equiv P_n$. Using this relation, we only need the first few Legendre polynomials, namely $P_0^0 = 1$, $P_1^0 = x$, $P_1^1 = -(1-x^2)^{1/2}$, and $P_2^1 = -3x(1-x^2)^{1/2}$.

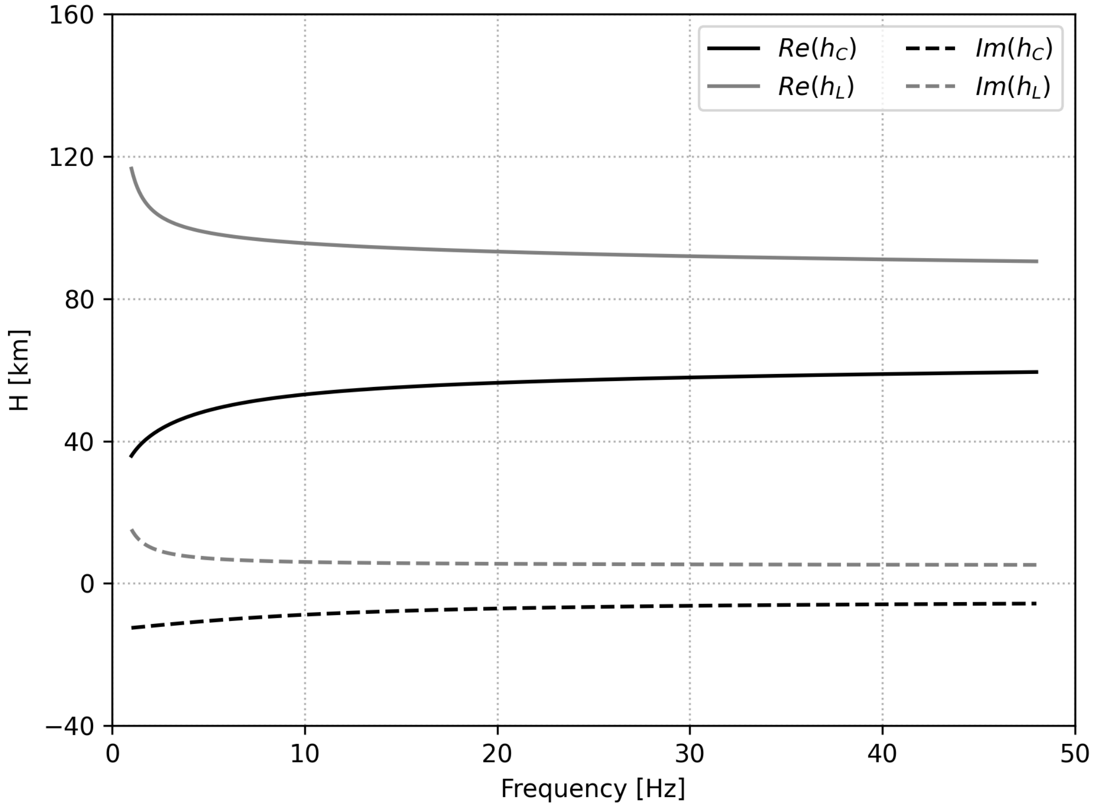

Figure 3: The complex, frequency dependent heights from Mushtak and Williams (2002).

In case the source is at the $\theta' = 0$ position this solution is equivalent to the widely used solutions given in Mushtak and Williams (2002). To prove this statement, first we introduce the complex, frequency dependent propagation parameter of the spherical cavity ν which can be obtained based on the following relation:

$$\nu(\nu+1) = k^2 R^2 \frac{h_L}{h_C} \,, \tag{26}$$

where k denotes the free space wave number (Mushtak and Williams, 2002). From Eq. (21) it follows that:

$$\mathcal{Y}_C Z_L R^2 = -\omega^2 \mu\epsilon \frac{h_L}{h_C} R^2 = -(kR)^2 \frac{h_L}{h_C} = -\nu(\nu+1) \,. \tag{27}$$

This means that Eqs. (22), (23) and (24) can be written as:

$$E_r(\omega,\theta) = -\frac{jM}{4\epsilon\omega R^2 h_C} \frac{\nu(\nu+1)}{\pi} \sum_{n=0}^{\infty} \frac{2n+1}{n(n+1)-\nu(\nu+1)} P_n(\cos\theta) \,, \tag{28}$$

$$B_\phi(\omega,\theta) = \frac{\mu M}{4\pi R h_C} \sum_{n=0}^{\infty} \frac{2n+1}{n(n+1)-\nu(\nu+1)} P_n^1(\cos\theta) \,, \tag{29}$$

$$B_\theta = 0 \,, \tag{30}$$

where we applied Eqs. (18) and (27). As the P_ν Legendre function of complex order ν can be calculated as:

$$\frac{P_\nu(-x)}{\sin(\nu\pi)} = -\frac{1}{\pi}\sum_{n=0}^{\infty}\frac{2n+1}{n(n+1)-\nu(\nu+1)}P_n(x) \; , \tag{31}$$

Eq. (28) can be written in the following form:

$$E_r(\omega,\theta) = \frac{jM}{4\epsilon\omega R^2}\frac{\nu(\nu+1)}{h_C}\frac{P_\nu(-\cos\theta)}{\sin(\nu\pi)} \; , \tag{32}$$

a formula used for example by Galejs (1972); Mushtak and Williams (2002); Wait (1996). Similarly, by applying the

$$\frac{P^1_\nu(-x)}{\sin(\nu\pi)} = \frac{1}{\pi}\sum_{n=0}^{\infty}\frac{2n+1}{n(n+1)-\nu(\nu+1)}P^1_n(x) \; , \tag{33}$$

relation in Eq. (29) we get:

$$B_\phi(\omega,\theta) = \frac{\mu M}{4Rh_C}\frac{P^1_\nu(-\cos\theta)}{\sin(\nu\pi)} = \frac{\mu M}{4R}\left(\frac{c}{R\omega}\right)^2\frac{\nu(\nu+1)}{h_L}\frac{P^1_\nu(-\cos\theta)}{\sin(\nu\pi)} \; , \tag{34}$$

in accordance with the solution presented by Mushtak and Williams (2002). With the complex propagation parameter ν, the voltage can be calculated as:

$$V(\omega,\theta) = \frac{jM\nu(\nu+1)}{4\epsilon\omega R^2}\frac{P_\nu(-\cos\theta)}{\sin(\nu\pi)} \; . \tag{35}$$

There are multiple methods to calculate the complex P_ν and P^1_ν functions. They can be obtained as a series of real Legendre polynomials (Wait, 1996) (see Eqs. 31 and 33). The advantage of this approach is its simple programmability. However, its convergence is rather slow. Therefore, the speeding up technique of Nickolaenko and Rabinowicz (1974) is recommended for the calculation of this series. Another method to calculate P_ν arises from its original definition with the hypergeometric function (see e.g., Erdelyi, 1953):

$$P_\nu(-x) = F\left(-\nu,\nu+1,1,\frac{1+x}{2}\right) \; . \tag{36}$$

The third calculation method we present is based on the addition formula for Legendre functions (Erdelyi, 1953):

$$\begin{aligned} P_\nu(-\cos\gamma) = P_\nu\left(-\cos\theta\cos\theta' - \sin\theta\sin\theta'\cos\Psi\right) = \\ P_\nu(-\cos\theta)P_\nu(\cos\theta') + 2\sum_{m=1}^{\infty}(-1)^m \\ \times\frac{\Gamma(\nu-m+1)}{\Gamma(\nu+m+1)}P^m_\nu(-\cos\theta)P^m_\nu(\cos\theta')\cos(m\Psi) \; , \end{aligned} \tag{37}$$

where $\Psi = \phi - \phi'$, while Γ and P^m_ν denote the Gamma function and the associated Legendre function of order m, respectively. The application of Eq. (37) in the case of the uniform Earth-ionosphere waveguide is not effective considering its computation time. We still present it since it shows the connection between the description of the uniform and the non-uniform cases. Later we will show that Eq. (35) with Eq. (37) represents a special case of the general formula describing the resonance field in the non-uniform Earth-ionosphere cavity.

2.1.4 Analytical Solution for the Non-uniform Cavity

Kirilov et al. (1997) published an analytical method to calculate the distribution of V in the non-uniform case where the day-night asymmetry of the Earth-ionosphere waveguide is taken into consideration. As a first step towards inferring the non-uniform solution we return to the uniform case with arbitrary source location where V has both θ and ϕ dependence (Fig. 4a). In this case, an equivalent form of Eq. (7), with the dimensionless complex propagation parameter ν, reads as:

$$\frac{\partial}{\partial x}\left((1-x^2)\frac{\partial}{\partial x}V\right)+\nu(\nu+1)V=\nu(\nu+1)\frac{j\mathcal{I}_{\mathcal{S}}h_C}{\epsilon\omega R^2}\delta(\theta')\,, \tag{38}$$

where $x=\cos\theta$.

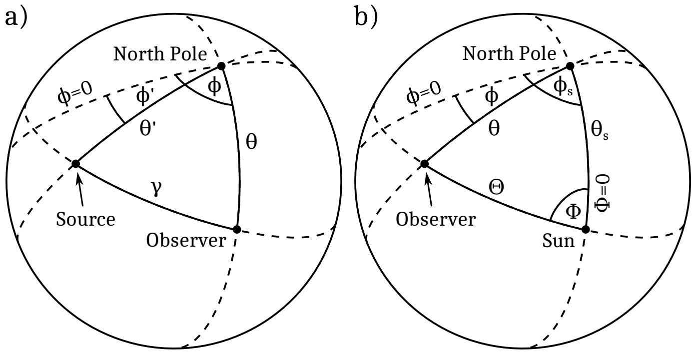

Figure 4: **Left**: Polar coordinates of the source (ϕ',θ') and the observer (ϕ,θ). γ denotes the angle between the source and the observer. **Right**: Polar coordinates of the observer (Φ,Θ) in the Sun-directed (transformed) coordinate system. The polar coordinates of the source (Φ',Θ') in the Sun-directed (transformed) coordinate system can be acquired in the same way.

The solution of this equation can be derived via the separation of variables. We look for a particular solution of Eq. (38) in the following separated form:

$$V(\phi,\theta)=V_p(\phi)V_t(\theta)\,. \tag{39}$$

The equation governing $V_t(\theta)$ then becomes:

$$\begin{aligned}\frac{\partial}{\partial x}\left((1-x^2)\frac{\partial}{\partial x}V_t\right)+V_t\left(\nu(\nu+1)-\frac{m^2}{1-x^2}\right)\\=\nu(\nu+1)\frac{j\mathcal{I}_{\mathcal{S}}h_C}{\omega\epsilon R^2}\delta(\theta')\,,\end{aligned} \tag{40}$$

while for $V_p(\phi)$ it is:

$$\frac{\partial^2}{\partial\phi^2}V_p=-m^2V_p\,, \tag{41}$$

where m is the separation variable. The solutions for Eq. (40) are the associated Legendre functions $P_\nu^m(\cos\theta)$ and $P_\nu^m(-\cos\theta)$ while the solutions for Eq. (41) are $\cos(m\psi)$ and $\sin(m\psi)$. However, the latter solution cannot fulfill the singularity property of the voltage V at the source location. Therefore, the general solution reads as:

$$V = c\sum_{m=0}^{\infty}\left[c_{1,m}P_\nu^m(\cos\theta) + c_{2,m}P_\nu^m(-\cos\theta)\right]\cos(m\psi)\,. \tag{42}$$

In the case of the uniform waveguide the coefficients c, $c_{1,m}$ and $c_{2,m}$ must satisfy only one condition, namely that V should have a singularity only at the source location, where finite power must flow into the waveguide from a point source, which requires an infinite field strength locally. The coefficient c is determined by the singularity property of the Legendre function and the source strength. Note, that $P_\nu^m(-\cos\theta)$ and $P_\nu^m(\cos\theta)$ in Eq. (42) have singularities at $\theta = 0$ and $\theta = \pi$, respectively. We can also obtain a formula of type (42) for V from Eqs. (35) and (37). The latter equation determines the coefficients $c_{1,m}$ and $c_{2,m}$.

Including the day-night asymmetry with this analytical model relies on the assumption that the surface of the Earth can be divided into two regions (dayside and nightside) and the waveguide is uniform within each region. Conveniently, one can perform a coordinate transformation to a system where the z-axis points towards the Sun and the day-night terminator is represented by a constant coordinate. In this new coordinate system, where the boundary conditions take a convenient form, we denote the coordinates of the Sun, the terminator, the source and the observer by Θ_s $(= 0°)$, Θ_t $(\approx 90°)$, (Φ',Θ') and (Φ,Θ), respectively (see Fig. 4b). The two hemispheres can be described as:

$$\nu = \begin{cases} \nu_d \text{ if } \Theta < \Theta_t\,, \\ \nu_n \text{ if } \Theta \geq \Theta_t\,, \end{cases} \tag{43}$$

hence, in the non-uniform case Eq. (42) is valid in the dayside and in the nightside domain but with different ν indices of Legendre functions (ν_d or ν_n). For our non-uniform calculations we use the complex ionospheric heights $h_C^{(d)}$, $h_L^{(d)}$ and $h_C^{(n)}$, $h_L^{(n)}$ from Kulak and Mlynarczyk (2013), which correspond to the dayside and nightside domains, respectively, from where ν_d and ν_n can be obtained based on Eq. (26). The coefficient c is the same as in the uniform case (see Eq. 35):

$$c = \frac{jM\nu_s(\nu_s+1)}{4\epsilon\omega R^2\sin(\nu_s\pi)}\,, \tag{44}$$

where $s = \{d,n\}$ depend on the location of the source. The $c_{1,m}$ and $c_{2,m}$ coefficients can be calculated from the boundary conditions that V and $\partial V/\partial\Theta$ must be continuous at the day-night terminator. Furthermore, V should have singularity only at the position of the source.

Now let us suppose that the source is on the dayside ($\Theta' < \Theta_t$). To calculate $c_{1,m}$ and $c_{2,m}$ coefficients, we first introduce the following quantities:

$$b_{1,m} = \epsilon_m (-1)^m \frac{\Gamma(\nu_d - m + 1)}{\Gamma(\nu_d + m + 1)} P_{\nu_d}^m(-\cos\Theta')\,, \tag{45}$$

$$b_{2,m} = \epsilon_m (-1)^m \frac{\Gamma(\nu_d - m + 1)}{\Gamma(\nu_d + m + 1)} P_{\nu_d}^m(\cos\Theta')\,, \tag{46}$$

$$\begin{aligned} R_m = -b_{2,m} \Bigg[& P_{\nu_d}^m(-\cos\Theta_t) \frac{\partial}{\partial x} P_{\nu_n}^m(-\cos\Theta_t) \\ & - \frac{h_L^{(n)}}{h_L^{(d)}} P_{\nu_n}^m(-\cos\Theta_t) \frac{\partial}{\partial x} P_{\nu_d}^m(-\cos\Theta_t) \Bigg] \\ & \times \Bigg[P_{\nu_d}^m(\cos\Theta_t) \frac{\partial}{\partial x} P_{\nu_n}^m(-\cos\Theta_t) \\ & + \frac{h_L^{(n)}}{h_L^{(d)}} P_{\nu_n}^m(-\cos\Theta_t) \frac{\partial}{\partial x} P_{\nu_d}^m(\cos\Theta_t) \Bigg]^{-1}\,, \end{aligned} \tag{47}$$

$$d_m = \frac{b_{2,m} P_{\nu_d}^m(-\cos\Theta_t) + R_m P_{\nu_d}^m(\cos\Theta_t)}{P_{\nu_n}^m(-\cos\Theta_t)}\,, \tag{48}$$

where R_m is the reflection coefficient, d_m is the propagation coefficient and

$$\begin{cases} \epsilon_m = 1 & \text{if} \quad m = 0\,, \\ \epsilon_m = 2 & \text{if} \quad m > 0\,. \end{cases} \tag{49}$$

Next, we need to distinguish between two cases in respect to the relative position of the source (Θ') and the observer (Θ). If $\Theta < \Theta'$, i.e. the observer is closer to the Sun than the source, the coefficients are:

$$c_{1,m} = b_{1,m} + R_m\,, \tag{50}$$

$$c_{2,m} = 0\,, \tag{51}$$

while in the case when $\Theta' \leq \Theta$:

$$c_{1,m} = R_m\,, \tag{52}$$

$$c_{2,m} = b_{2,m}\,. \tag{53}$$

If $\Theta > \Theta_t$, which means that the observer is on the nightside, the coefficients take the following form:

$$c_{1,m} = 0\,, \tag{54}$$

$$c_{2,m} = d_m\,. \tag{55}$$

These equations require the accurate calculation of the Gamma function with a complex argument. In our code the numerical calculation of the complex Gamma function was performed based on the method of Lanczos (1964). In the uniform case (where $h_L^{(n)} = h_L^{(d)}$) $R_m = 0$, $d_m = b_{2,m}$ and we obtain a version of Eq. (35), where the Legendre function is calculated with the addition formula (Eq. 37). Similar formulas exist for the case when the source is on the nightside.

To transform the original coordinate system (ϕ,θ) to the Sun-centered spherical coordinates (Φ,Θ) the cosine and sine theorems for spherical triangles should be applied. Choosing the $\Phi = 0$ meridian of the Sun-centered coordinate system to cross the North Pole of the original coordinate system (see Fig. 4b) the spherical triangle theorems can be applied:

$$\begin{aligned} \cos\Theta &= \cos\theta_s \cos\theta + \sin\theta_s \sin\theta \cos(\phi_s - \phi)\,, && (56)\\ \sin\Phi &= \sin(\phi_s - \phi)\frac{\sin\theta}{\sin\Theta}\,. && (57) \end{aligned}$$

The same equations apply for the primed coordinates as well.

To obtain the magnetic components in the transformed coordinate system Eq. (14) should be applied. Since we need to take the partial derivatives with respect to the original coordinates the chain rule of derivation has to be used:

$$\frac{\partial V}{\partial \theta} = \frac{\partial V}{\partial \Theta}\frac{\partial \Theta}{\partial \theta} + \frac{\partial V}{\partial \Phi}\frac{\partial \Phi}{\partial \theta}\,, \tag{58}$$

$$\frac{\partial V}{\partial \phi} = \frac{\partial V}{\partial \Theta}\frac{\partial \Theta}{\partial \phi} + \frac{\partial V}{\partial \Phi}\frac{\partial \Phi}{\partial \phi}\,. \tag{59}$$

The partial derivatives of Θ and Φ against θ and ϕ can be obtained from Eqs. (56) and (57).

2.1.5 Numerical Solution for the Non-uniform Cavity

Our numerical solution of Eq. (5) was first introduced in Pracser et al. (2021) and can be regarded as a modified version of the solution given by Galuk et al. (2018). Instead of discretizing the original form of Eq. (5) we first integrated it in order to obtain linear connections in V between neighbouring nodal points. We expected an increase in numerical accuracy owing to this step. The discretization requires a grid (θ_i, ϕ_j, $i = 1...N$, $j = 1...M$) on the Earth's surface which is illustrated in Fig. 5.

An equivalent form of Eq. (5) reads as:

$$\operatorname{div}\frac{1}{L}\operatorname{grad} V + \omega^2 \mathcal{C}(V + V_s) = 0\,, \tag{60}$$

which follows from Eq. (20) and the $V_S = \mathcal{I}_S/\mathcal{Y}_\mathcal{C}$ relation. By integrating this equation over the domain A and applying Gauss theorem we arrive at the following form:

$$\int\limits_{dA} \frac{1}{L}\mathbf{n}\operatorname{grad} V \mathrm{d}l + \iint\limits_{A} \omega^2 \mathcal{C} V \mathrm{d}s = -\iint\limits_{A} \omega^2 \mathcal{C} V_s \mathrm{d}s\,, \tag{61}$$

where dA is the boundary of A and $\mathbf{n}$ is the normal vector perpendicular to dA. This equation contains only the first derivatives of the voltage which can be replaced

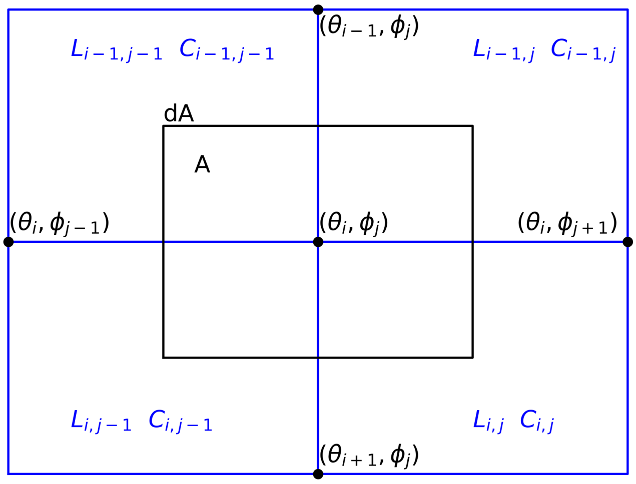

Figure 5: Discretization of the Earth's surface.

by ratios of finite differences. Let us denote the voltage at the node (i,j) by $V_{i,j}$. This way the first term on the left side of Eq. (61) can be approximated by:

$$\begin{aligned}&\left(\frac{1}{L_{i-1,j-1}}+\frac{1}{L_{i-1,j}}\right)\frac{V_{i,j}-V_{i-1,j}}{\Delta\theta}\sin\left(\theta_{i-1}+\frac{1}{2}\Delta\theta\right)\frac{\Delta\phi}{2}\\&+\left(\frac{1}{L_{i,j-1}}+\frac{1}{L_{i,j}}\right)\frac{V_{i+1,j}-V_{i,j}}{\Delta\theta}\sin\left(\theta_{i}+\frac{1}{2}\Delta\theta\right)\frac{\Delta\phi}{2}\\&+\left(\frac{1}{L_{i,j-1}}+\frac{1}{L_{i+1,j-1}}\right)\frac{V_{i,j}-V_{i,j-1}}{\sin\theta_i\ \Delta\phi}\frac{\Delta\theta}{2}\\&+\left(\frac{1}{L_{i,j}}+\frac{1}{L_{i+1,j}}\right)\frac{V_{i,j+1}-V_{i,j}}{\sin\theta_i\ \Delta\phi}\frac{\Delta\theta}{2}\ ,\end{aligned}\tag{62}$$

while the second term on the left-hand side becomes:

$$\begin{aligned}&\omega^2 V_{i,j}R^2\frac{\Delta\theta\Delta\phi}{4}[\sin\left(\theta_{i-1}+\frac{1}{2}\Delta\theta\right)(\mathcal{C}_{i-1,j-1}+\mathcal{C}_{i-1,j})\\&+\sin\left(\theta_{i}+\frac{1}{2}\Delta\theta\right)(\mathcal{C}_{i,j-1}+\mathcal{C}_{i,j})]\ .\end{aligned}\tag{63}$$

The right-hand side of Eq. (61) is 0 except at the node occupied by the source. This way the $V_{i,j}$ voltage values are determined by a system of linear equations. In our numerical algorithm $\Delta\theta=\Delta\phi=1°$, i.e. the number of grid points is $179\times 360+2$.

In our code the source must be assigned to a specific node but the observer can be at any location as we can interpolate between the nodes. Let us suppose that for the θ and ϕ coordinates

$$\theta_i\le\theta<\theta_{i+1}\ ,\quad \phi_j\le\phi<\phi_{j+1}\ ,\tag{64}$$

where θ_i and ϕ_i are grid point coordinates. In this case we expect for $V(\phi,\theta)$ the following form:

$$V(\phi,\theta)=\sum_{k=0}^{3}\sum_{l=0}^{3}c_{k,l}P_k(\cos\theta)\cos(l\phi)\ .\tag{65}$$

The coefficients $c_{k,l}$ can be calculated from the nearby values of the voltage in the nodes ($V_{m,n}$, $m = i - 1,...,i + 2, n = j - 1,...,j + 2$). This calculation is a problem of fitting that leads to a system of linear equations, the solution of which gives the coefficients $c_{k,l}$. The partial derivatives required for the magnetic field components (Eq. 14) are calculated by differentiating Eq. (65) with respect to θ and ϕ.

It is to be emphasized, that this numerical solution is applicable for any distribution of the propagation parameter ν and not only for the special case of cavity non-uniformity described in Section 2.1.4.

2.1.6 Modeling Multiple Sources

As it has been discussed in the Introduction it is not possible to distinguish single lightning strokes in the “background” SR measurements. Therefore, the Earth’s surface has to be divided into elementary source zones characterized by average $M(\omega) = Ids(\omega)$ current moment values. Superimposed lightning strokes are incoherent in nature, therefore to obtain the effect of multiple sources their power spectral density (PSD) values must be added (Nickolaenko et al., 1996; Shvets et al., 2009). The PSD of the current moment yields the following unit:

$$[PSD(Ids)] = \frac{A^2m^2}{Hz} = \frac{C^2/s^2\ m^2}{Hz} = \frac{C^2m^2}{s} \, . \tag{66}$$

This quantity represents the measure of lightning activity in ”background” SR research (Dyrda et al., 2014; Shvets et al., 2009) and can be interpreted in the following way. The radiated field from a lightning flash is proportional to the total charge transferred times the vertical distance that charge is moved, i.e. the charge moment change (CMC) (Qds) of the source (Heckman et al., 1998). As the radiated field is proportional to the CMC, the energy is proportional to the square of the CMC. We can get a quantity that is proportional to the energy radiated by lightning sources within a time unit (one second) by multiplying the radiated energy with the average stroke rate (λ, $[\lambda] = 1/s$). This quantity has the unit of:

$$[CMC^2] * [\lambda] = \frac{C^2m^2}{s} \, , \tag{67}$$

that is exactly the source term we apply. It follows that one needs to calculate the PSD of the measured field component to be in accordance with this description. As the channel length of lightning strokes is in the order of km, it is more common to use the unit of $\mathrm{C}^2\,\mathrm{km}^2/\mathrm{s}$ for the source term.

From Eqs. (22), (23) and (24) it is clear that each field component can be described in the following compact form:

$$E_r(\omega,\phi',\theta',\phi,\theta) = M(\omega) * G_E(\omega,\phi',\theta',\phi,\theta) \, , \tag{68}$$

$$B_\phi(\omega,\phi',\theta',\phi,\theta) = M(\omega) * G_{B,\phi}(\omega,\phi',\theta',\phi,\theta) \, , \tag{69}$$

$$B_\theta(\omega,\phi',\theta',\phi,\theta) = M(\omega) * G_{B,\theta}(\omega,\phi',\theta',\phi,\theta)\,, \tag{70}$$

where G_E, $G_{B,\phi}$ and $G_{B,\theta}$ are the frequency responses of the cavity for the electric and magnetic field components, respectively. It follows that, for example, the magnetic field at different observation places can be described by the following matrix equation, where we assume m different elementary source zones and n different observation places:

$$\begin{bmatrix} |G_{B,1,1}|^2 & |G_{B,1,2}|^2 & \cdots & |G_{B,1,m}|^2 \\ |G_{B,2,1}|^2 & |G_{B,2,2}|^2 & \cdots & |G_{B,2,m}|^2 \\ \vdots & \vdots & \ddots & \vdots \\ |G_{B,n,1}|^2 & |G_{B,n,2}|^2 & \cdots & |G_{B,n,m}|^2 \end{bmatrix} \begin{bmatrix} |S_1|^2 \\ |S_2|^2 \\ \vdots \\ |S_m|^2 \end{bmatrix} = \begin{bmatrix} |B_1|^2 \\ |B_2|^2 \\ \vdots \\ |B_n|^2 \end{bmatrix}\,, \tag{71}$$

where $G_{B,j,k}$ denotes the frequency response of the Earth-ionosphere cavity to a source of unit strength within the k^{th} source zone measured at the j^{th} observation site, $S_k^2 = |Ids(\omega)|_k^2$ and B_j^2 is the PSD of the measured magnetic field. For the sake of simplicity, the matrix equation is written for only one frequency and for one magnetic field component. However, this can be generalized for multiple frequencies and for the two magnetic and one electric field components. In general the magnetic induction vector on the right side of Eq. (71) should be replaced by $F_{c,j,l}$, where the first index (c) represents the electromagnetic field component (E_r, B_ϕ or B_θ), the second one (j) the observation site and the third one (l) the frequency. In that case $G_{B,j,k}$ in Eq. (71) has to be replaced by $G_{c,j,l,k}$. As the current moment spectrum of a typical lightning stroke is assumed to be flat in the ELF range, S_k^2 values do not depend on the frequency. The short form of the generalized description reads as follows:

$$\overline{\overline{\mathbf{G}}}\,\overline{\mathbf{s}} = \overline{\mathbf{f}}\,, \tag{72}$$

where vector $\mathbf{s}$ and $\mathbf{f}$ contains the S_k^2 and $F_{c,j,l}^2$ values, respectively.

2.2 The Open Source Python Package *schupy*

In Bozoki et al. (2019) the open-source python package `schupy` and its very-first function `forward_tdte` had been introduced which enables the simulation of SRs generated by an arbitrary distribution of lightning sources specified by the user and returns the theoretical electric and magnetic fields at the user-specified location. The `forward_tdte` function applies the analytical solution corresponding to the lossy, uniform cavity described in Section 2.1.3, and can simulate point sources as well as extended ones. It is possible to specify the size of the extended source, which the code will represent as randomly distributed point sources (100 points as a set-in value) within the given radius from the center of the source, which has a total intensity specified by the user. The code calculates the squared absolute value of the investigated electromagnetic field components corresponding to the power spectral density (PSD) of the recorded electromagnetic fields in real SR measurements (see Section 2.1.6). The method of the complex ionospheric height calculation can be set either to "mushtak" corresponding to the height calculation proposed by Mushtak and Williams (2002) or to "kulak" corresponding to the height calculation proposed by Kulak and Mlynarczyk (2013). Geographic locations of the sources and of the observing station can be visualized by `schupy`, making use of the `cartopy` package for visualization of the Earth[1]. The `schupy` package is available via the `pip` package manager system (`https://pypi.org/project/schupy/`) and the project's Github page: `https://github.com/dalyagergely/schupy`, where a more detailed technical description is presented as well.

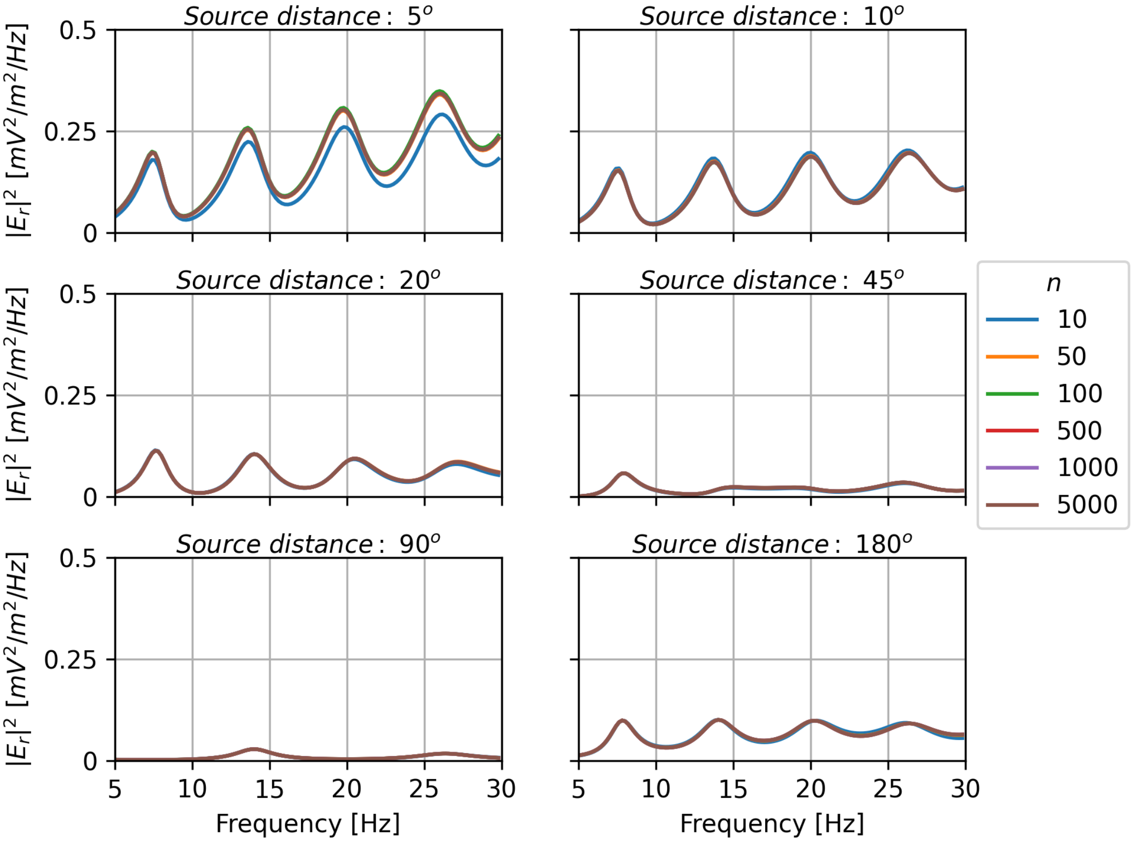

Figure 6: Convergence of the theoretical spectra of the $|E_r|^2$ component for different source-observer distances. n denotes the maximal order of Legendre polynomials to sum.

Following Bozoki et al. (2019) we present three tests based on the `schupy.forward_tdte` function. First, the convergence of theoretical spectra is tested, then the spectra generated by two antipodal sources is compared and finally the difference between the spectra of point and extended sources is investigated. These tests demonstrate the usefulness of `schupy` in investigating SR-related

---

[1] `https://scitools.org.uk/cartopy/docs/latest/`

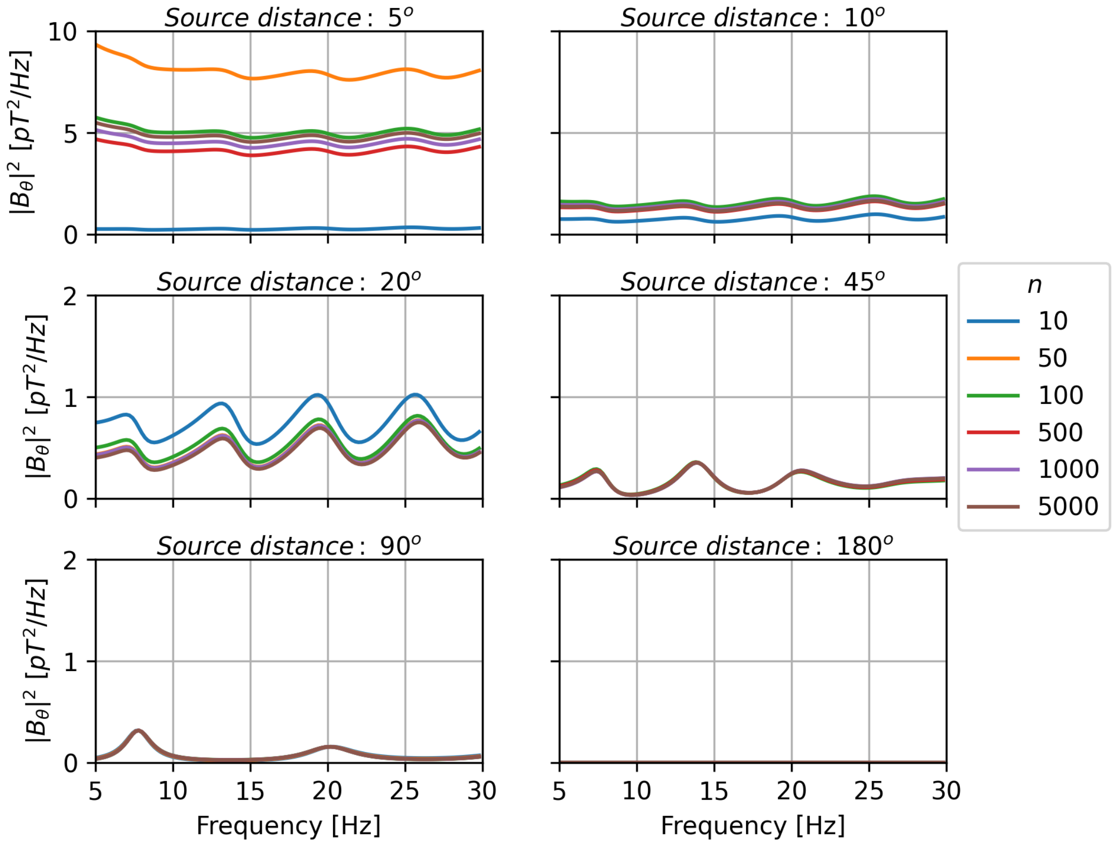

Figure 7: The same as Fig. 6 but for the $|B_\theta|^2$ component. Note, that the upper limit of the y axis is different for the two shortest source-observer distances than for the other cases.

scientific questions.

2.2.1 Convergence of Theoretical Spectra

As it can be seen in Eqs. (22), (23) and (24) the electromagnetic field components of SRs can be calculated as an infinite summation of (associated) Legendre polynomials. Practically, only a finite number of summation can be done (up to n), thus the question arises: at what n can we accept the result? It is to be noted, that the answer depends on the source-observer distance.

In order to investigate this problem we carry out a test where the positions of a point-like lightning source with 10^5 $\mathrm{C}^2\,\mathrm{km}^2/\mathrm{s}$ source intensity are: (0°, 5° E), (0°, 10° E), (0°, 20° E), (0°, 40° E), (0°, 90° E) and (0°, 180° E), respectively and the theoretical spectra are determined for the (0°, 0°) location in each case. The theoretical spectra are calculated for the following values of n: [10, 50, 100, 500, 1000, 5000]. All the positions are on the Equator, therefore the $|B_\phi|^2$ component is always zero. The results are shown in Fig. 6 and Fig. 7.

It can be noted that the electric component converges faster than the magnetic. Our conclusion is that in most cases $n = 500$ should be enough except for B_θ when the observer is close to the source ($\leq 5°$). In Figs. 6 and 7 it can be seen that the resonance peaks are not always symmetric. This is especially the case closer to the source. This property of the resonance curves can be attributed to the presence of traveling waves which transmit energy from source to the resonator (Kulak et al., 2006).

2.2.2 Theoretical Spectra of Antipodal Sources

This test is devoted to comparing theoretical spectra of antipodal sources. Here, our motivation is to gain more insight about non-uniqueness, which manifests as parallel equivalent solutions for the SR inversion task (see e.g., Prácser et al., 2019). In a lossless cavity antipodal sources would produce exactly the same spectra at arbitrary location on Earth. However, the Earth-ionosphere cavity is lossy, which is taken into account by introducing h_L and h_c complex equivalents of the altitudes. The question is, in what extent does the theoretical spectra differ in this formalism.

We place two sources with same intensities of 10^5 $\mathrm{C}^2\,\mathrm{km}^2/\mathrm{s}$ at antipodal positions (0°, 90° W) and (0°, 90° E) and determine the theoretical spectra for the following locations: (0°, 0°), (0°, 15° E), (0°, 30° E), (0°, 45° E), (0°, 60° E) and (0°, 75° E). As in the previous test, all the positions are on the Equator, therefore the $|B_\phi|^2$ component is always zero.

It can be seen that in the midpoint (0°, 0°) theoretical spectra are exactly the same (Figs. 8 and 9). However, apart from this specific point the two spectra are noticeably different. We note that the resonance frequencies corresponding to the antipodal sources are usually different as well.

2.2.3 Point Versus Extended Source

In this test we compare the theoretical spectra of a point source with those of a distributed source (with a radius of 1 Mm). Both the centroid position of the extended source and the location of the point source are (0°, 0°) and we determine the theoretical spectra for the equatorial distances of 20°, 30°, 60°, 90°, 120° and 150°. The extended source consists of 100 randomly distributed sources within the given radius with a total intensity of 10^5 $\mathrm{C}^2\,\mathrm{km}^2/\mathrm{s}$, the same value as set for the point source. Figures 10 and 11 shows the results for the $|E_r|^2$ and $|B_\theta|^2$ component, respectively. As in the previous two studies $|B_\phi|^2$ is always zero. The absolute difference between the theoretical spectra generated by the two kinds of sources is quite small. We note that 90° is a nodal distance for the first and third mode of the electric component and for the second and fourth mode of the magnetic component. At this distance the spectral intensities are nearly 0.

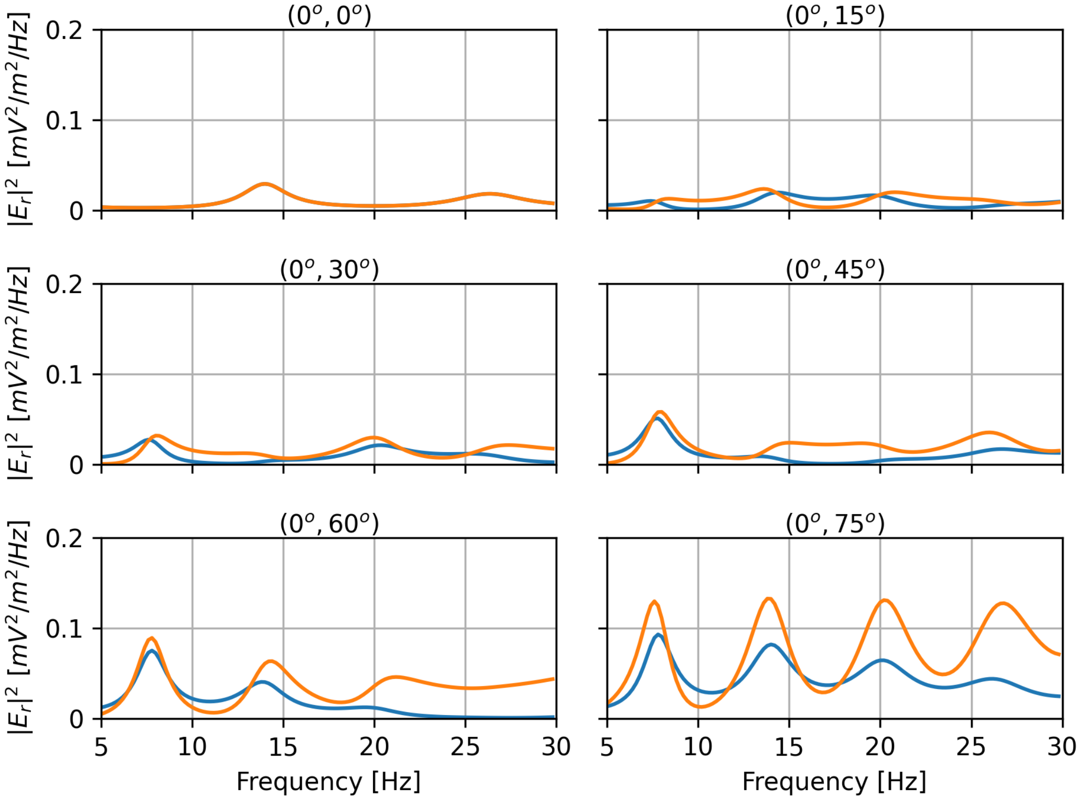

Figure 8: Theoretical spectra of the $|E_r|^2$ component at different observer positions for the two antipodal sources. The orange and blue lines mark the theoretical spectra of the sources at the (0°, 90° E) and (0°, 90° W) locations, respectively.

2.3 Numerical Validation Tests

As it has been described in Sections 2.1.4 and 2.1.5 the TDTE (Eq. 5) can be solved either analytically or numerically. In both approaches some inaccuracy of the algorithms can be expected and this is particularly true for the non-uniform case where the day-night asymmetry of the Earth-ionosphere cavity is taken into consideration. An analytical solution requires the summing of nested infinite series that often converge very slowly (Nickolaenko and Rabinowicz, 1974). In the numerical solution the unknown continuous function is estimated only at certain discrete points and this worsens the accuracy of the calculation. Therefore, we consider it an important task to implement both methods and compare their output by means of numerical tests (Pracser et al., 2021).

We carry out three different numerical tests to compare the output of our two independent models. In each test we calculate the squared absolute value of the investigated electromagnetic field components corresponding to the power spectral density (PSD) of the recorded electromagnetic fields in real SR measurements (see Section 2.1.6). This is the quantity commonly extracted from SR measurements.

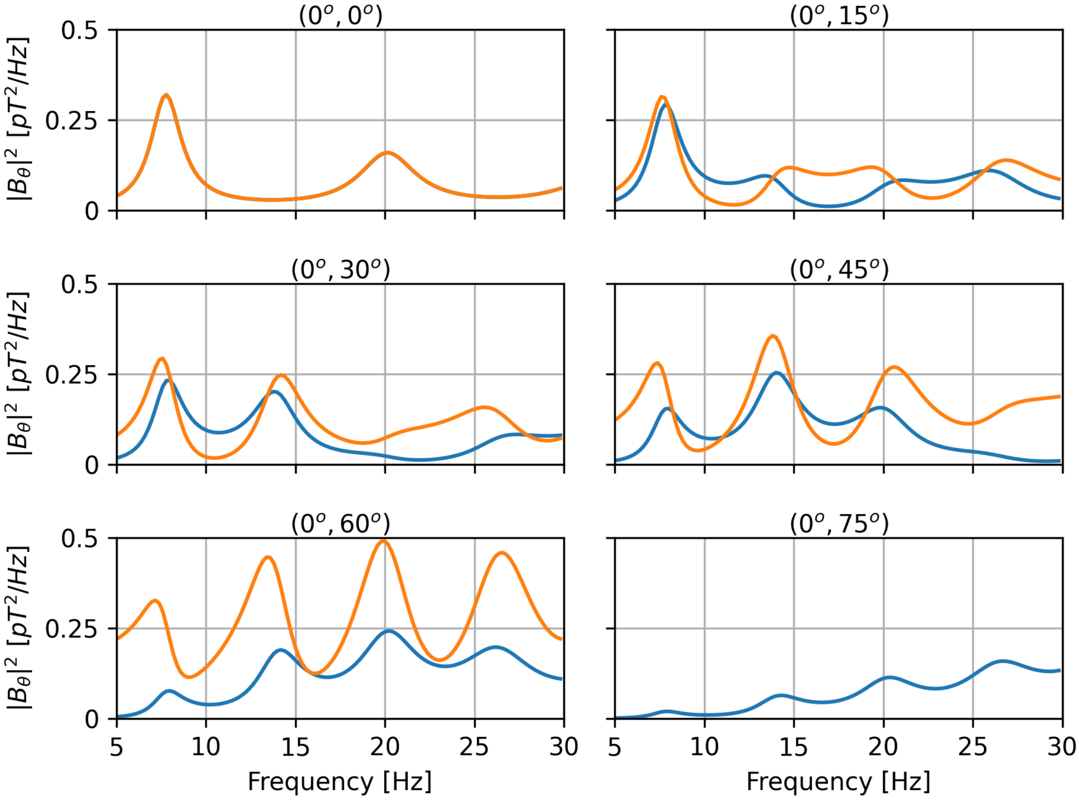

Figure 9: The same as Fig. 8 but for the $|B_\theta|^2$ component.

For the calculations we use the complex ionospheric heights proposed by Kulak and Mlynarczyk (2013).

2.3.1 7.9 Hz in the Uniform Cavity

Our first test is performed for the uniform case. We compare the $|E_r|^2$ values of the analytical and the numerical calculations for $f = \omega/2\pi = 7.9$ Hz (the approximate value of the first Schumann resonance mode) as a function of the angular distance between the source (with an assumed source strength of 6×10^4 $\mathrm{C^2\,km^2/s}$) and the observer. As it can be seen in Fig. 12 both models produce practically the same output (the two results agree within 0.2% over nearly the entire domain), only a slight difference can be observed near the source, where the solutions become singular. Fig. 12 reflects the basic spatial structure of the first SR mode, namely that the electric field has a minimum near 90° and a secondary maximum at the antipode, i.e. at the angular distance of 180° from the source.

2.3.2 7.9 Hz in the Non-Uniform Cavity

In our second test we compare the analytical and numerical calculations for 7.9 Hz for the non-uniform Earth-ionosphere cavity including day-night asymmetry (Fig. 13 and Fig. 14). In order to do so we fix the position of the source and the observer

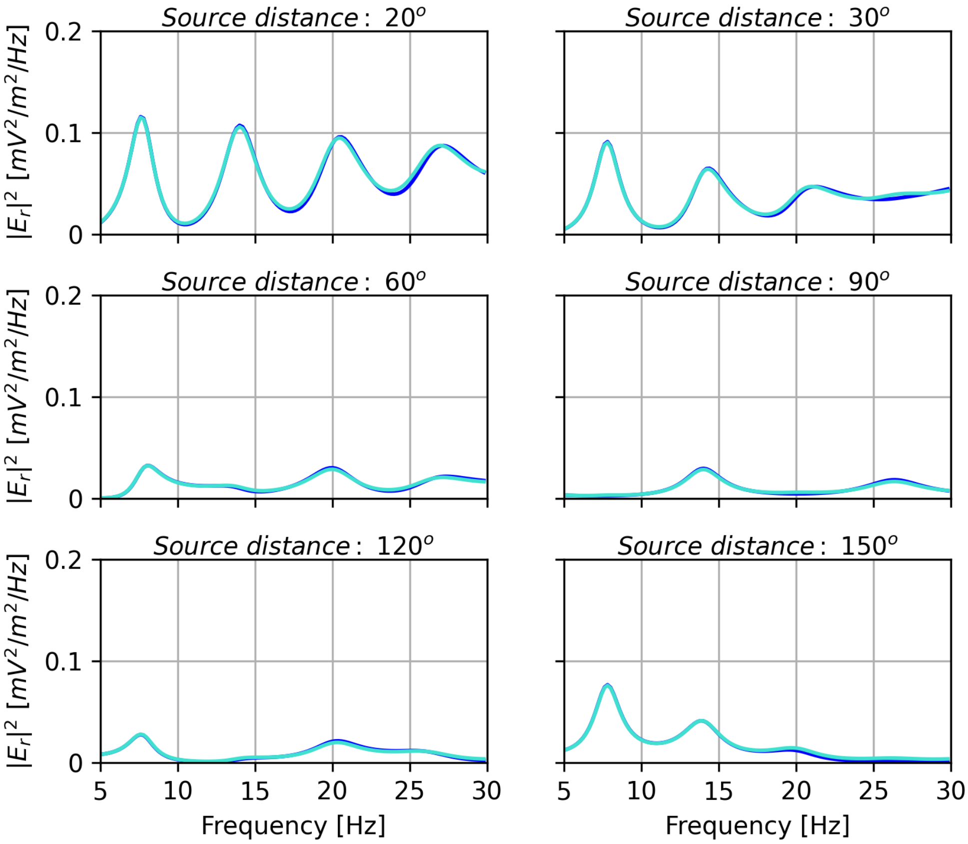

Figure 10: Theoretical spectra of the $|E_r|^2$ component for different source-observer distances corresponding to a point (blue) and an extended (light blue) (radius = 1 Mm) source.

and vary the position of the Sun. In the test shown in Fig. 13 (for the electric component) and Fig. 14 (for the magnetic component) the Sun is located at the Equator and both the source (10° N, 0° E, 6×10^4 $\mathrm{C}^2\,\mathrm{km}^2/\mathrm{s}$) and the observer (70° N, 60° E) are in the Northern Hemisphere. It follows that the day-night boundary has north-south direction. As a reference we have determined the $|E_r|^2$ and $|B_\theta|^2$ values for the uniform cavity with dayside and nightside propagation parameters, respectively. At 7.9 Hz the real parts of the complex ionospheric heights take the following value: $h_c^{(d)} = 53.1$ km, $h_l^{(d)} = 101.4$ km, $h_c^{(n)} = 62.5$ km, $h_l^{(n)} = 114.5$ km (Kulak and Mlynarczyk, 2013). In accordance with our expectation the intensity for the non-uniform model lies between the nightside-only and dayside-only models. We can conclude, that the agreement between the two model outputs is excellent (the relative difference is less than 0.05% and 0.08% for the electric and magnetic components, respectively). When interpreting the figures it is important to take into consideration that the day-night terminator is 90° (in longitude) from the position of the Sun. There are four discontinuities in the electric field component (Fig. 13) corresponding to the cases when the day-to-night transition (dawn) meets the source (Sun position: 90°) and the observer (Sun position: 150°) as well as when the night-to-day transition (dusk) does the same (Sun positions: −90° and −30°). The

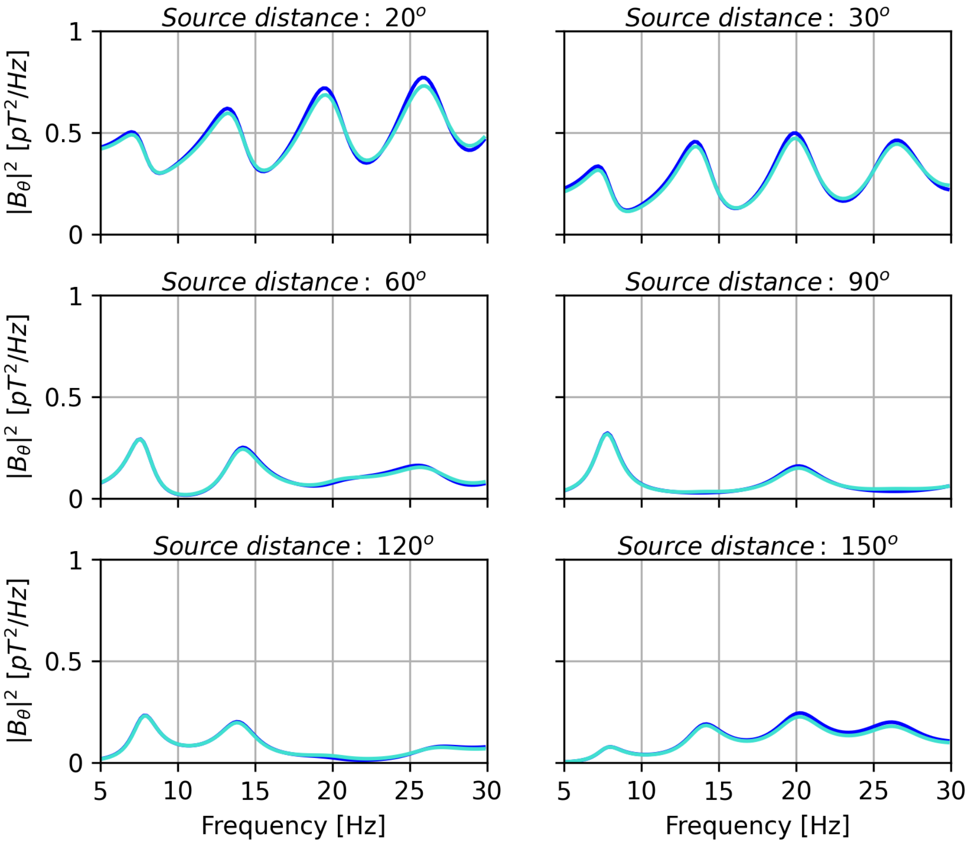

Figure 11: The same as Fig. 10 but for the $|B_\theta|^2$ component.

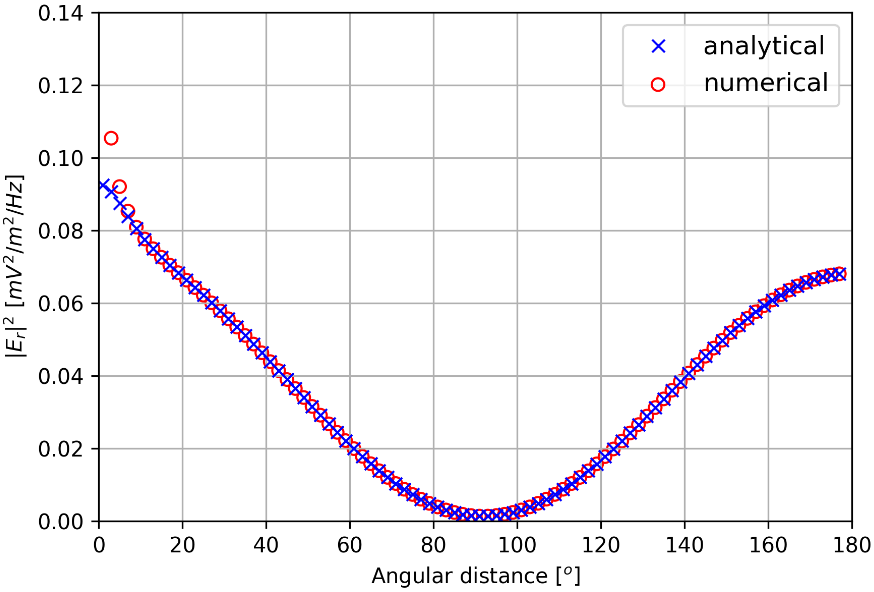

Figure 12: The electric field intensity at 7.9 Hz for the uniform Earth-ionosphere cavity as a function of the distance from the source at 0° determined by our analytical and numerical models. The two results agree within 0.2% at angular distances larger than 15°.

magnetic field component (Fig. 14) is continuous when the day-night terminator crosses the observer location, which follows from the continuity of the current density components perpendicular to this boundary.

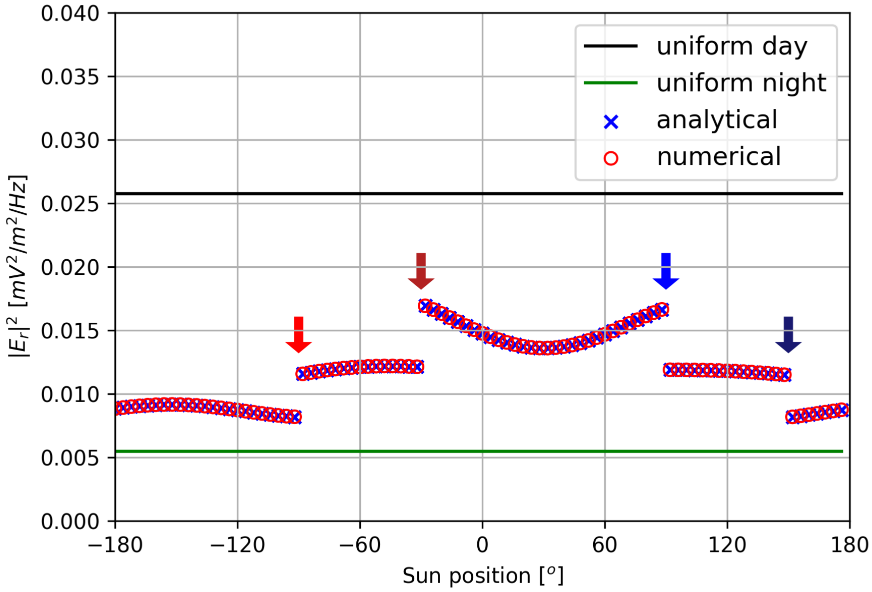

Figure 13: The electric field intensity at 7.9 Hz for the uniform and non-uniform Earth-ionosphere cavity as a function of the Sun's position determined by our analytical and numerical models. The two results agree within 0.05%. Red and blue arrows mark the Sun positions corresponding to the night-to-day (dawn) and day-to-night (dusk) transitions at the source (light colors) and the observer (dark colors).

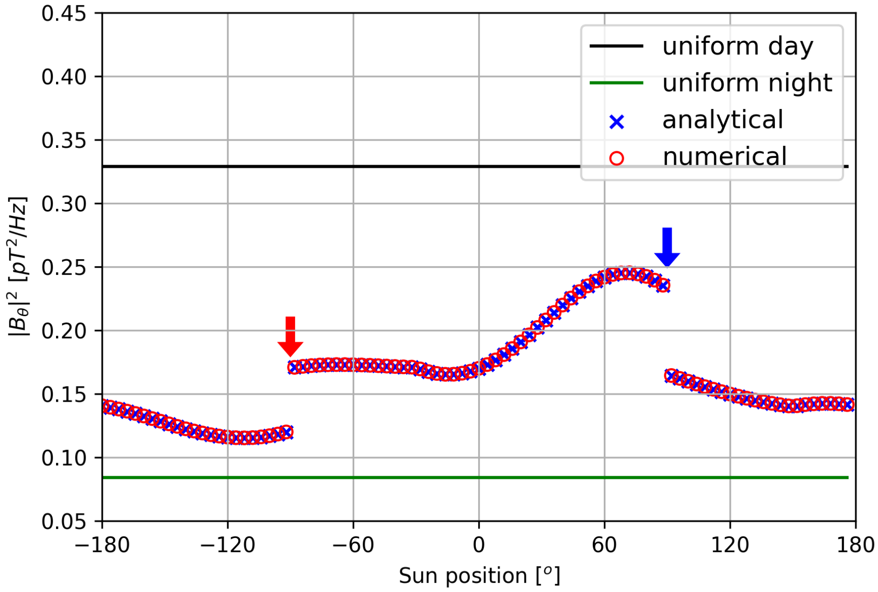

Figure 14: The same as Fig. 13. but for the θ component of the magnetic field intensity. Here the results of the two non-uniform models agree within 0.08%.

2.3.3 Full Spectra in the Non-Uniform Cavity

Finally, we test our calculations on full spectra similar to what we obtain in practice from SR measurements. For this test we use three sources to represent the prominent continental "chimneys" with geographical coordinates (0° N, 80° W), (7° S, 20° E) and (0° N, 110° E), and with source strengths of 6×10^4 C^2 km^2/s, 9×10^4 C^2 km^2/s and 6×10^4 $C^2\,km^2/s$, respectively. We calculate the spectra for two observation sites, one at (77° N, 15° E) (representing the Hornsund ELF station of the Polish Academy of Sciences in Svalbard) and the other at (44.3° N, 142.2° E) (representing the Moshiri ELF station in Japan). Fig. 15 shows the spectra obtained with our analytical and numerical models for the $|E_r|^2$ and $|B_\theta|^2$ field components at these locations with the expected resonance peaks at ∼8 Hz, ∼14 Hz and ∼20 Hz. Once again excellent agreement is noted between the results produced by the two approaches which agree within 0.4% over nearly the entire domain.

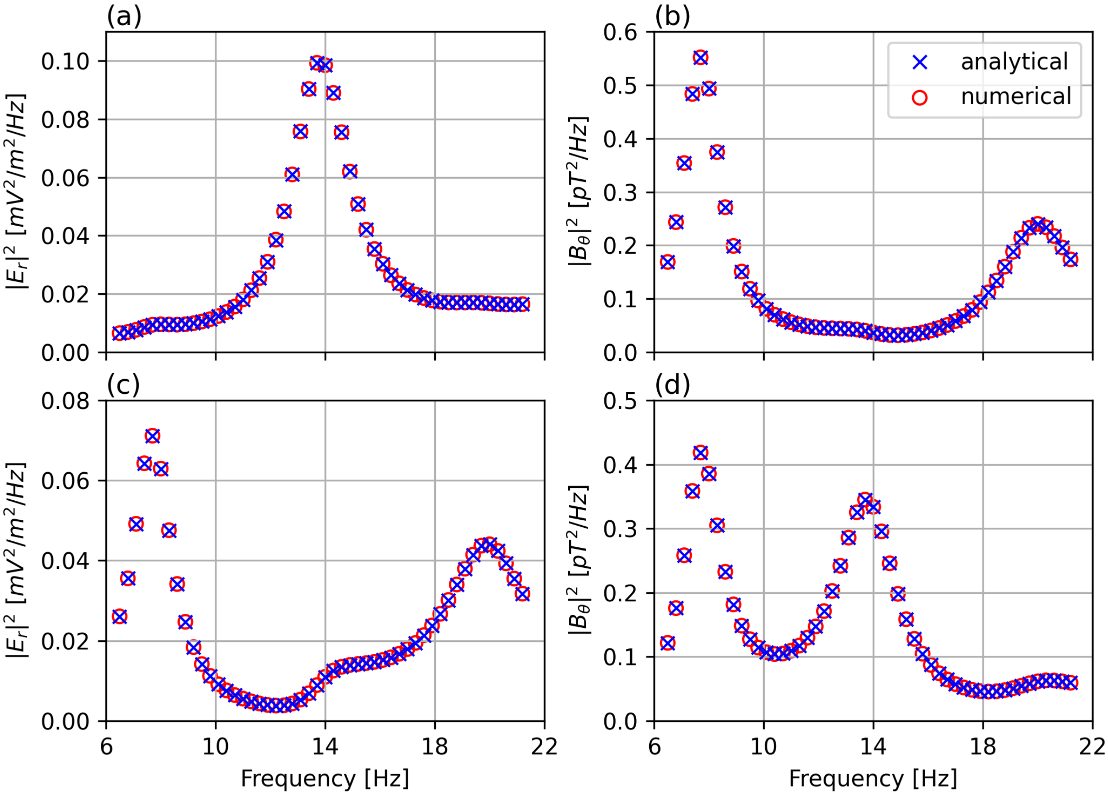

Figure 15: Modelled spectra for the $|E_r|^2$ (a,c) and $|B_\theta|^2$ (b,d) field components. Subplots (a) and (b) correspond to the observation site at (77.0° N, 15° E) while subplots (c) and (d) correspond to the observation site at (44.3° N, 142.2° E). The results agree within 0.4% over nearly the entire domain.

2.3.4 Conclusions of the Validation Tests

The three tests show a conspicuous conformity between the output of the analytical and numerical models, which can be regarded as the validation of the two methods. As the two solutions are based on completely independent mathematical formalisms the conspicuous conformity between the outputs establishes not only the correctness of the formalisms but the correctness of the implementations (the coding) as well. To the best of our knowledge Pracser et al. (2021) was the first paper to verify this conformity between the two solutions.

3 Inversion of Schumann Resonance Measurements

This chapter describes our inversion algorithm (Prácser et al., 2019) aimed to determine the intensity and distribution of global lightning activity based on SR measurements.

3.1 Introduction

Lightning activity is getting increasing attention in the research community as it is recognized now as an essential climate variable by the Word Meteorological Organization (WMO) indicating the changing climate of the Earth. The underlying reason for that is the nonlinear relation between the lightning activity and surface temperature (Williams, 1992). Efforts are now underway to monitor its long-term characteristics on local, regional, and global scales, including the stroke occurrence rate, the average charge transfer, and the distribution of thunderstorm affected areas (e.g., Blakeslee et al., 2014).

Optical detection carried out by satellites provides one possibility to study lightning activity on global scales. Although satellites in Low Earth Orbit are not able to detect lightning strokes shielded by clouds or outside the suborbital swath, statistical studies are an important output of such measurements (e.g., Christian et al., 2003). However, continuous monitoring of a specific thunderstorm area is not possible with this method. A major advance for continuous lightning detection in the American sector came with the Geostationary Lightning Mapper instrument onboard the new generation Geostationary Earth Orbit satellite GOES-R (Goodman et al., 2013) and in the Asian sector with the Lightning Mapping Imager instrument onboard the FengYun-4A satellite (Yang et al., 2017).

On the other hand, ground-based monitoring of global lightning activity with practical independence from the actual cloud thickness and from the time of the day also serves as an important method with much lower foundation requirements for lightning research. Most of the ground-based lightning monitoring techniques are based on the EM signal generated by lightning and propagating within the Earth-ionosphere waveguide for the detection. As lightning radiated power peaks in the VLF frequency range (3–30 kHz; Wait, 1996) one possibility is to monitor global lightning activity with a network of VLF receivers such as the World Wide Lightning Location Network (WWLLN)[2]. Although wave attenuation in the VLF band is relatively small (about 10 dB/Mm; Barr et al., 2000), several hundreds of receiver stations are necessary to achieve global coverage with such a system. At the

---

[2] http://wwlln.net

moment the detection efficiency of the WWLLN lies around a few tens of percent, from which it is only possible to give rough estimations on global lightning activity (Bürgesser, 2017; Hutchins et al., 2012). This available technology prevents the detailed quantitative comparison of lightning activity on continental scales on time scales ranging from the diurnal to the interannual.

Wave attenuation in the lowest part of the ELF frequency range (<100 Hz) is much smaller (about 0.5 dB/Mm; Chapman et al., 1966; Wait, 1996) and enables the investigation of global lightning activity with only a few (1–20) receiver stations. In contrast to VLF methods detection efficiency does not arise as a difficulty in the ELF band because all individual lightning discharges with vertical extent contribute to the SR field. Since the ice-based process of charge separation in thunderstorms is gravity-driven, charge is basically separated vertically in the thundercloud so every lightning flash in the atmosphere (intracloud and cloud-to-ground alike) is expected to contribute to the SR intensity. An average charge moment change can be derived from SR measurements in absolute units of $\mathrm{C}^2\,\mathrm{km}^2/\mathrm{s}$ (see Section 2.1.6), a quantity not biased by chosen event selection criteria as in case of statistics based on the number density of strokes or flashes provided by other methods.

Previously several attempts were made to determine the global lightning distribution based on SR records. Heckman et al. (1998) presented 10 days of inverse calculations using three component ($\mathrm{H_{NS}}$, $\mathrm{H_{EW}}$, $\mathrm{E_Z}$) field measurements at the Rhode Island station. Their approach assumed three thunderstorm regions at fixed locations, computed their contribution to the measured fields, and tried to find the best linear combination of source intensities to reproduce the measured spectrum. Shvets (2001) proposed an inversion technique based on the linear and nonlinear combination of the electric and magnetic field power spectra in order to infer worldwide lightning activity without any preliminary supposition about its spatial structure. While Shvets (2001) worked with the solution of the 2D telegraph equation, later Ando and Hayakawa (2007); Ando et al. (2005) and Yang et al. (2009) used 3D finite difference equations for the SR modeling. These methods enabled the determination of the 1D distribution of lightning intensity relative to one observation point. Later, Shvets and his co-authors (Shvets and Hayakawa, 2011; Shvets et al., 2009, 2010) implemented a two-stage inversion process called “ELF tomography.” After determining the 1D lightning distribution from a few observation sites their model combined the results into 2D maps of worldwide lightning activity with a second inversion step. Dyrda et al. (2014) characterized the lightning activity of the African thunderstorm center based on a single ELF station in Poland, Hylaty. After applying spectral decomposition to the SR data (proposed by Kulak et al., 2006) the activity and the distance of the most powerful African thunderstorm center has been derived with 1° spatial and 10-min time resolution. The authors demonstrated that the inferred 1D lightning activity maps are in good agreement with satellite measurements. It is to be mentioned that this was the first work using two-scale-height ionospheric characterization for the SR inversion task but only for the simplified 1D case. For more details about the motivation and history of SR inversions we recommend the work of Nickolaenko and Hayakawa (2014), where the authors devote an entire chapter to this thriving topic (Inverse problem of SR). We would like to highlight one further work on SR inversion, namely, the PhD thesis of P. H. Nelson (Nelson, 1967), which serves as the basis for our technique and has been further improved during our work.

3.2 Description of the Inversion Algorithm

Geophysical inversions in the case of electromagnetic methods are usually based on the knowledge of the source of electromagnetic field and the goal is to determine the electrical properties of the medium. However, in the inversion of SR measurements the situation is just the reverse. The medium where the wave propagation takes place (the Earth-ionosphere waveguide) is assumed and the goal is to determine the locations and strengths of the sources.

Here we mention two different approaches for this procedure. One option is to assume a limited number of sources and then determine both their location and intensity (Williams and Mareev, 2014; Williams et al., 2014b). However, in this case the unknown parameters of the inversion are physically different, i.e. source coordinates and intensities. In general, this can be less favorable for the stability of the inversion. Another possibility is to assume a relatively large number of sources (in order of 10–100) on a given grid with fixed locations and the inversion algorithm estimates only the intensities of the grid points. All the grid points are accounted for in the inversion, and for locations without source activity the inversion algorithm assigns a negligible amount of intensity. In our algorithm this second approach has been implemented and hereafter, the given grid is called the inversion grid.

The inversion task means the solution of Eq. (72) for the unknown $|S_k|^2$ values characterizing lightning activity within the k^{th} elementary source zone. Because of the use of squared values the forward calculation is linear; theoretically, a simple minimization could be used in the least squares sense

$$||\overline{\overline{\mathbf{G}}}\overline{\mathbf{s}} - \overline{\mathbf{f}}||^2 = min. \tag{73}$$

However, this would not be appropriate as the measured data contain noise and the applied Earth-ionosphere model is just an approximation to the real one. Therefore, negative values for source strength could be obtained as well. In Shvets et al. (2009) this problem is solved by means of the nonnegative least squares algorithm. To avoid negative source strengths our inversion algorithm uses the logarithms of the source intensities, i.e. $|S_k|^2 = e^{|L_k|}$ substitution. As a result, the forward modeling is no longer linear and an iterative linearized inversion technique has to be used starting from initially assumed model parameters.

The applied linearized inversion is based on the singular value decomposition (SVD) of the Jacobian (Jackson, 1972; Lanczos, 1960)

$$\mathbf{J} = \mathbf{U}\Lambda\mathbf{V}^T \, , \tag{74}$$

where the columns of $\mathbf{U}$ and $\mathbf{V}$ matrices are the eigenvectors $\mathbf{u}_k$ and $\mathbf{v}_k$ in the data and parameter spaces, respectively, and superscript T denotes transposition. The diagonal matrix Λ contains the λ_k eigenvalues in descending order. Eigenvectors with 0 eigenvalues are omitted from the matrices $\mathbf{U}$ and $\mathbf{V}$. The $\mathbf{u}_k$ and $\mathbf{v}_k$ eigenvectors and λ_k eigenvalues fulfill the following relations:

$$\mathbf{J}\mathbf{v}_k = \lambda_k \mathbf{u}_k \, , \;\; \mathbf{J}^T\mathbf{u}_k = \lambda_k \mathbf{v}_k \, , \;\; \mathbf{J}^T\mathbf{J}\mathbf{v}_k = \lambda^2 \mathbf{v}_k \, , \;\; k = 1...m \, . \tag{75}$$

Here we assumed that $m < n$; that is, the problem is mathematically overdetermined (in general, min(m,n) determines the number of eigenvalues to be used). In our case the elements of the Jacobian are

$$J_{c,j,l,k} = |G_{c,j,l,k}|^2 L_k \, , \quad j = 1...n \, , \quad k = 1...m \, , \tag{76}$$

where the L$_k$ term in the Jacobian is the consequence of the logarithmic equation. Based on the singular value decomposition (Eq. 74), the generalized inverse of the Jacobian can be written as (Lanczos, 1960)

$$\mathbf{J}^{-1} = \mathbf{V}\Lambda^{-1}\mathbf{U}^T \, . \tag{77}$$

The benefit of the SVD method (Eq. 74) is that the reliability of the inverted parameters can be inferred from the distribution of the eigenvalues. In general, the number of the highest eigenvalues indicates the number of reliable model parameters. Based on Eq. (77), the change (Δ) of the model parameters in each iteration step can be calculated as

$$\Delta\mathbf{l} = \mathbf{V}\Lambda^{-1}\mathbf{U}^T\Delta\mathbf{f} \, , \tag{78}$$

where vector $\mathbf{l}$ contains the logarithms of the $|S_k|^2$ values.

However, Eq. (78) is mathematically an ill-posed task (indicated by the very high ratio between the highest and lowest eigenvalue of $\mathbf{G}$). Therefore, its regularized version has to be used (Tikhonov and Arsenin, 1977), where the matrix Λ^{-1} is modified, so that its k^{th} element is

$$\frac{\lambda_k}{\lambda_k^2 + \alpha} \, , \tag{79}$$

where α is the damping factor, which can be determined by specifying a given value for the $||\Delta\mathbf{l}||$ parameter change. This modified SVD means the minimization of

$||\overline{\overline{\mathbf{G}}}\bar{\mathbf{s}} - \bar{\mathbf{f}}||^2$ so that $||\Delta \mathbf{l}||^2 \leq \beta$. A large damping factor belongs to a small $||\Delta \mathbf{l}||$ and vice versa. The $\mathbf{J}^T \Delta \mathbf{f}$ vector can be expressed by the linear combination of the $\mathbf{v}_k$ eigenvectors of the SVD via

$$\mathbf{J}^T \Delta \mathbf{f} = \sum_{k=1}^{m} c_k \mathbf{v}_k \, . \tag{80}$$

The same is true for $||\Delta \mathbf{l}||$,

$$\Delta \mathbf{l} = \sum_{k=1}^{m} l_k \mathbf{v}_k \, , \tag{81}$$

where the l_k coefficients are

$$l_k = \frac{c_k}{\lambda_k^2 + \alpha} \, . \tag{82}$$

It follows that α is the solution of the equation

$$\beta = \sum_{k=1}^{m} \left(\frac{c_k}{\lambda_k^2 + \alpha} \right)^2 \, , \tag{83}$$

where β is equal to the $||\Delta \mathbf{l}||$ parameter change. If

$$\sum_{k=1}^{m} \left(\frac{c_k}{\lambda_k^2} \right)^2 \leq \beta \, , \tag{84}$$

then α is equal to 0. In our inversion algorithm β is relatively small (α large); that is, during an iteration step, only a small change of parameter is allowed. This restriction increases the number of iterations, but due to rather fast SR modeling (in case of the uniform model), the calculation is still relatively fast (100 iteration steps require a few seconds). The calculation of α is explained in more detail in Tikhonov and Arsenin (1977).

Our general experience is that the inversion result is practically independent of the selection of β within a reasonable range. By "reasonable range" we mean the avoidance of too high values when the parameters can fluctuate strongly during the iteration and the inversion becomes unstable and also the too small values when the inversion gets very time-consuming. Our experience is that a reasonable range of β is between 1% and 20%.

3.3 Test With Synthetic Data

This section is devoted to describing the most important synthetic tests we have carried out to demonstrate the applicability of our inversion algorithm. In the following five tests we presume three sources within the three major thunderstorm regions on Earth, solve the forward modeling with respect to the observation sites, and invert the source strengths from the generated synthetic data by applying our linearized inversion algorithm. In the first four tests the presumed lightning activity represents the early morning hours in UTC when South-American (SA) activity is in decline, the Maritime Continent (MC) activity is increasing, while Africa (AF) is in a quiet phase (8×10^4 $\mathrm{C}^2\,\mathrm{km}^2/\mathrm{s}$ source intensity in South America, 3×10^4 $\mathrm{C}^2\,\mathrm{km}^2/\mathrm{s}$ in Africa, and 8×10^4 $\mathrm{C}^2\,\mathrm{km}^2/\mathrm{s}$ in the Maritime Continent). In Test 5 the daily average of global lightning activity is represented with African dominance, South America and Maritime Continent in second and third place, respectively (8×10^4 $\mathrm{C}^2\,\mathrm{km}^2/\mathrm{s}$ source intensity in South America, 1×10^5 $\mathrm{C}^2\,\mathrm{km}^2/\mathrm{s}$ in Africa, and 7×10^4 $\mathrm{C}^2\,\mathrm{km}^2/\mathrm{s}$ in the Maritime Continent). The lightning activity maps from the inversion and the inferred integrated lightning activities for the main thunderstorm regions in comparison with the initially assumed source values are presented for all the tests. We also list the ratio of the first and the third eigenvalues of the SVD, indicating the reliability of the three most intense inverted source parameters, and the mean root-mean-square fitting error of the inverted to the synthetic spectra. The inversion is better when these two values are smaller. In our sixth test we draw some conclusions about non-uniqueness, which is the consequence of parallel equivalent solutions for the SR inversion task.

Our tests represent the six-station magnetic field measurements operated by the HeartMath Institute (https://www.heartmath.org/research/global-coherence/; see their position marked with blue rectangles in Fig. 16). While Nelson (1967) and most of the SR-based inverse calculations use only the SR spectral parameters (modal frequency, intensity, and Q factor), we propose to apply the whole obtainable SR frequency range. In that manner the problem is more mathematically constrained. However, the appropriate examination of data quality becomes even more important because the intervening parts of the spectra are more often contaminated by noise than the spectral peaks. Our investigated power spectra consist of 50 equally spaced frequency samples from 6 up to 24 Hz, so the six observation sites contribute altogether $6 \times 2 \times 50 = 600$ data points. The two perpendicular components of the magnetic field (B_{NS} : north-south and B_{EW} : east-west) are usually measured with a pair of induction coils, where the NS coil is oriented along the local geographical meridian (measuring B_ϕ) and the EW coil is perpendicular to it (corresponding to B_θ).

A uniformly spaced inversion grid with 10° × 10° angular resolution has been chosen near the equatorial continental region (from 100° W to 150° E and from 10° S to 20° N) for the tests. This grid is composed of 104 grid points (model parameters) in total. The initial source intensity was 1 $\mathrm{C}^2\,\mathrm{km}^2/\mathrm{s}$ for all the points within the inversion grid, which is entirely negligible compared to the real source activity of the order of 1×10^5 $\mathrm{C}^2\,\mathrm{km}^2/\mathrm{s}$. This means that there is no initial assumption about the lightning distribution.

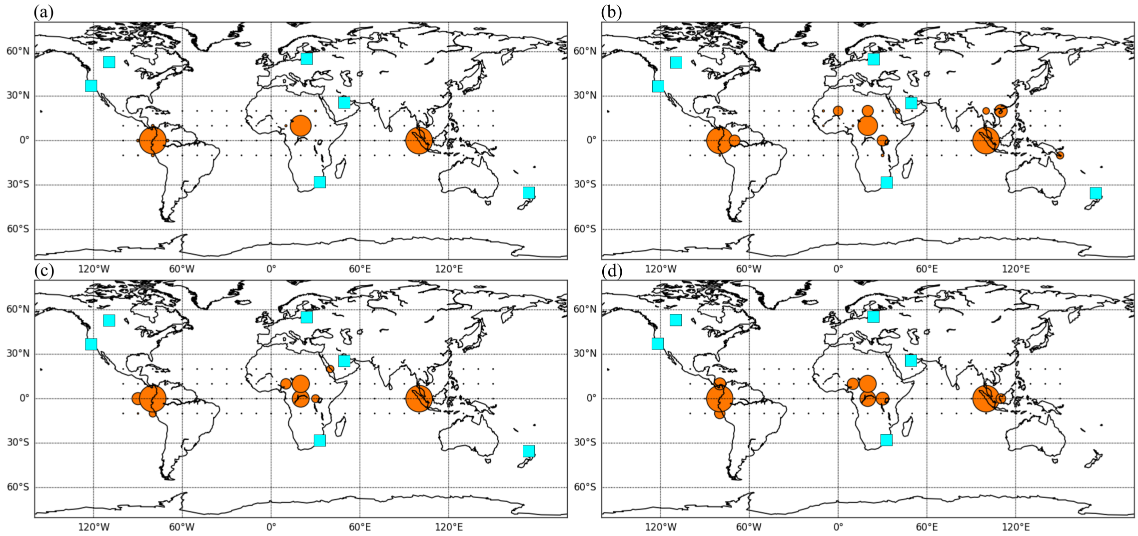

Figure 16: **(a–d)** Result of the Tests 1–4. The sources obtained from the inversion are marked with orange circles with areas proportional to their calculated intensities. Blue squares denote the six HeartMath observation sites.

3.3.1 Test 1 With Noise-Free Data

In the first test the location of each presumed source falls on the inversion grid (South America: 0° N, 80° W; Africa: 10° N, 20° E; Maritime Continent: 0° N, 100° E) and the observed spectra are noise free. The inversion finds the position and the intensity of lightning activity with high accuracy and without any initial information about the sources (Fig. 16a). The assumed and inverted integrated intensities for the major thunderstorm regions are in excellent agreement (Table 1) while the mean root-mean-square (RMS) error is extremely small on the order of 10^{-6} pT^2/Hz (Table 1).

3.3.2 Test 2 With Added Noise

In this test the location of each assumed source falls on the inversion grid (South America: 0° N, 80° W; Africa: 10° N, 20° E; Maritime Continent: 0° N, 100° E) but significant data error with an assumed Gaussian distribution (with 20% relative error) is added to the generated synthetic spectra. Although some false source activity appears in the calculation (Fig. 16b), the inferred total source activity of the main thunderstorm centers are obtained with good accuracy (Table 1). RMS error increased by 4 orders of magnitude compared to Test 1. However, λ_1 to λ_3 ratio shows that the inversion result is still very stable.

3.3.3 Test 3 With a Source Outside the Inversion Grid

It is obvious that positioning the assumed sources exactly on the inversion grid is a very idealistic case. Therefore, in this test the assumed African source does not fall

Source	Assumed Source Intensity	Test 1	Test 2	Test 3
SA	8×10^4	100.0%	91.3%	102.8%
AF	3×10^4	100.0%	104.3%	100.6%
MC	8×10^4	100.0%	105.5%	97.1%
RMS	-	5.02×10^{-6}	2.73×10^{-2}	1.1×10^{-2}
λ_1/λ_3	-	4.437	4.687	4.759

Table 1: Inversion model parameters for the Tests 1–3. The assumed source intensities are given in $\mathrm{C}^2\,\mathrm{km}^2/\mathrm{s}$ while the values obtained from inversion are in relative units compared to the presumed one. Note that while the second column refers to point sources the source intensities from inversion are integrated over the corresponding thunderstorm region. The last two rows contain the RMS fitting error and the ratio of the first and third eigenvalue of the SVD.

onto one of the inversion grid points (South America: 0° N, 80° W; Africa: 5° N, 20° E; Maritime Continent: 0° N, 100° E). Instead, it is placed between the (0° N, 20° E) and (10° N, 20° E) grid points (see Fig. 16c). The synthetic data contain Gaussian noise (with 7% relative error). While the inverted and assumed intensities for the thunderstorm centers are still in reasonable agreement, now the relative ranking of South America and the Maritime Continent has changed compared to Test 2 which can be attributed to non-uniqueness. It seems that the program estimates the intensity of the African source well while it distributes its total source activity between the grid points next to the presumed source center. Therefore, we can conclude that our algorithm handles this situation well. However, based on the ratio of the first and the third eigenvalues the stability of the inversion worsened compared to the previous tests.

3.3.4 Test 4 With One Omitted Observation Site

In our tests each measurement provides 100 data points while the number of inversion model parameters is 104; therefore, the inversion problem is mathematically overdetermined. The possible effect of a data gap at an observation site can be investigated, which still remains an overdetermined problem. Therefore, within this test we omitted the observation sites one by one. The synthetic data contain Gaussian noise (with 7% relative error), and the presumed sources are in the same position as in Tests 1 and 2 (South America: 0° N, 80° W; Africa: 10° N, 20° E; Maritime Continent: 0° N, 100° E). Figure 16d shows the case when observation site 6 has been omitted, and Table 2 summarizes the numerical results of the test. The high λ_1/λ_3 ratio indicates the stability of the result despite the data gaps. Based on the RMS error the inversion is most vulnerable to a data gap at observation site 6 (in New Zealand). We note that observation site 6 is the farthest from every other station and therefore probably provides unique information about the lightning activity.

Source	**Assumed Source Intensity**	**Site 1**	**Site 2**	**Site 3**	**Site 4**	**Site 5**	**Site 6**
SA	8×10^4	101.2%	101.2%	101.9%	100.1%	99.2%	98.8%
AF	3×10^4	98.3%	100.6%	100.3%	99.7%	99.3%	98.6%
MC	8×10^4	99.4%	99.7%	98.0%	100.5%	100.9%	102.6%
RMS	-	$4.4{\times}10^{-3}$	$3.4{\times}10^{-3}$	$3.6{\times}10^{-3}$	$4.1{\times}10^{-3}$	$4.3{\times}10^{-3}$	$5.0{\times}10^{-3}$
λ_1/λ_3	-	4.497	4.274	4.816	4.445	4.286	4.499

Table 2: Inversion model parameters for Test 4 in the same format as in Table 1. The columns with observation site numbers mark the omission of this site in the multistation inversion.

3.3.5 Test 5 With Adding Observation Sites One by One

This test is aimed to investigate the improvement of the results by adding more and more stations to the calculations. The observation sites are added to the calculation one by one in accordance with their numberings. First, we invert the source distribution using only the data from observation site 1, then from the data of observation 1 and 2, etc. Here the presumed source intensities represent the daily average global lightning distribution (8×10^4 $C^2\,km^2/s$ source intensity in South America, 1×10^5 $C^2\,km^2/s$ in Africa, and 7×10^4 $C^2\,km^2/s$ in the Maritime Continent) and they are located on the inversion grid (South America: 0° N, 60° W; Africa: 10° N, 20° E; Maritime Continent: 0° N, 100° E; see Fig. 17). An error is added with Gaussian distribution (with 5% relative error) to the generated synthetic data. It is obvious that the quality of the inversion result increases when adding more and more stations (see λ_1/λ_3 and RMS values in Table 3). Furthermore, it can be concluded that one or two stations are not enough for reconstructing the global lightning activity (see the 26% relative error in the intensity reconstruction of the Maritime Continent), whereas the six-station inversion seems to produce reliable results. As the intensity of the presumed lightning activity differs from the previous tests we can conclude that the model is able to reconstruct lightning activity independently of the presumed distribution and intensity of the sources. However, the mean RMS is smallest for six-station inversion.

It is to be emphasized that here we assume only three dominant lightning sources. If this assumption is not fulfilled in a real situation then probably more observation sites are needed to reconstruct global lightning activity properly.

Source	**Assumed Source Intensity**	**Site 1**	**Site 1-2**	**Site 1-3**	**Site 1-4**	**Site 1-5**	**Site 1-6**
SA	8×10^4	101.6%	102.6%	102.6%	98.2%	99.4%	100.9%
AF	10×10^4	87.0%	100.4%	100.5%	101.7%	98.1%	100.2%
MC	7×10^4	126.4%	96.2%	99.2%	100.6%	102.0%	99.2%
RMS	-	6.0×10^{-3}	4.2×10^{-3}	2.5×10^{-3}	2.3×10^{-3}	1.8×10^{-3}	1.7×10^{-3}
λ_1/λ_3	-	4.389	4.880	4.723	5.044	5.854	5.120

Table 3: Inversion model parameters for Test 5 in the same format as in Table 1. The column header marks the sites used for the actual inversion.

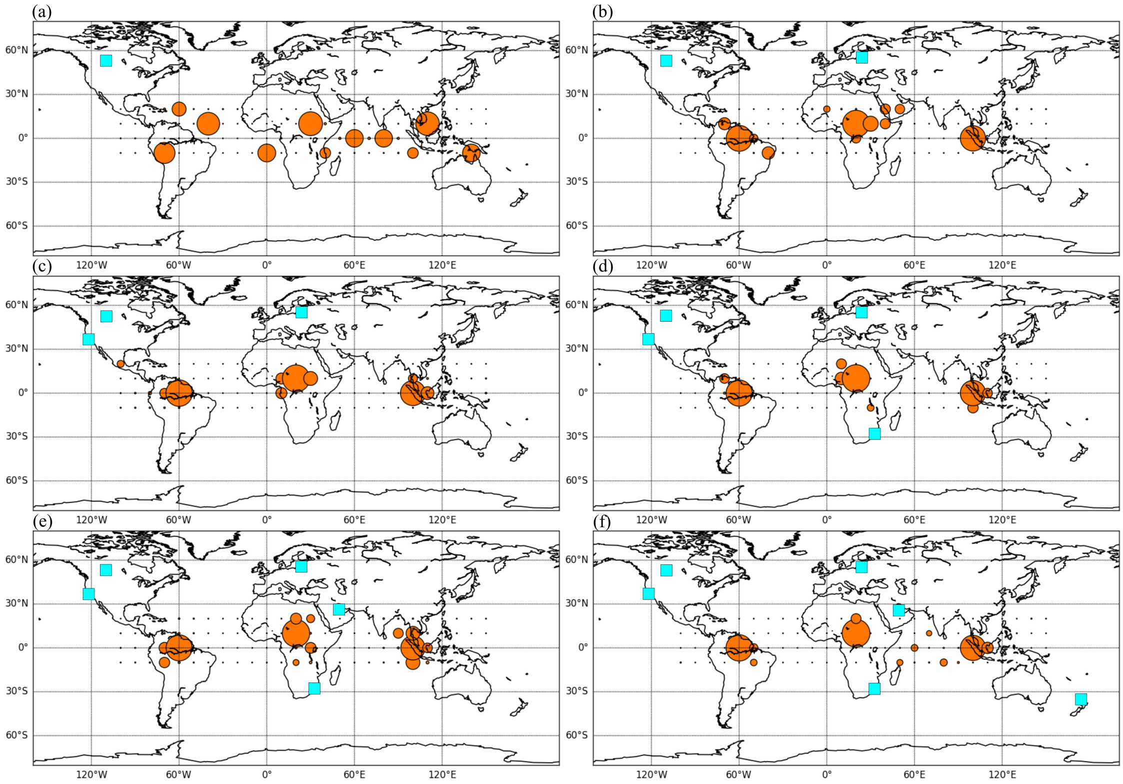

Figure 17: **(a–f)** Result of the Test 5. The notations are the same as in Fig. 16.

3.3.6 Test 6 About Non-uniqueness

At this point it is appropriate to mention a problem connected with SR inversions which was first discussed by Nelson (1967), namely, non-uniqueness, which manifests as parallel equivalent solutions for the SR inversion task. Phase information is lost when the S_k values are squared. As a consequence, propagation direction cannot be assigned to the wave propagation. Therefore, one real source and a "fake" one at the same distance but in the opposite direction from the monitoring station in the case of magnetic measurements yield similar spectra at the station and so they cannot be distinguished. Furthermore, a lossless cavity model would contain two further fake source positions referring to the antipodal pairs of the above two. This problem arises mainly with the nearly diametrically opposite South-American and Maritime Continent thunderstorm centers as it manifests as a high correlation coefficient (0.87) between the eigenvalues corresponding to these two sources in the noise-free test. By adding more stations to the calculation the problem gets more specified which helps to resolve non-uniqueness. This issue has to be investigated in more detail in the future.

In order to get more information about this important issue we have carried out a sixth test with two exactly antipodal sources, one in South America (0° N, 60° W) and one in the Maritime Continent (0° N, 120° E). As our goal is to determine whether the inversion code is able to distinguish between them we assigned different source strengths to them, that is, 1×10^6 $\mathrm{C}^2\,\mathrm{km}^2/\mathrm{s}$ and 5×10^5 $\mathrm{C}^2\,\mathrm{km}^2/\mathrm{s}$ to South America and to Maritime Continent, respectively. Our result is that the program is indeed able to reconstruct the difference between the two lightning zones as we got 101% of the initial source intensity for South America and 98.4% for the Maritime Continent. Our experience is that this result is independent of the initial guess of source distribution. Therefore, we can conclude that non-uniqueness connected with two antipodal sources can be resolved by the losses in the cavity, at least in this simplified situation (only two sources and six observation sites).

3.4 Conclusions

In this chapter we have introduced our SR inversion model based mainly on the PhD thesis of P. H. Nelson (1967). Our aim is to determine the distribution and intensity of the global thunderstorm activity in absolute units ($\mathrm{C}^2\,\mathrm{km}^2/\mathrm{s}$) from a few SR receiving stations which could serve as an important indicator of the Earth's changing climate. The logarithm of the source term has been used in order to avoid negative source intensities. As a consequence the forward modeling is nonlinear, and so we have introduced a linearized inversion algorithm which is based on the singular value decomposition of the Jacobian. In our program a relatively large number of sources with fixed locations are used on a so-called inversion grid and the algorithm estimates the source intensity of each grid point. As not just SR peaks but also the intervening part of the SR spectrum is determined primarily by lightning activity and by wave propagation in the cavity we use the whole obtainable SR frequency range for the inversion in order to make the problem as mathematically constrained as possible. The reliability of our algorithm has been demonstrated via six synthetic tests which represent the six-station magnetic measurements of the HeartMath Institute. In our tests three active source centers were assumed representing the three major thunderstorm regions on Earth. The most important conclusions of these tests are the follows:

- The model is able to reconstruct lightning activity reliably without any preliminary information about the presumed source intensity and distribution.
- Although noise in the data definitely worsens the accuracy of the source location, it barely influences the correctness of the integrated intensity calculated for the main thunderstorm regions.
- The ratio of SVD eigenvalues in the different tests does not fluctuate strongly ($4.274 < \lambda_1/\lambda_3 < 4.816$), which confirms the reliability (stability) of the inferred total intensities.
- The algorithm is capable of handling source activity falling between the inversion grid points, although some false activity might appear as a consequence.
- A data gap at one of the investigated six stations does not influence the results significantly.
- Increasing the number of SR stations does improve the quality of the inversion.
- While data from one or two stations seem not enough to reconstruct the global lightning activity, the six station inversion produce reliable results in case of three dominant lightning chimneys.
- The problem of non-uniqueness manifested as a high correlation coefficient (0.87) between the SVD eigenvalues corresponding to the nearly antipodal South-American and Maritime continent thunder storm centers.
- The algorithm is able to distinguish between two exactly antipodal sources due to the lossiness of the cavity.

We admit that there are countless further possibilities which could supply important information about the model. However, we wanted to restrict ourselves to the most interesting ones. We hope that we could call attention to the importance and usefulness of synthetic tests.

4 Global Lightning Activity on the ENSO timescale

This chapter demonstrates that SRs are a powerful tool to investigate global lightning activity by presenting our results connected to the El Niño–Southern Oscillation (ENSO) phenomenon published in Williams et al. (2021).

4.1 Introduction

The El Niño–Southern Oscillation (ENSO) is an irregularly repeating interannual variation with alternations between a warm (El Niño) and a cold (La Niña) phase, as measured in sea surface temperature. Both ENSO episodes have worldwide influence on the global climate but the warm El Niño period can cause more dramatic changes, manifest in heavy rainfall or severe drought, mainly in the tropical and subtropical regions (Allen et al., 1996). A challenging and up-to-now unresolved issue is the prediction of occurrence and magnitude of El Niño episodes. As with the effects of ENSO, the main global lightning activity worldwide can also be found in the tropics, in three dominant continental regions known as the lightning 'chimneys': the Maritime Continent together with the Indian subcontinent, Africa (including the Congo Basin) and the Americas (including the Amazon Basin of South America). The World Meteorological Organization (WMO) recently declared lightning as one of the essential climate variables (Aich et al., 2018) which underlines the importance of lightning research in studying the impact of ENSO on global climate.

Several studies have looked at the ENSO phenomenon with a focus on its possible effect on lightning activity in selected regions and with emphasis on distinguishing the behavior in the warm phase and the cold phase. For example, the flash rate was higher over the Maritime Continent in the peak warm phase of March 1998 than during the following cold episode in March 1999 of the super El Niño of 1997/98 (Hamid et al., 2001). Comparison of lightning activity in the El Niño (2002) and La Niña years (1998–2001) showed that lightning activity over India increased by nearly 18% in the seasonally-matched warm period (Kandalgaonkar et al., 2003). Evidence for increased lightning activity in the Indian subcontinent and Southeast Asia during the El Niño phase was confirmed by several other works as well (e.g., Ahmad and Ghosh, 2017; Kumar and Kamra, 2012; Tinmaker et al., 2017; Yoshida et al., 2007; Yuan et al., 2016). Analysis of seasonal rainfall and lightning activity showed a strong correlation with ENSO episodes over the central and eastern Mediterranean Sea (Price and Federmesser, 2006). The increased wintertime Southeastern U.S. lightning (thunderstorm) activity during 1997-1998 was attributed to the enhanced synoptic-scale forcing associated with the ENSO (Goodman et al., 2000). Global lightning has also been examined from an ENSO perspective by Chronis et al. (2008) and Satori et al. (2009). Dowdy (2016) has suggested the potential for seasonal forecasting of lightning and thunderstorm activity in various regions throughout the world by studying large-scale modes of atmospheric and oceanic variability. According to his results, ENSO has the strongest relationship with lightning activity during each individual season.

In early ENSO/lightning studies, Williams (1992) found a close correlation between the surface temperature anomaly (Hansen and Lebedeff, 1987) and the horizontal magnetic field component of SRs observed at West Greenwich, Rhode Island in the period 1969–1974, spanning two warm and two cold ENSO episodes. The meridional redistribution of global lightning was deduced from SR frequency variations during the super El Niño event of 1997/98 (Satori and Zieger, 1999). Later, independent evidence for the meridional as well as zonal redistribution of global lightning was given for the super El Niño event of 1997/98 and a moderate El Niño episode in 2002/2003 based on OTD/LIS satellite observations (Satori et al., 2009). It was also shown that the global lightning activity tends to increase worldwide during warm ENSO events over land, especially in the Maritime Continent and India (Satori et al., 2009). Beggan and Musur (2019) studied the possible relationship between SRs and Madden Julian Oscillation (MJO) in 2013-2018. They have found that the periodical variations of SR spectral parameters (intensity, frequency) and MJO are occasionally in phase but exclusively in the years under La Niña condition before and after the super El Niño of 2015/16.

The great majority of studies addressing the ENSO-lightning relationship have dealt with the general behavior of lightning activity during the ENSO warm and cold episodes, respectively. One notable exception is Guha et al. (2017) who studied the warm-to-cold ENSO transition in 2009/2010. Few studies have focused on the temporal evolution of continental-scale lightning activity on the ENSO timescale. The transition period from peak cold phase to peak warm phase represents many months and occasionally more than one year. Here we study global lightning on a monthly basis in the time period of two super El Niño events in 1997/98 and 2015/16 based on SR observations. Although these two extreme climate events were markedly different in some important aspects (Chen et al., 2017), we aim to reveal common signatures in their evolution with attention focused on their effect on continental-scale lightning activity. We shall also be concerned with the precursory signature of ENSO lightning on the global temperature, given earlier evidence that heat is transferred from the ocean to the tropical atmosphere in the warm phase, and subsequently transferred to the global atmosphere (Trenberth et al., 2002). These findings will hopefully contribute to the better understanding and predictability of ENSO in the future.

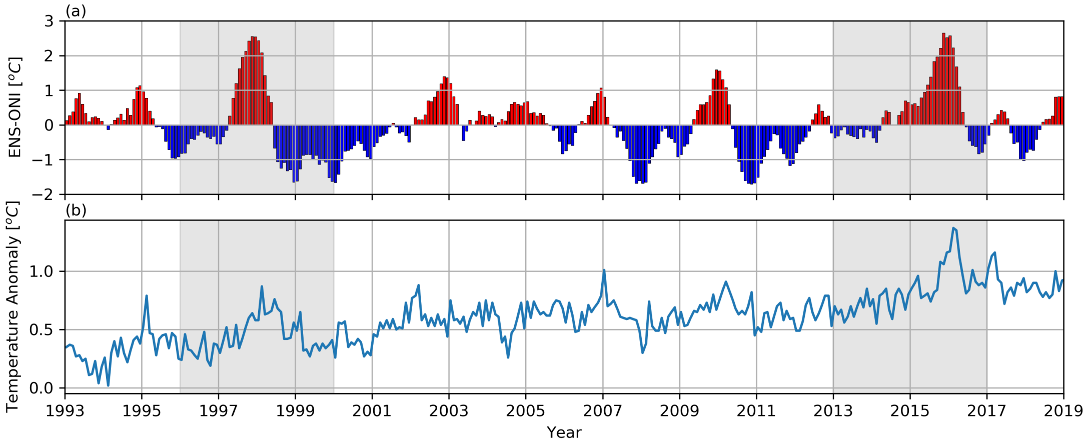

Figure 18: **(a)** The ENS-ONI index and **(b)** the global monthly mean surface temperature change in the time period of 1993-2019. Gray-shade background highlights the super El Niño time periods 1996-1999 and 2013-2016 investigated in this study. In the upper plot warm (El Niño) periods are shown in red and cold (La Niña) periods are shown in blue.

4.2 Data and Methods

For our analyses we have selected the two strongest El Niño events of the last quarter century, in 1997/98 and in 2015/16, which are often called 'super' El Niño events[3] due to their extraordinary large magnitude (Fig. 18). From the numerous different indices characterizing the ENSO phenomenon, the Ensemble Oceanic NINO Index (ENS-ONI) has been selected which is an observation-based and real-time index given with monthly time resolution. The ENS-ONI index is determined by averaging sea surface temperature anomalies in an area of the east-central equatorial Pacific Ocean (Nino-3.4 region).

The global context of the tropical ENS-ONI index in Fig. 18 is exposed by the comparison of the record of global monthly mean surface temperature change from NASA[4], on the same time scale. This record is included here to show a well-known result that El Niño events transfer heat from the ocean to the atmosphere (Trenberth et al., 2002), a process that ultimately warms the global atmosphere. Accordingly, the peak El Niño times in Fig. 18 lead the maxima in global air temperature by times of order 2-3 months, with the largest peak temperatures linked with the two extreme events.

At the Nagycenk Geophysical Observatory (NCK, 47.6° N, 16.7° E) in Hungary the continuous recording of the SR spectral parameters corresponding to the vertical electric field began in May 1993 (see Section 1.2). The applied complex demodulation algorithm provides the frequency and the amplitude of the first three SR modes (Satori et al., 1996). Time periods with unrealistic spectral parameters, e.g. due to

---

[3] `https://www.webberweather.com/ensemble-oceanic-nino-index.html`

[4] `https://data.giss.nasa.gov/gistemp/graphs_v4/`

local weather conditions, were removed manually. We utilize this dataset over the four-year-long time period of 1996-1999 to investigate the evolution of the super El Niño event of 1997/98. Two-component magnetic observations at MIT's SR station in West Greenwich, Rhode Island (RID, 41.6° N, 71.7° W) are also used in case of this super El Niño event. Modal parameters for the SRs at RID are extracted from spectral intensity by Lorentzian fitting (Boldi et al., 2018; Mushtak and Williams, 2002).

Magnetic SR measurements at Hornsund (HRN, 77.0° N, 15.6° E), Eskdalemuir (ESK, 55.3° N, 3.2° W), Alberta (ALB, 51.9° N, 111.5° W) and Boulder Creek (BOU, 37.2° N, 122.1° W) stations were processed in the 4-year long time period of 2013-2016 to investigate the evolution of the super El Niño event of 2015/16. The HRN station is operated by the Polish Academy of Sciences at Svalbard, the ESK station by the British Geological Survey in the UK, and the ALB and BOU stations by the HeartMath Institute[5] in the United States and in Canada, respectively. These sites are equipped with a pair of induction coil magnetometers aligned with the geographical north-south direction (H_{NS}) and perpendicular to it (H_{EW}). The measurements were bandpass-filtered and 10 min-average spectra were generated for the two magnetic components separately. The weighted average method as in Musur and Beggan (2019) was applied to obtain the SR spectral parameters (intensity and frequency). Time periods with unrealistic spectral parameters were manually removed from the dataset. The SR data from the HRN station are not available between September 2015 and March 2016 due to technical reasons.

In this study we calculate the monthly average diurnal variation of the first SR mode's intensity (I_1) with 10-min time resolution, i.e. a (12x144) matrix characterizes each processed year (the 10-min time resolution yields 6x24=144 intensity values for each of the 12 months within a year). The main advantage of this approach is that in addition to highlighting the months with unusual SR intensity it provides the UT time characteristics of the anomaly as well, which has crucial importance in the interpretation of the results. In order to reveal possible ENSO-related variations in I_1(12,144) it is necessary to remove the substantial seasonal variation (see e.g., Satori, 1996) in the data. Therefore, we introduced a normalization process as follows:

$$I_{1,\mathrm{norm}}\ [\%] = 100\% \ \frac{I_1 - I_{1,\mathrm{av}}}{I_{1,\mathrm{av}}}\ , \tag{85}$$

where $I_{1,\mathrm{av}}$(12,144) denotes the 4-year average of $I_1(12, 144)$ (1996–1999 or 2013–2016). In practice, this means that the average value for all the months of e.g., January is removed from each of the four years to leave the residual value. Hereafter, we call this quantity "normalized SR intensity."

In order to support our SR-based results and to reveal the origin of the observed

---

[5] `https://www.heartmath.org/gci/`

anomalies in SR intensity, selected months of the two investigated time periods are analyzed based on independent data sets of lightning observations as well. Monthly averages of the 2.5° × 2.5° gridded flash number density (flash/km^2) data provided by the OTD satellite (Cecil et al., 2014) are applied for the time period of the super El Niño event of 1997/98 (neither OTD nor LIS data were available for the second event). In addition, monthly averages of 1° × 1° gridded World Wide Lightning Location Network (WWLLN[6]) flash rate (flash/1° × 1°) data, based on very low frequency (VLF) observations, are analyzed for the super El Niño event of 2015/16 (WWLLN data were not available for the first event).

4.3 Results

The interpretation of SR intensities as a global lightning indicator is not immediately straightforward to nonspecialists in meteorology and climate studies, and so some discussion on this aspect is appropriate in advance of the presentation of the results themselves. To interpret the SR-based results to be shown in Figs. 19-21 it is important to be aware of the characteristic diurnal variation of SR intensity which is strongly coupled to the diurnal variation of global lightning activity. The major part of global lightning is concentrated in the tropical continental regions, which can be divided into three main areas: the African, the American, and the Asian lightning "chimneys" (Christian et al., 2003). As the most intense time period of lightning activity corresponds to the afternoon hours in local time (Williams et al., 2000), the activation of the main lightning chimneys occurs separately in universal time. The maximum SR intensity corresponding to the Asian, the African, and the American chimneys are usually at around 8, 15, and 20 UT, respectively. This property of lightning activity is mirrored by the diurnal variation of SR intensity and makes it possible to distinguish the contribution of the different chimneys to the observed increase in SR intensity. It is important to note that an electric antenna is isotropic in its response and so for all wave propagation directions. In contrast, the magnetic coils are most responsive to electromagnetic waves propagating perpendicular to their orientation, and thereby they yield additional information about the direction of lightning activity connected to the observed anomalies in SR intensity.

4.3.1 Results Based on SR Measurements

Figure 19a shows the ENS-ONI index and Fig. 19b presents the normalized SR intensity variation of the E_Z field component at the NCK station between 1996 and 1999, a 4-year time period corresponding to the super El Niño event of 1997/98. The most conspicuous intensification in the normalized intensity of SRs occurs in February (∼70%) and in April (∼90%), clearly in the transition of ENSO from

---

[6] `http://wwlln.net`

the La Niña to its El Niño phase (Fig. 19a). The intensification is not uniform in UT time but maximizes near 10–14 UT (Fig. 19b) when the lightning in the Indo-Gangetic Plain in northern India is most active, a region previously highlighted for exceptional lightning activity (Albrecht et al., 2016; Cecil et al., 2014; Guha et al., 2017; Kandalgaonkar et al., 2005). In contrast, only minor intensification is evident during the warm phase in the normalized SR intensity which is more evident in November and December 1997 in Fig. 19b where the yellow colors replace the light blue ones. Later on, a notable suppression of activity is evident during the declining period of the warm phase (January, February, March, and April of 1998). The world maps show the location of the two distant SR stations: NCK (Fig. 19c) and RID (Figs. 19d and 19e). The vertical electric field component (E_Z) was measured at NCK and the two horizontal magnetic field components (H_{NS} and H_{EW}) were recorded in RID. The E_Z antenna is responsive to any direction while the induction coils are the most sensitive for the great propagational circle path perpendicular for the coil axis. The orange and green lines in the maps (Figs. 19d and 19e) indicate those directions. Diurnal variations of the first SR mode's intensity in April 1997 (red) are compared with April 1996 (blue) for the E_Z field component at NCK (Fig. 19h), for the H_{EW} (Fig. 19g) component, as well as for the H_{NS} (Fig. 19h) magnetic field components at RID, respectively. The SR intensity exhibits considerable increase in the E_Z field component at NCK between 06 and 16 UT with maximum intensity at 11 UT in April 1997 (Fig. 19f). The H_{EW} field component shows increased intensity at RID between 10 and 15 UT while the intensity of the H_{NS} field component shows little change between April 1996 and April 1997. On the basis that the H_{NS} field component (responsive to the African lightning activity at RID, see Fig. 19h), shows little change between April 1996 and April 1997, we can conclude that the increased SR intensity in the E_Z field component at NCK and in the H_{EW} field component in RID are attributable to the increased lightning activity in the MC and in India. That country has been shown to have the maximum lightning activity near 11 UT with a sustained period of decay thereafter (Chaudhari et al., 2010). The big difference between the SR response in E_Z at NCK and in H_{EW} in RID may be explained by the fact that the DC component of the electric field is not perfectly separated from the AC component (SRs) in the electronics of the preamplifier in case of large changes in the static field ($\geq$ 300 V/m). Both SRs and potential gradient measurements have been running in parallel at NCK (Bor et al., 2020) and the occasional contamination of SR intensity with anomalously increased PG values was demonstrated by Märcz et al. (1997). As was shown by Märcz and Satori (2005) the PG measurement at NCK was also responsive to the super El Niño of 1997/98. Therefore, a likely scenario is that the SR observations mirror both the variation in the AC (SRs) and the DC field connected with the super El Niño event of 1997/98 which enlarges the observed intensity in the first SR mode at NCK compared to the magnetic measurement at RID. This idea is supported by the observation that the percentage increase at the maximum of the mean diurnal intensity variation between April 1996 and April 1997 is smaller in the second (∼300%) and third (∼250%) SR modes than in the first mode (∼350%) at NCK (not presented here). In addition, the sunrise time at RID is near 10 UT and the SR intensity is diminished under nighttime condition before 10 UT due to the day-night asymmetry of the Earth-ionosphere cavity (Satori et al., 2007, 2016). The NCK station as well as the India and MC source regions are under daytime condition during the maximum lightning activity in those regions in April.

Figures 20 and 21 present the results for the super El Niño event of 2015/16. World maps are added to these figures to show the location of the widely separated SR stations: HRN, ESK (Fig. 20a) and ALB, BOU (Fig. 21a). The orientations of the magnetic coils and the propagation directions, for which the coils are the most sensitive, are also indicated. The $\mathrm{H_{NS}}$ and $\mathrm{H_{EW}}$ coils are marked consequently with green and orange colors, respectively. Figures 20b and 21b show the normalized SR intensity variations in the $\mathrm{H_{NS}}$ and $\mathrm{H_{EW}}$ magnetic field components between 2013 and 2016 while Figs. 20c–20e and 21c–21e present the diurnal SR intensity variation of selected months from the same time period.

The 2015/16 super El Niño event showed a substantially longer duration than the 1997/98 event (26 vs. 14 months, see Fig. 18). At the investigated stations the first remarkable SR intensification took place in September 2014, when the ENS-ONI index jumped from a near zero to a markedly positive value (Figs. 20b and 21b). The largest SR intensifications appear in the period December 2014–February 2015, when after a small decrease the ENS-ONI index starts to increase strongly again. This time period can be regarded as a second transition interval of the El Niño episode. The last transition month when conspicuous SR intensification is observed in the normalized SR intensity plots is April 2015.

Previous ENSO-lightning studies have focused on lightning enhancement in the peak El Niño (warm) phase rather than in the transition, and that bears checking for this case as well. Similar to the 1997/98 event, secondary SR intensification is evident near the maximum of the 2015/2016 super El Niño event. This can be seen in the September and December months of 2015 (yellow color) in the record from the ESK station in Fig. 20b and also in the interval September to December 2015 (yellow color, a few tens of percent enhancement) in the records from the BOU and ALB stations in Fig.21b. A notable suppression of activity is evident during the declining period of the warm phase (February, March, and April of 2016) just as in the case of the 1997/98 event in Fig. 19.

With a goal toward highlighting the interannual variations in SR signals, the

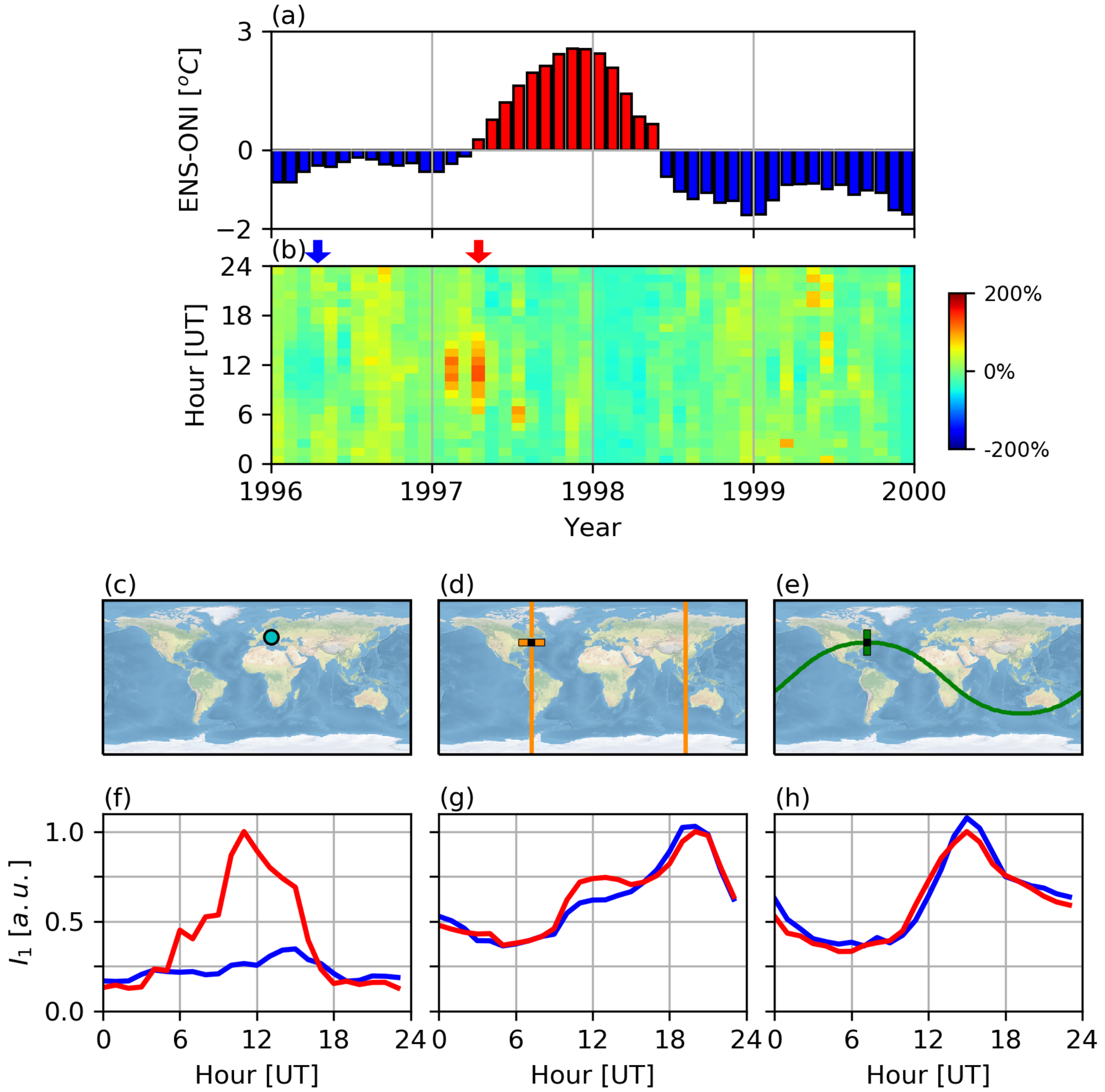

Figure 19: SR-based observations for the super El Niño event of 1997/98. **(a)** The ENS-ONI index and **(b)** the normalized SR intensity at Nagycenk (NCK) station between 1996 and 1999. The color scale represents the bipolar % deviations from the monthly/seasonal means of absolute intensity based on the 4-year period of SR observations (see Section 4.2 for more details). April 1996 and April 1997 are marked with a blue and a red arrow, respectively. **(c–e)** Maps with the locations of **(c)** NCK (for E_Z) and **(d and e)** RID (for H_{NS} and H_{EW}) stations. Panels **(d and e)** show the orientation of the magnetic coils (H_{NS} = green; H_{EW} = orange) and the propagation directions for which they are the most sensitive. **(f–h)** Diurnal variations of the first SR mode's intensity in April 1997 (red) as compared with April 1996 (blue) **(f)** for the E_Z field component at NCK, **(g)** for the H_{EW} as well as **(h)** for the H_{NS} magnetic field components at RID, respectively. The diurnal variations in intensity in **(f–h)** are all normalized to unity for the maximum value in April 1997.

diurnal variations of the first SR mode's intensity in the two magnetic field components at the four stations were selected in the same months (September, December, February) of four consecutive years, as shown for the HRN and ESK stations in Figs. 20c–20e as well as for the ALB and BOU stations in Figs. 21c–21e. Variation

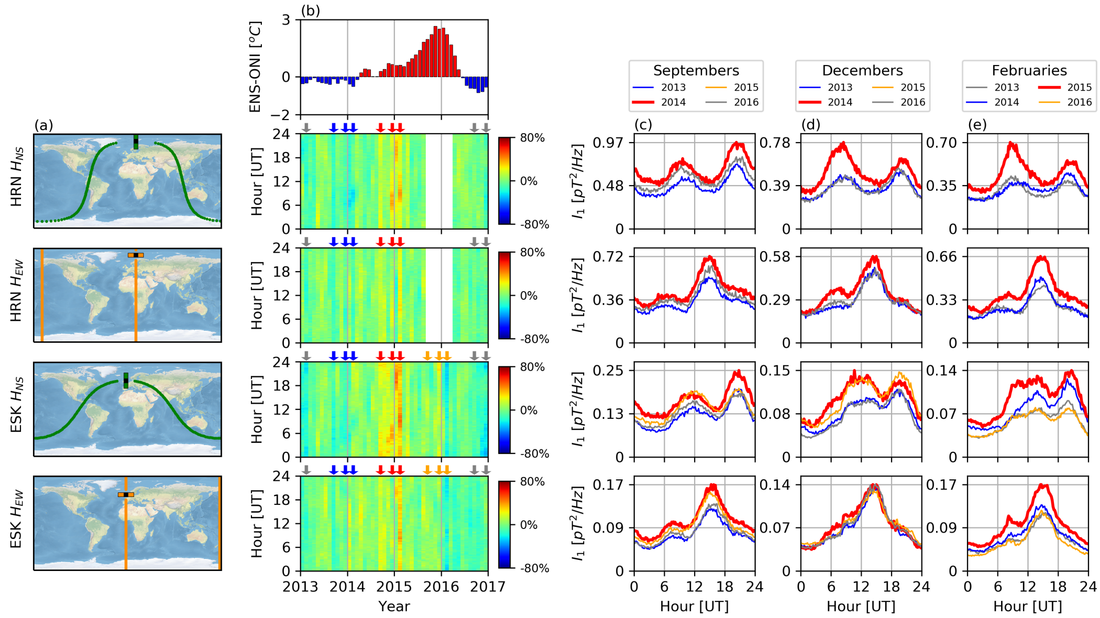

Figure 20: SR intensity at Hornsund (HRN) and Eskdalemuir (ESK) stations over the period 2013–2017. **(a)** Maps with the locations of the SR stations, the orientation of the magnetic coils ($\mathrm{H_{NS}}$ = green; $\mathrm{H_{EW}}$ = orange) and the propagation directions for which they are the most sensitive. **(b)** The ENS-ONI index (top) and the normalized SR intensity plots. The color scale represents the bipolar % deviations from the monthly/seasonal means of absolute intensity based on the 4-year period (see Section 4.2 for more details). **(c–e)** Diurnal variations of the first SR mode's intensity in pT^2/Hz for the two magnetic field components at the two stations (four panels in each column) in selected months: **(c)** Septembers, **(d)** Decembers, and **(e)** Februaries. The red curves in the panels of column **(c)** indicate September 2014, panels of column **(d)** December 2014 and panels of column **(e)** February 2015 (all are transition months indicated with red arrows in column b). **(c)** The orange curves refer to September 2015, **(d)** December 2015, and **(e)** February 2016 (all are in the main phase of the super El Niño of 2015/2016 indicated with orange arrows in the ESK-related portion of column b). The blue curves indicate **(c)** September 2013, **(d)** December 2013, and **(e)** February 2014 (all are in cold or neutral phase preceding the super El Niño of 2015/16 indicated with blue arrows in column b). The gray curves refer to **(c)** September 2016 and **(d)** December 2016 as well as **(e)** February 2013.

of SR intensity measured with two magnetic field components at four distant stations can capture the anomalous behavior of global lightning activity as the great circle paths shown in the maps cross one or more tropical chimney regions. The colored arrows in Figs. 20b and 21b show the selected months for diurnal analysis from the 4-year time window. The red color identifies the months in the transition period preceding the super El Niño of 2015/16, the orange color refers to the main phase of the super El Niño, the blue color represents the cold (neutral) period before the super El Niño event and the gray color indicates those months which are separated from the cold, transition, and main phase intervals but included in the 4-year normalization procedure. The diurnal SR intensities are greatest in the transition months (curves with red color) for all four SR stations and for both the

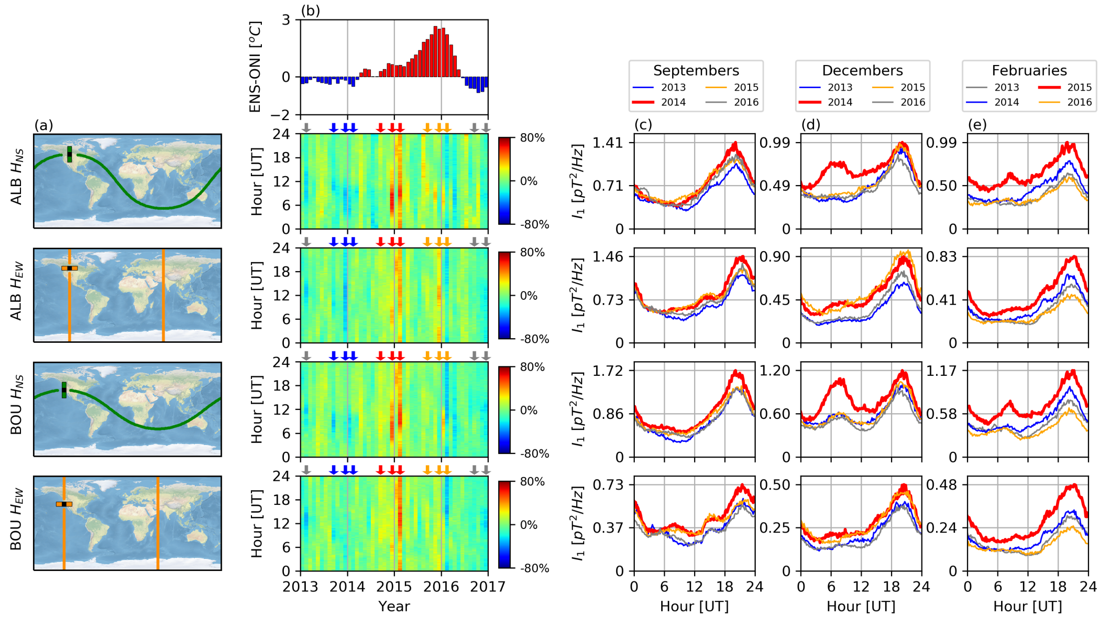

Figure 21: SR intensity at Alberta (ALB) and Boulder Creek (BOU) stations over the period 2013–2017. **(a)** Maps with the locations of the SR stations, the orientation of the magnetic coils (H_{NS} = green; H_{EW} = orange) and the propagation directions for which they are the most sensitive. **(b)** The ENS-ONI index (top) and the normalized SR intensity plots. The color scale represents the bipolar % deviations from the monthly/seasonal means of absolute intensity based on the 4-year period (see Section 4.2 for more details). **(c–e)** Diurnal variations of the first mode's SR intensity in pT^2/Hz for the two magnetic field components at the two stations (four panels in each column) in selected months: **(c)** Septembers, **(d)** Decembers, and **(e)** Februaries. The red curves in the panels of column **(c)** indicate September 2014, panels of column **(d)** December 2014 and panels of column **(e)** February 2015 (all are transition months indicated with red arrows in column b). The orange curves refer to **(c)** September 2015, **(d)** December 2015, and **(e)** February 2016 (all are in the main phase of the super El Niño of 2015/16 indicated with orange arrows in column b). The blue curves indicate **(c)** September 2013, **(d)** December 2013, and **(e)** February 2014 (all are in the cold or neutral phase preceding the super El Niño of 2015/16 and indicated with blue arrows in column b). The gray curves refer to **(c)** September 2016 and **(d)** December 2016 as well as **(e)** February 2013.

H_{EW} and H_{NS} magnetic field components, as shown in Figs. 20c–20e and 21c–21e. Consequently, a worldwide intensification of lightning activity occurred during the transition months. The diurnal SR intensity variations in the main phase of the super El Niño (curves with orange color) approached the level of SR intensities in the transition month of September and December (Figs. 20c, 20d, 21c, and 21d) and before the peak of the super El Niño. In the later declining warm phase of the super El Niño, in February 2016 (Figs. 20e and 21e), the SR intensity was greatly diminished. The level of diurnal SR intensity variations does decrease in the months of the cold period preceding the transition interval (curves with blue colors) and in the months at the beginning and end of the 4-year time window (curves with gray color). The great circle path at HRN and ESK in the case of the H_{NS} field component crosses the MC and West India (see Fig. 20a). Large SR intensity anomalies are attributed to these regions in the transition months: December 2014 and February 2015 (corresponding to the red curves in Figs. 20d and 20e). A huge increase (~80%–100%) of SR intensity in H_{NS} occurred at the HRN station near 8 UT when the MC shows the customary maximum lightning activity and an anomalously large increase of SR intensity appeared at the ESK station as well as a wide maximum centered near 12 UT when the Indian subcontinent shows the usual maximum lightning activity. The H_{EW} field component at HRN indicated a noticeable increase of lightning activity in the African chimney region at around 15 UT at both the HRN and ESK stations in the transition month of February 2015 (corresponding red curves in Fig. 20e). The H_{NS} field component at ALB and BOU are responsive to the lightning activity in Australia and the southeastern part of the MC (see the great circle paths in the maps of Fig. 21a). In the transition month of December 2014, a large increase (~100%–150%) of SR intensity was observed at these two stations near 7 UT, when these regions show the maximum lightning activity (corresponding red curves in Fig. 21d). A smaller response in SR intensity can be seen in February 2015 as well (corresponding red curves in Fig. 21e). A positive anomaly in SR intensity in the H_{EW} field component at the BOU station was observed near 21 UT in the transition month of February, 2015 (corresponding red curve in Fig. 21e). This anomaly could be attributed to the increased lightning activity nearby in the coastal region of Mexico.

4.3.2 Results Based on Independent Lightning Observations

The SRs are inherently a long-wavelength phenomenon and in single-station observations cannot resolve the sub-continental distribution of lightning sources. In order to further strengthen our SR-based results and to reveal the specific geographical regions from which the intensification of SRs predominantly originate we analyze lightning distributions provided by independent observational methods (satellite-based optical and ground-based VLF) in selected months when the strongest intensification in SRs is documented: April 1997 (Fig. 22) for the 1997/98 event as well as December 2014 (Fig. 23) and February 2015 (Fig. 24) for the 2014/15 super El Niño event. As references we use the lightning distributions from the same months but one year earlier: April 1996 (under La Niña condition) as well as December 2013 and February 2014 (under non-ENSO condition), respectively. We carry out this kind of analysis only for the Asian chimney region where the UT time distributions of normalized SR intensity shown in Figs. 19–21 provide evidence for the most probable locations of important changes in lightning activity.

High-flash-rate lightning activity was observed in Southeast Asia and the MC in the ENSO transition month of April 1997, with increased lightning activity also de-

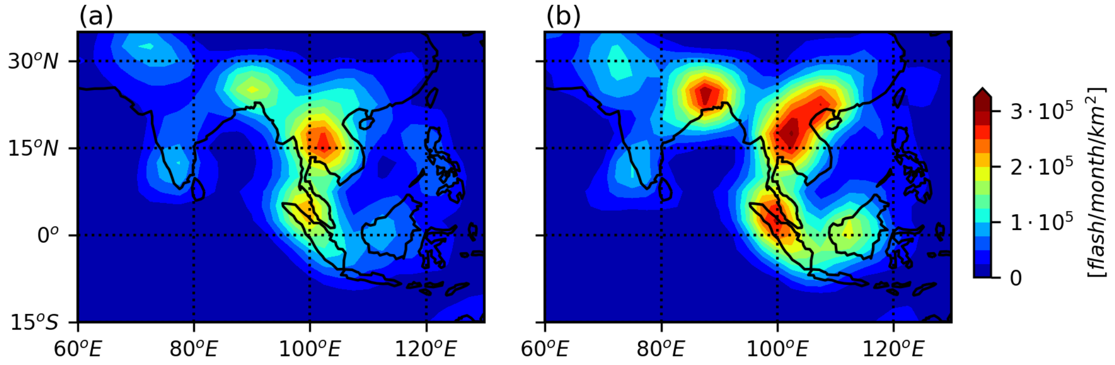

Figure 22: Flash number density for the Maritime Continent (MC) and India observed by the Optical Transient Detector satellite in **(a)** April 1996 and **(b)** April 1997. A ~35% increase in flashes was observed between April 1996 and April 1997.

tected in northeast India and the Himalaya region as observed by the OTD satellite (Fig. 22). The overall lightning increase for the MC in Fig. 22 between April 1996 and April 1997 amounted to ~35%. This behavior is consistent with the enhanced SR intensity documented in Figs. 19f and 19g in the same transition month, but with different percentage increments (~350% in E_Z at NCK and ~20% in H_{EW} at RID). The large percentage departures relate to the different methods for the lightning observations. In general, OTD underestimates the lightning activity in unsampled active regions over the monthly time scale but can identify weak flash characteristics (event/flash, group/flash, radiance/flash, duration/flash) in India (Beirle et al., 2014). The mean optical radiance per flash in India is only half of the global average (Beirle et al., 2014). Furthermore, higher optical radiance values are observed over Indonesia than over India (Beirle et al., 2014). Therefore, it is possible that the lightning activity can appear with different importance in the SR measurements based on ELF electromagnetic radiation of lightning and on the optical observation by the OTD satellite. The OTD activity was sustained for most of 1997 to the peak in the warm phase in November 1997 (but not shown here), while the SR-measured lightning diminished markedly after April 1997. This apparent discrepancy between two independent measures of lightning activity is not presently understood.

Given the evidence in multistation SR measurements shown in Figs. 20 and 21 for greater regionally resolved lightning activity in the ENSO transition months, and in recognition of the importance of oceanic lightning in this MC chimney, interest arose in the comparison with continuously available surface lightning network data. Observations from the WWLLN have been examined for two transition months (December 2014 and February 2015) over a wide area (90° E to 160° E and 35° S to 15° N) of the MC in Figs. 23 and 24, respectively. In both figures, comparison maps are made for the same months in two separate years, and for both daytime (10:00 a.m. – 10:00 p.m., centered at 4:00 p.m.) and nighttime (10:00 p.m. – 10:00 a.m., centered at 4:00 a.m.) conditions. Also included in each plot (Figs. 23e and 24e) are the local diurnal variations of the WWLLN-observed lightning strokes averaged over each month. Especially noteworthy in Fig. 23 is the marked increase in lightning activity over northern Australia and an average increase of ∼25% strokes from December 2013 to December 2014. Also noteworthy in Fig. 24 is the pronounced increase in activity over northwest Australia and the prevalent areas of activity immediately adjacent to land-ocean boundaries (Sumatra, Borneo, NW Australia, Gulf of Carpentaria (Australia)). The average increase in strokes in the transition month February 2015 is ∼15%. The full diurnal comparisons in both Figs. 23 and 24 show more lightning in the ENSO transition month in nearly every local hour.

In conclusion, based on independent lightning observations (OTD and WWLLN), lightning activity was more intense in the Asian/MC chimney region in the transition months of the two super El Niño events than in the same months of the preceding years under La Niña or non-ENSO conditions. These independent lightning observations are consistent with inferences based on SR observations with inherently coarser spatial resolution.

4.4 Discussion

The UT time distribution of the observed anomalies in SR intensity preceding the two super El Niño events show different characteristics. For the transition months of the 1997/98 super El Niño event the anomalies appear predominantly near 10–12 UT which is the characteristic activation time of the western part of the Asian chimney including the Indian subcontinent and Pakistan (Albrecht et al., 2016; Blakeslee et al., 2014). On the other hand, the SR intensity increases throughout the whole 0–24 UT time period in connection with the super El Niño event of 2015/16, which hints at a global response (i.e., all chimneys involved) in lightning activity. However, in this event the greatest increase of SR intensity often appears in the 6–12 UT period which again can be attributed to increased lightning activity in the specific regions of the Asian/MC chimney. In this respect the two super El Niño events are similar.

The known difference in the onset behaviors of the two super El Niño events (Lim et al., 2017) also appear in the SR intensity variations. The earlier event showed a simpler evolution. The anomalous increase of SR intensity is confined to a 2–3 month interval preceding the super El Niño event of 1997/98. This period of February to April coincides with the premonsoon time in India. On the other hand, the 2015/16 super El Niño occurred in two steps which is in line with our SR observations. The anomalous increase of SR intensity was first observed in September 2014 exactly when the ENS-ONI index turned from near zero to a markedly positive value. But then, in the subsequent months, the warm phase appeared to be aborting. The reignition of the 2015/16 super El Niño occurred in February 2015 and amplified

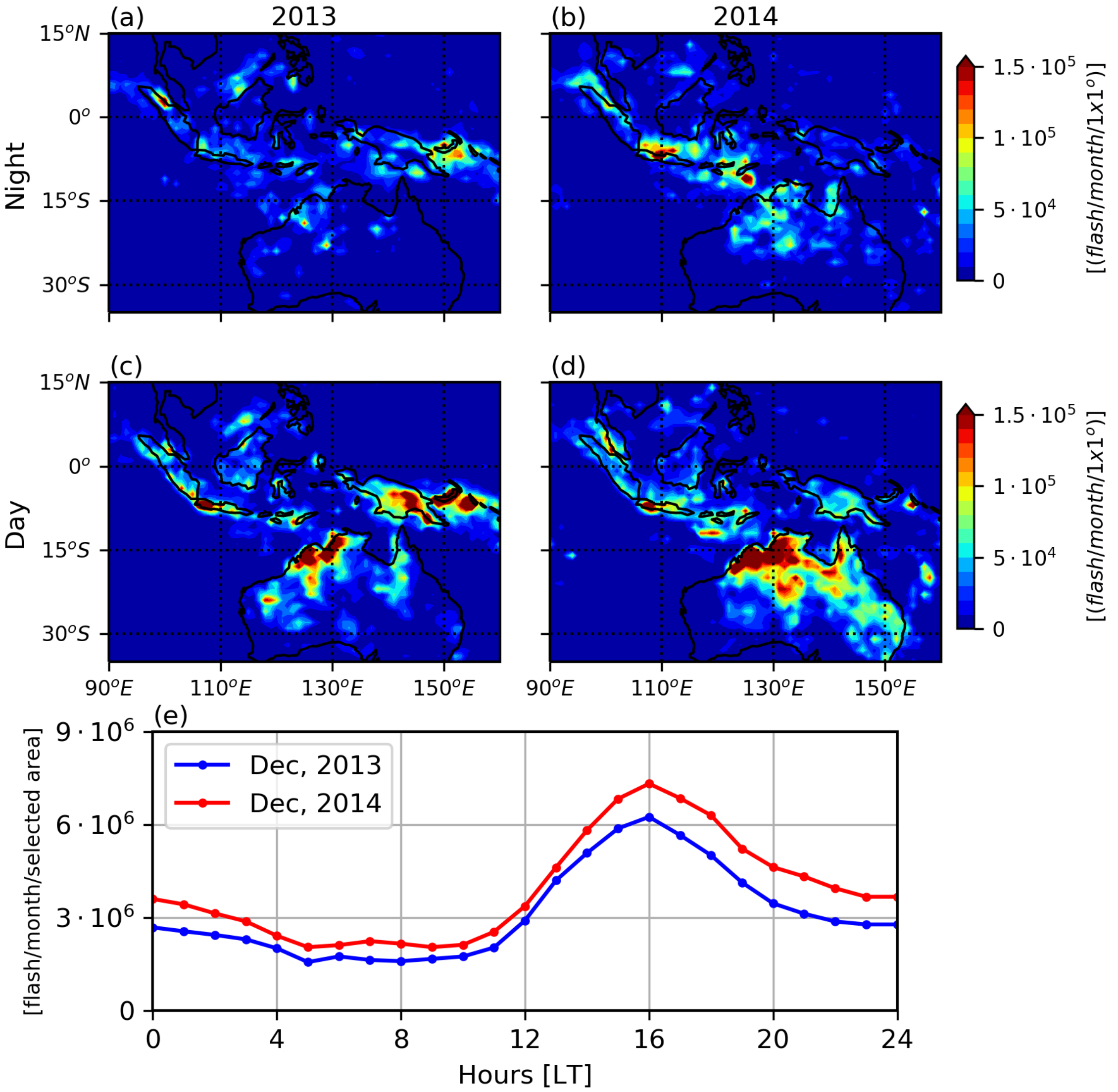

Figure 23: Flash rate observed by the World Wide Lightning Location Network (WWLLN) network in **(a)** December 2013 between 22 and 10 LT ("nighttime"), **(b)** December 2014 between 22 and 10 LT ("nighttime"), **(c)** December 2013 between 10 and 22 LT ("daytime"), and **(d)** December 2014 between 10 and 22 LT ("daytime") for the MC as well as northern Australia. **(e)** Diurnal variation in local time for the entire month of December, both during the cold phase (December 2013, blue) and during the transition to warm phase (December 2014, red). The conspicuous increase in lightning activity in Australia is consistent with the SR diurnal enhancements noted in the same month in Figs. 20 and 21.

this warm episode into a super El Niño by the end of 2015 (Chen et al., 2017; Dong and McPhaden, 2018). The anomalies in SR intensity already appeared in December 2014 and reached their maximum in February 2015. These observations strongly suggest that the SR intensity provides early evidence for the occurrence of the warm ENSO periods at least in the case of the strongest "super" El Niño-like events.

Many published studies address the ENSO-lightning relationship, and in most of

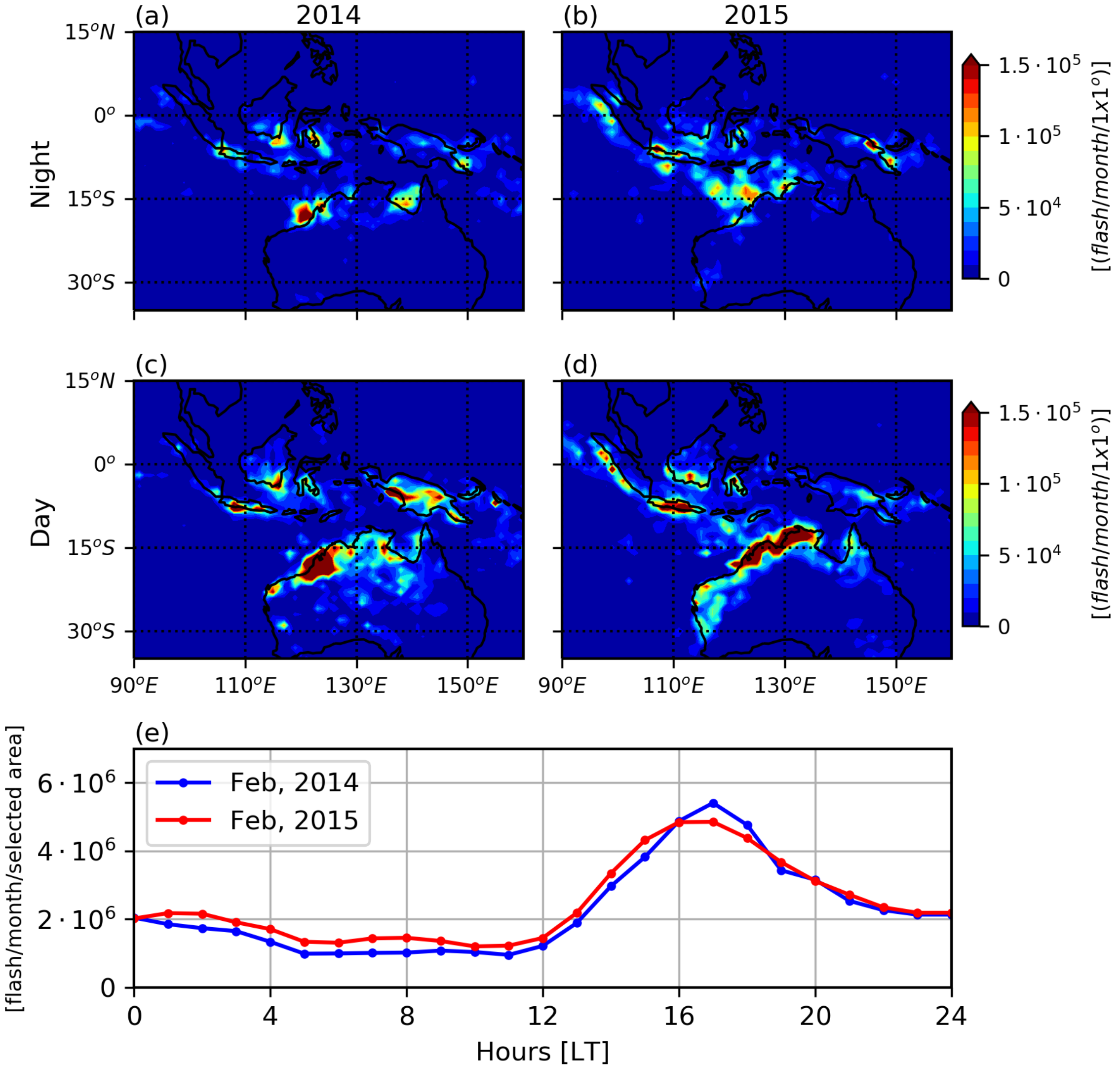

Figure 24: Flash rate observed by the WWLLN network in **(a)** February 2014 between 22 and 10 LT ("nighttime"), **(b)** February 2015 between 22 and 10 LT ("nighttime"), **(c)** February 2014 between 10 and 22 LT ("daytime"), and **(d)** February 2015 between 10 and 22 LT ("daytime") for the MC and including northern Australia. **(e)** Diurnal variation in local time for the entire month of February, both during the cold phase (February 2014, blue) and during the transition to warm phase (February 2015, red). Nighttime activity immediately adjacent to land regions is evident in many cases. The conspicuous increase in lightning activity in Australia in all but three LT hours is consistent with the SR diurnal enhancements noted in the same month in Figs. 20 and 20.

them the warm and cold phases are the exclusive scientific focus, not the transition periods. Some of these earlier studies refer simply to El Niño "years" and La Niña "years" (Kulkarni and Siingh, 2014; Kumar and Kamra, 2012; Tinmaker et al., 2017) while others select specific monthly sequences as "El Niño" and "La Niña" episodes, based on various ENSO temperature indices (Chronis et al., 2008; Hamid et al., 2001; Satori et al., 2009; Wu et al., 2012; Yoshida et al., 2007). But in either procedure the transition period from cold to warm phase, frequently amounting to several months, is either left out of the analysis, or a portion is included with the warm phase. One important exception is the study by Guha et al. (2017) in which emphasis is given to the warm-to-cold transition in the 2009/2010 ENSO event that can be seen in Fig. 18. Even in earlier studies making use of the pressure-based Southern Oscillation Index that considered only temperature and rainfall variations (e.g., Halpert and Ropelewski, 1992) over tropical continental regions, primary attention was given only to the "high" and "low" phases of ENSO, and not their transitions.

This documented focus in previous ENSO/lightning studies is understandable given the general interest in the response of lightning activity to surface air temperature (e.g., Williams et al., 2019). The El Niño periods exhibit the warmest SST anomalies and the La Niña periods the coolest ones. But the ENSO indices are continuously variable measures of SST imposed by the ocean, and the conspicuous lightning enhancements in the transition period points to thermodynamic/convective disequilibrium. Both the land surfaces and the atmospheric column are adjusting to the change forced by the increase in the temperature of the ocean that surrounds the land masses of the MC during the transition period. Both these adjustments can contribute to increased updraft strength in the deep moist convection that accounts for the lightning activity.

A long-standing assumption in interpretations of SR background signals from relatively compact chimney sources is that the measured intensity is proportional to the lightning flash rate (Boldi et al., 2018; Dyrda et al., 2014; Heckman et al., 1998). The SR/OTD and SR/WWLLN comparisons documented in Section 4.3.2 suggest that this assumption may not always be valid. Implicit in the linear relationship between SR intensity and flash rate is the invariance of the mean charge moment change (CMC) per flash but, in reality, this quantity could vary with meteorological scenario, including the phase of ENSO. The WWLLN is recording only high-energy ground flashes, and this may provide some explanation for why the interannual changes in WWLLN stroke rates (∼20%) are smaller than changes documented with SRs and optical methods. Further comparisons between SR intensity and flash rates measured by more conventional detection methods (optical and radio frequency) are needed to sort this out. Comparisons of this kind during the declining warm phase of the super El Niño events are particularly needed. The Global Lightning Mappers on GOES-16 and GOES-17 satellites will be particularly valuable in this regard as they provide the same continuous observations of specific regions that are also available with SR observations.

As previously noted, one of the main advantages of the SR-based monitoring of global lightning activity is that it does not suffer from the detection efficiency problems which are inherent with other lightning detection methods (Boccippio et al., 2000; Hutchins et al., 2012; Said et al., 2010). Lightning radiated waves in the SR band (< 100 Hz) have extremely weak attenuation (< 0.5 dB/Mm; Wait, 1996) and all lightning strokes with vertical extent contribute to the measured electromagnetic fields. However, to reveal the best possible CMC-based spatial distribution of global lightning corresponding to the months with increased SR intensity, a geophysical inversion algorithm ingesting multi-ELF-station spectral information is required (Nelson, 1967; Nickolaenko and Hayakawa, 2014). The inversion algorithm introduced in this work will hopefully contribute to the better understanding of variations in lightning activity on the ENSO timescale. Time series data from a large number of ELF receivers worldwide have been assembled for the period of the second super El Niño and inversion calculations are planned as a future effort.

4.5 Conclusions

In the present study we aimed to identify common signatures in the temporal evolution of two "super" El Niño events in 1997/98 and 2015/16 by investigating SR intensity. The analyses directed our attention to the transition months preceding these events when ENSO turned from the cold La Niña to its warm El Niño phase. Intensification of SRs occurred in the transition months preceding both super El Niño episodes, supporting a key role for thermodynamic disequilibrium and suggesting that SR intensity may play a precursory role for the occurrence and magnitude of these extreme climate events. In addition, SR intensity records mirrored also some of the important differences between the onset mechanisms of the two events. Our results suggest that the observed SR intensifications corresponding to the 1996/97 super El Niño event originate from Southeast Asia, the MC, and India while a global response of lightning activity is indicated for the 2015/16 super El Niño event. Indeed, the intensification of lightning activity has been confirmed in selected months by independent lightning observations as well. The peak El Niño times lead the maxima in global temperature by times of order 2–3 months, and consequently the major upsurge in lightning activity within the MC in the super El Niño events (preceding by ∼6 months the times of maximum ENS-ONI index) serves as predictions of peak global warming with lead times ∼9 months.

5 The Earth-ionosphere Cavity on the Solar Cycle Timescale

In this chapter long-term changes in the properties of the Earth-ionosphere cavity are inferred following Bozoki et al. (2021). On one hand these observations demonstrate how SR measurements can be used to investigate space weather related phenomena. On the other hand, the described space weather effects represent a challenge for the SR inversion task as one needs to handle them (e.g., to determine solar cycle dependent complex ionospheric altitudes) to get a realistic estimate for the intensity and distribution of global lightning activity.

5.1 Introduction

In 2015 long-term SR intensity records from the Ukrainian Antarctic station "Akademik Vernadsky" were published which clearly showed a pronounced solar cycle modulation (up to 60%) of SR intensity (Nickolaenko et al., 2015), just as in an earlier paper by Füllekrug et al. (2002) using data from the Antarctic station Arrival Heights. Recently, Koloskov et al. (2020) reported that SR intensity records at the Vernadsky station are still in phase with the solar cycle and that a new SR station began operation at Svalbard in the Arctic in 2013 that also shows the solar cycle modulation of SR intensity. The origin of this effect is a challenging question as satellite observations do not show a solar cycle variation in the intensity and distribution of lightning activity (which is recognized as the primary origin of SR intensity variations) (Christian et al., 2003; Williams, 2016; Williams et al., 2014a). Furthermore, there is little clear evidence reported in the literature so far regarding the direct influence of extra-terrestrial processes on SR intensity over shorter timescales which could form the basis of the longer-term modulation from the solar cycle. In studies by Williams et al. (2014a) and Satori et al. (2016) the authors argued that energetic electron precipitation (EEP) may account for the observed interannual SR intensity modulation by affecting the ionospheric height locally over the observer. As for the physical basis the authors suggested (following Sentman and Fraser, 1991) that the energy flux through the waveguide, parallel with the Earth's surface, must be conserved and when the local height is reduced by EEP, the magnetic field and attendant intensity must increase locally (a scenario illustrated in Fig. 33). However, before the paper by Bozoki et al. (2021) no direct evidence has been presented in the literature supporting the suggested EEP-effect on SRs either on the solar-cycle or on shorter timescales.

Energetic particles are trapped in the magnetosphere in radiation belts (RBs). They are heated to relativistic energies (from several tens of keV up to the order of

MeV) by various wave particle interactions (WPI), field line reconnection processes and large-scale electric fields (see e.g., Baker et al., 2018). Particle acceleration, as well as losses from pitch angle scattering into the atmosphere, can be intensified during geomagnetic storm periods in space weather events (Reeves et al., 2003). The characteristic timescale of single precipitation loss events reflects the duration of the causative source mechanism, and generally falls in the sub-second to hours range.

The expected effect of electron precipitation on SRs depends in part on the characteristic penetration depth of the electrons into the atmosphere (Satori et al., 2016) and the main factor determining the penetration depth of precipitating electrons is their energy (Rees, 1989), as illustrated in Fig. 25. Model calculations (Artamonov et al., 2017; Mironova et al., 2019a) show that the upper ("magnetic") boundary of the Earth–ionosphere cavity resonator (near 90–110 km) (Satori et al., 2005, 2016) is strongly affected by precipitating electrons in the 1–30 keV energy range. However, EISCAT incoherent scatter radar measurements show that the electron density can increase dramatically down to ∼70 km during strongly ionizing EEP events (Belova et al., 2005; Miyoshi et al., 2015). This observation suggests that electrons in the energy range of 30–300 keV can influence the upper ("magnetic") boundary of the Earth–ionosphere cavity resonator as well (Fig. 25). It is important to note that Fig. 25 illustrates only necessary conditions that energetic electrons will lower the local ionospheric height. Sufficient conditions involve the orders-of-magnitude increase in ionizing flux of energetic electrons, as discussed earlier for X-radiation (Williams and Satori, 2007).

The paper by Toledo-Redondo et al. (2012b) is a pioneering work on long-term quasi-global variations in the night-time height of the Earth–ionosphere cavity. Based on the extraction of the waveguide cutoff frequency in DEMETER satellite observations, the authors showed that the effective height of the waveguide was anti-correlated with the solar activity between 2006 and 2009.

A collection of simultaneously recording ELF stations is needed to characterize the deformation of the Earth–ionosphere cavity. In this work our first objective is to extend the published set of long-term SR intensity records by presenting new results from the high latitude ($|\text{lat}| > 60°$) stations: Hornsund (Svalbard), Syowa (Antarctica) and Maitri (Antarctica), from the mid-high latitude ($50° < |\text{lat}| < 60°$) stations: Eskdalemuir (United Kingdom) and Belsk (Poland), and from the low latitude ($|\text{lat}| < 30°$) station: Shillong (India), as well as an extended set of measurements from the high latitude Ukranian stations in the Arctic (Sousy) and Antarctic (Vernadsky). SR observations are compared with long-term fluxes of precipitating 30–300 keV electrons provided by the National Oceanic and Atmospheric Administration (NOAA) Polar Operational Environmental Satellites (POES) and with

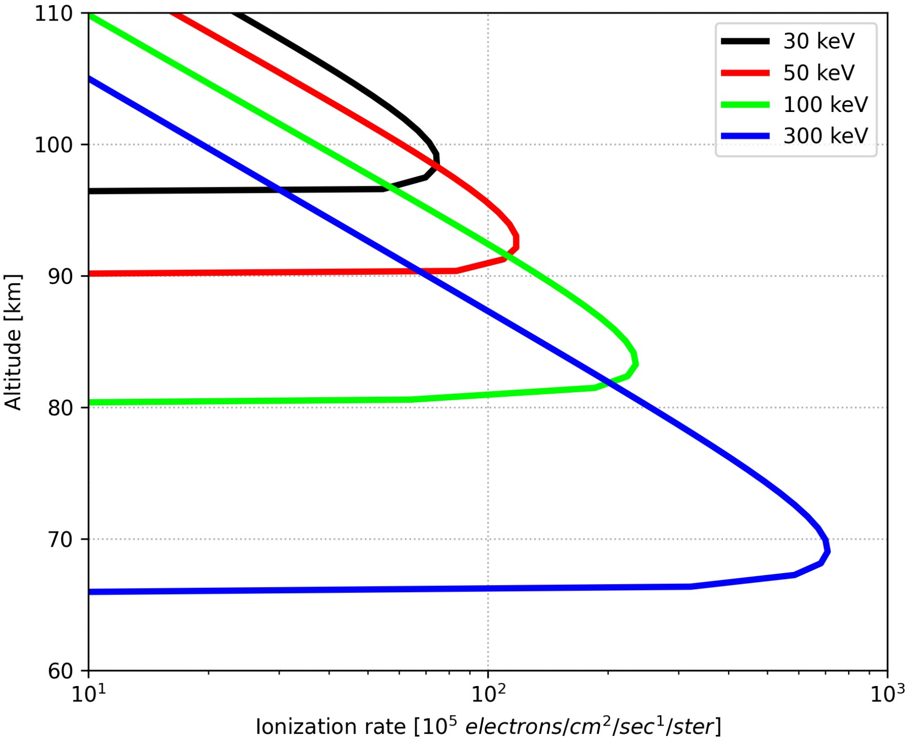

Figure 25: Ionization rates versus altitude for monoenergetic electron flux based on the models described in Artamonov et al. (2017) and Mironova et al. (2019a).

electron precipitation events identified in Super Dual Auroral Radar Network (SuperDARN) measurements in Antarctica (Bland et al., 2019). An extended set of the global waveguide's effective height, as observed in the survey electric field ELF-VLF spectra recorded by the French DEMETER satellite (Toledo-Redondo et al., 2012b), is also presented and analyzed.

5.2 Data and Methods

5.2.1 SR Data

In this work we present long-term induction coil measurements from eight different SR stations which observe the variation of the horizontal magnetic field in the lowest part of the ELF band and analyze monthly average magnetic intensities of the first SR mode. Figure 26 shows the location of the SR stations as well as the great circle paths (GCPs) of the wave propagation directions in which the coils are most sensitive. A common map is shown for the Hornsund and Sousy stations in Fig. 26 as these two stations are in close proximity (within 150 km, both at Svalbard) compared to the wavelength of ELF waves (of the order of 10 Mm). Induction coils are usually aligned with the local geographical meridian and perpendicular to it, except at the Syowa station where they are oriented along the geomagnetic north-south and east-west directions (Fig. 26f).

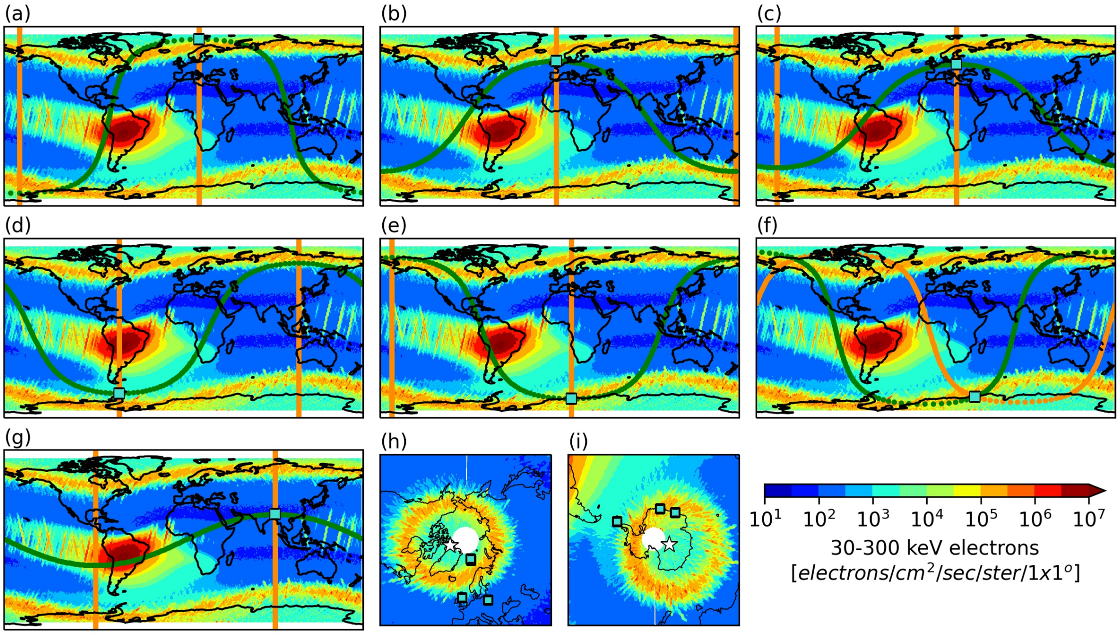

Figure 26: The location of the **(a)** Hornsund (HRN)/Sousy (SOU), **(b)** Eskdalemuir (ESK), **(c)** Belsk (BEL), **(d)** Vernadsky (VRN), **(e)** Maitri (MAI), **(f)** Syowa (SYO) and **(g)** Shillong (SHI) SR stations (turquoise squares) and the wave propagation directions (great circle paths) for which the coils are the most sensitive (H_{NS} = green, H_{EW} = orange). Note that at the SYO station the coils are oriented along the geomagnetic north-south and east-west directions. The background world maps show the distribution of precipitated 30–300 keV electrons in 1 × 1 degree spatial resolution in 2005 (yielding the highest precipitation fluxes in the time interval investigated in this study) provided by the NOAA-15 satellite. The polar views ($|\text{lat}| > 40°$) of the Northern **(h)** and Southern **(i)** Hemispheres together with the location of the high- and mid-high latitude SR stations and the geomagnetic poles (white stars).

The Institute of Geophysics of the Polish Academy of Sciences established SR measurements at the Polish Polar Station Hornsund at Svalbard (HRN; 77.0° N, 15.6° E; L=14.0; Fig. 26a) and at the Central Geophysical Observatory in Belsk, Poland (BEL; 51.8° N, 20.8° E; L=2.2; Fig. 26c) in 2004 and 2005, respectively (Neska et al., 2019, 2007). From the HRN station measured data were processed from September 2004 to October 2020. The main data gaps within this time period are: 06/2006-11/2007, 07-11/2008, 03/2009, 09/2009, 07-08/2011, 09/2015-03/2016 and 01-09/2017 (H_{EW}). From the BEL station the fully processed April 2005–December 2012 time period contains the following data gaps: 06/2005, 08/2005, 04-05/2006 and 01-02/2007. Since the entire dataset had been reprocessed for the present study we describe the applied data processing technique in detail.

Raw time series measurements were bandpass-filtered and 10-min estimates of average power spectral density (PSD) with a frequency resolution of ~0.2 Hz were generated by applying Welch's method (Welch, 1967). Welch's method estimates the PSD by dividing the data into overlapping segments, determining the PSD of each segment and averaging them. In order to minimize the aliasing effect of regional lightning activity and exceptionally intense lightning strokes generating Q-bursts (Guha et al., 2017) the PSD of data segments containing spikes greater than 40 pT in absolute value were omitted before averaging. From the obtained 10-min average PSD the intensity of the first SR mode was determined by means of the weighted average method (Nickolaenko et al., 2015). The peak frequency of the first mode (f_1) was calculated from the discrete PSD as:

$$f_1 = \frac{\sum_{6.5Hz}^{9.5Hz} f_k \cdot PSD_k}{\sum_{6.5Hz}^{9.5Hz} PSD_k}\,, \tag{86}$$

and the PSD of the nearest frequency value to this peak frequency was assigned as the intensity of the first SR mode.

SR measurements can easily be affected (contaminated) by different local noise processes (with natural and artificial origin), such as local lightning, wind, human activity, etc. (see e.g., Tatsis et al., 2021; Tritakis et al., 2021). In order to further improve the quality of the results a manual data sanitization step has been carried out before calculating the monthly averaged intensities. Our method relies on the evidence that the daily variation of SR intensity is usually highly similar within a month (Satori, 1996). Therefore the intensity of the first SR mode was plotted as a function of UT time for all the days within the processed month and days with unusual daily intensity variation were excluded when calculating the monthly average.

SR measurements are carried out by the British Geological Survey at Eskdalemuir Observatory (ESK; 55.3° N, 3.2° W; L=2.7; Fig. 26b) near the Scottish Borders of the United Kingdom since September 2012 (Beggan and Musur, 2018; Musur and Beggan, 2019). For the present study processed data are available from June 2012 to December 2020 with a few gaps in the record. Details about the station and data processing can be found in Musur and Beggan (2019).

The Institute of Radio Astronomy (IRA) of the National Academy of Sciences of Ukraine established observations at two high latitude SR stations in the Arctic and in the Antarctic, respectively. The Arctic station is located at the Sousy facility of the Tromso Geophysical Observatory (the Arctic University of Norway, UiT) at Svalbard (SOU; 78.1° N, 16.0° E; L=16.1; Fig. 26a) and began operation in September 2013 while the Antarctic station is located in the Western Antarctic at the Ukrainian station “Akademik Vernadsky” (VRN; 65.25° S, 64.25° W; L=2.6; Fig. 26d) and began operation in March 2002. From the SOU station data are available from September 2013 to August 2020 with data gaps in 04/2014, 05/2014, 07/2016 while from the VRN station data are available from March 2002 to April 2020 with one long gap between 09/2009 and 03/2010. For more information about the stations and data processing we refer to the paper of Koloskov et al. (2020). Here we note only that data segments with distorted SR spectra were removed from the VRN and SOU databases before averaging. From the VRN station an extended dataset of the spectral intensity at 11 Hz (between the first and second resonance peaks) is also presented (Koloskov et al., 2020). Later in this study we show that a substantial portion of long-term SR intensity variations are related to changes in the quality factor (Q-factor) of the Earth–ionosphere cavity, which characterizes the rate of energy dissipation at a given resonance mode (Kulak et al., 2003; Madden and Thompson, 1965). The investigation of spectral intensity between the first and second resonance peaks (near 11 Hz) is motivated by this observation as it is expected to have only a minor dependence on the Q-factor of the cavity. We note that recording at the frequency of about 11 Hz was originally proposed and implemented by Fraser-Smith et al. (1991).

The Indian Antarctic station Maitri (MAI; 70.8° S, 11.7° E; L=5.0; Fig. 26e) is located in the Eastern Antarctic and SR data from the station are available from March 2010 to December 2019 with data gaps in 04/2018, 11-12/2018 (H_{EW}) and 11/2019. It is important to note that at the Maitri station the magnetic coils were oriented initially along the geomagnetic north-south and east-west directions. However, by the end of 2012 they were reoriented along the geographic main directions. In order to work with a homogeneous dataset and to be consistent with the other SR stations, SR intensity values from Maitri are shown only from January 2013 in the present study. For more information about the station we refer to the paper by Manu et al. (2015). Low latitude SR measurements are available from the Shillong station (SHI; 25.92° N, 91.88° E; L=1.15; Fig. 26g) in India (Rawat et al., 2012) from January 2008 to December 2016 with data gaps in 07/2008, 05/2014 and 01-04/2015. Raw SR measurements from SHI were processed with the same technique as described for the HRN and BEL stations.

The induction coil magnetometers at the Japanese permanent research station Syowa (SYO; 69.0° S, 39.6° E; L=6.3; Fig. 26f) were set up in February 2000 and processed data are available for the present study from January 2006 to December 2015 with data gaps in 03/2008, 07/2008, 06-07/2014 and 06-08/2015. At the SYO station the coils are aligned with the geomagnetic north-south and east-west directions ($D=-48.5°$ in the year of installation). For more information about the station we refer to the paper by Sato and Fukunishi (2005). For the SYO data the same manual data sanitization process as for the HRN and BEL data has been applied.

5.2.2 EEP Observations

Satellite Measurements

The flux of precipitating $E > 30$ keV, >100 keV, >300 keV electrons is provided by the T0 telescope of the Medium Energy Proton and Electron Detector (MEPED) instrument (as part of the Space Environment Monitor 2 instrument package) onboard the NOAA-15 satellite (Rodger et al., 2010). Electrons that are detected by the T0 telescope (pointing outward along the local zenith) on the quasi-polar (98.70°), Sun-synchronous, low earth orbit (LEO) (~807 km) of the NOAA-15 satellite are in the atmospheric loss cone and will enter the atmosphere (Rodger et al., 2010). However, it is to be noted that the T0 telescope detects particles only near the center of the atmospheric loss cone and therefore underestimates the total flux of precipitating electrons (Mironova et al., 2019b; Rodger et al., 2010; van de Kamp et al., 2016).

To demonstrate the typical geographical configuration of the propagation paths (great circle paths) corresponding to the different SR stations and the electron precipitation-affected areas the distribution of precipitated 30–300 keV electrons (as a sum of the measured flux in the three corresponding channels of the T0 telescope) in 1 × 1 degree spatial resolution in 2005 (yielding the highest precipitation fluxes in the time interval investigated in this study) are displayed in the background in the subplots of Fig. 26. As can be seen on the maps three main areas are affected primarily by electron precipitation: two high latitude, zonally continuous stripes in the Northern and Southern Hemispheres which we will refer to hereafter as precipitation belts, and the South Atlantic Magnetic Anomaly in South America. Five of the investigated SR stations (HRN, SOU, VRN, MAI, SYO) lie very close (within 1 Mm and << the wavelength of the ELF waves) to at least one of these areas. Furthermore, some propagation paths cross the South Atlantic Magnetic Anomaly. The great circle path corresponding to the H_{NS} component at the SHI station needs to be highlighted as well which does not cross the precipitation belts at all. Furthermore, the South Atlantic Magnetic Anomaly is also very far from this measuring site. Therefore, we do not expect EEP-related local SR intensity changes in this H_{NS} component.

SuperDARN Measurements

A list of EEP events derived from the Syowa East SuperDARN radar was used to identify individual EEP-related anomalies in our SR records in June 2011. Although SuperDARN radars are designed primarily for detecting plasma structures in the E and F region ionospheres (Chisham et al., 2007; Greenwald et al., 1995), they can also be used to estimate HF radio wave attenuation in the ionospheric D region using an approach similar to riometry (Bland et al., 2018). In this study we use the EEP event list for the Syowa East SuperDARN radar described in Bland et al. (2019). This radar is located in Antarctica at 69.00° S, 39.58° E (geographic), so all of the June 2011 events were observed under night-time/twilight conditions.

5.2.3 Sunspot Number and AE Index

The traditional sunspot number is used to characterize the magnitude and length of the solar cycles and to identify the year(s) of the maximum and minimum solar activities. The auroral electrojet (AE) index is a measure of geomagnetic activity in the auroral zone (Davis and Sugiura, 1966) and is often applied as an indicator for EEP activity (e.g., Lam et al., 2010). These datasets are available from the OMNIWeb database (https://omniweb.gsfc.nasa.gov/form/dx1.html).

5.2.4 X-Ray Observations

The 0.1–0.8 nm X-ray measurements of the Space Environment Monitor (SEM) instrument onboard the GOES 10 and 15 satellites is used to characterize solar radiation-related changes in the Earth–ionosphere cavity (Satori et al., 2005, 2016). Monthly average flux values were determined from the 1-min and 5-min resolution datafiles available from NOAA's corresponding database (https://satdat.ngdc.noaa.gov/sem/goes/data/avg/).

5.2.5 Satellite-Based Observations of Waveguide Cutoff

Long-term variation of the upper boundary region of the Earth–ionosphere cavity resonator is also investigated in this study by using satellite-based wave recordings. The lower ionosphere forms the highly variable reflecting upper surface of the Earth–ionosphere waveguide (EIWG). Since far from the source, lightning impulses propagate in a guided manner, the effective height of the EIWG (reflecting altitudes) can be observed as suppressions in wave field strength at higher ELF, lower VLF frequencies around the cutoffs of distinct wave modes (see modeling details in Cummer, 2000; Ferencz et al., 2007). This effect is best recognized in case of the first guided mode at approximately 1.6 kHz, exhibiting often a lower intensity band in the spectrum of single impulses as well as in time averaged dynamic power spectra of the cavity background field (Toledo-Redondo et al., 2012b).

Due to the excitation of the lower ionosphere by waves in the EIWG with the above described character, the wide-band ELF-VLF wave records of LEO satellites also exhibit this specific spectral pattern. The electric field data of the French DEMETER satellite (Berthelier et al., 2006) with a polar LEO orbit has been utilized here to determine guided cutoffs, and thus to follow the change of the cavity's shape during approximately a quarter solar cycle period. Six years of night-time ELF-VLF spectra (whole years of 2005–2010) recorded at topside altitudes (660–710 km) between 65° geomagnetic latitudes have been analyzed. This uniquely rich, continuous ELF-VLF wave database is composed of power spectrum values under 20 kHz with 19.53 Hz resolution in frequencies and 2.048 s resolution in time (survey mode). Occurrences of wave power minima around the supposed cutoffs and their parameters (minimum frequency, sharpness, reliability factor) has been determined in consecutive spectrum vectors by applying a quadratic fit in the 1.4–1.95 kHz frequency range. The settings of the identifying algorithm have been fine-tuned by using a training set of several hundred of half orbits selected randomly from the whole recording base. In order to suppress noise and still maintain good spatial and temporal resolution, an averaged spectrum of eleven consecutive measurements was found optimal as input data. This step reliably finds the minima (if present) and yields approximately 1.5° spatial resolution in latitude. The effective height corresponding to the cutoff frequency is then determined by applying the condition for the transverse resonance of the waveguide (Toledo-Redondo et al., 2012b):

$$h_{\mathrm{eff}} = \frac{c}{2 \cdot f_{\mathrm{cutoff}}} \,. \tag{87}$$

We present annual averages of the effective height for different latitudinal domains. Raw data consisting of satellite coordinates, times at the mid positions of the averaged recording set and the parameters of the identified effect were stored for later analysis. The investigated domains consist of various geomagnetic latitudes: low- ($|\mathrm{mlat}| < 20°$), mid- ($20° \le |\mathrm{mlat}| < 50°$) and mid-high ($50° \le |\mathrm{mlat}| \le 65°$). Data points corresponding to the South Atlantic Magnetic Anomaly (defined as $-50° \le \mathrm{lat} \le 0°$ and $-90° \le \mathrm{lon} \le 50°$) were excluded when calculating the yearly averages.

5.3 Results

5.3.1 Results Based on SR Measurements

Multi-station Schumann resonance observations are used in this study to investigate long-term variations in SR intensity, selected year-to-year variations, and short-term variations attributable to single EEP events that affect both magnetic hemispheres. These topics are addressed in three separate sections below.

Long-Term Variations

Figure 27 displays the collection of SR intensity records available for the present study in the time window spanning about one and a half solar cycles between 2002 and 2020 (solar cycles 23 and 24) together with selected indicators of the solar and geomagnetic activity and of EEP. Subplot Fig. 27a shows the monthly average values of the sunspot number, the AE index and the X-ray flux. The EEP flux of 30–300 keV electrons in daily (black) and monthly (red) time resolution are shown in Fig. 27b. The EEP flux in daily time resolution is included to demonstrate its highly variable nature. The precipitation fluxes can vary by 3 orders of magnitude within

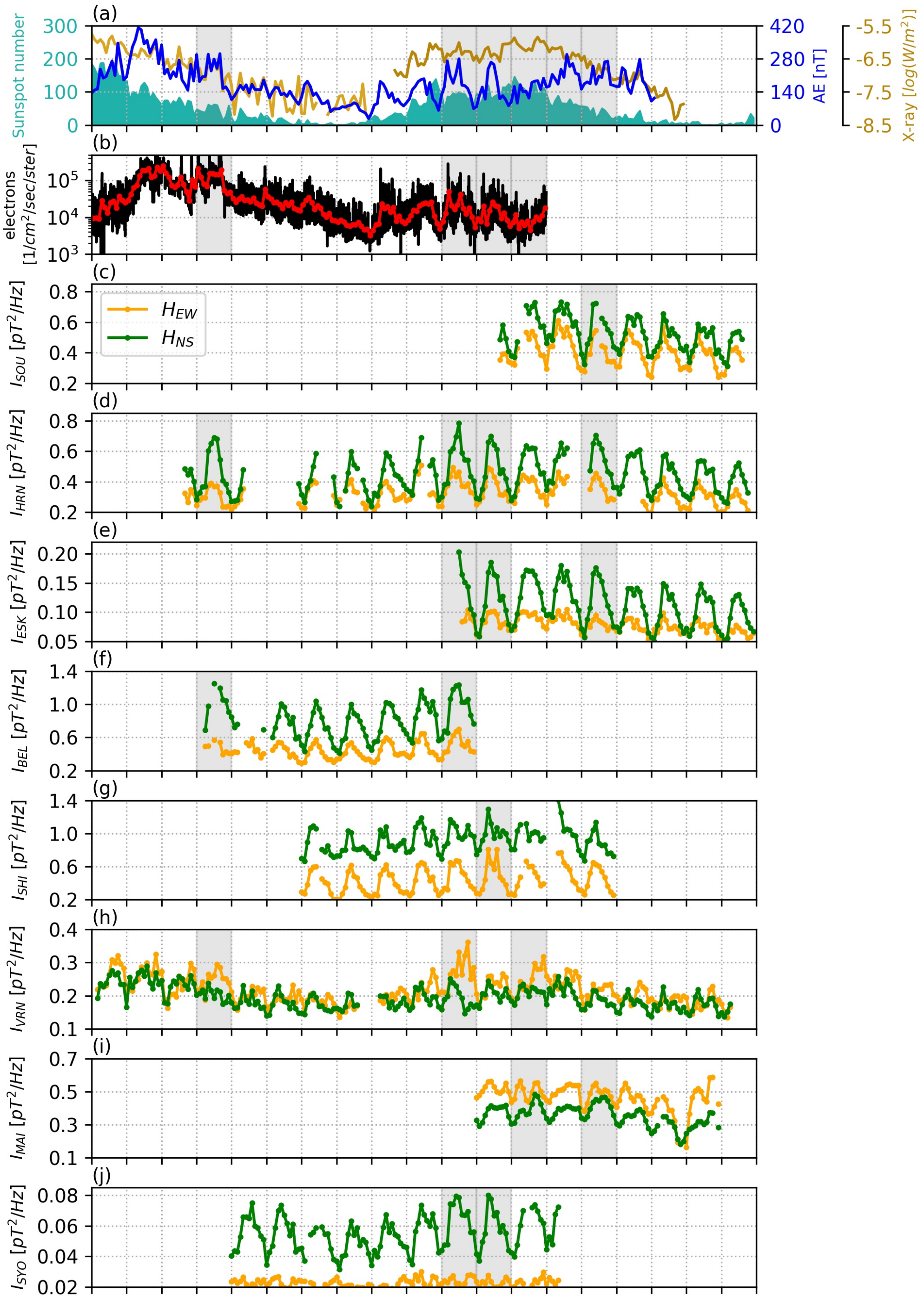

Figure 27: **(a)** Monthly average values of the sunspot number (turquoise), the AE index (blue) and the X-ray flux (GOES-10: gold, GOES-15: dark gold), **(b)** 30–300 keV electron precipitation fluxes in daily (black) and monthly (red) time resolution as well as the long-term records of the first SR mode's intensity in monthly time resolution at the **(c)** Sousy (SOU), **(d)** Hornsund (HRN), **(e)** Eskdalemuir (ESK), **(f)** Belsk (BEL), **(g)** Shillong (SHI), **(h)** Vernadsky (VRN), **(i)** Maitri (MAI) and **(j)** Syowa (SYO) SR stations. Gray background highlights years with exceptional SR intensities.

a few days during geomagnetic storms (Clilverd et al., 2007). The long-term records of the first SR mode's intensity in the H_{EW} and H_{NS} magnetic field components are shown in monthly time resolution from the Sousy (SOU), Hornsund (HRN), Eskdalemuir (ESK), Belsk (BEL), Shillong (SHI), Vernadsky (VRN), Maitri (MAI) and Syowa (SYO) stations in Figs. 27c-j. From the different stations SR data are available in the time windows described earlier.

As can be seen in Fig. 27a, the X-ray flux follows the time variation of the sunspot number in contrast to the AE index which has a distinct phase delay with respect to the solar maxima after 2002 and 2014/2015, and also shows extraordinary behavior in 2012 and in 2013 preceding the last solar cycle maximum in 2014. A good correlation is evident between the time series of the AE index and the 30–300 keV EEP fluxes as shown in Figs. 27a and b. We note that a moderate annual variation is present in both parameters with Northern Hemisphere (NH) summer maxima as noted in earlier works (e.g., Lockwood et al., 2020; Suvorova, 2017).

The SR intensity records in Figs. 27c–j show a complex behavior. On one hand a seasonal variation is present in the data with the highest intensity values usually observed in NH summer months. This general behavior is in accordance with the NH summer annual maxima in the magnitude of global lightning activity (Christian et al., 2003; Satori, 1996). We also note the presence of semi-annual variations (with spring and autumn peaks) at some SR stations (Satori and Zieger, 1996). The absolute level of SR intensity may show up to an order of magnitude difference station-by-station. We attribute this observation primarily to the different source-observer geometries but it could also hint to problems with the absolute calibration of the stations. Calibration issues are the most likely explanation for the eye-catching differences between the SR intensity records of the SOU and HRN stations which should be almost the same based on the close proximity of the stations.

On the other hand, the solar cycle modulation is evident at all SR stations and is in phase with the solar cycle (as indicated by the sunspot number). The solar cycle modulation of SR intensity is usually more pronounced in one of the magnetic field components: in the H_{EW} component at the VRN and SHI stations and in the H_{NS} component at the SOU, HRN, ESK, BEL, MAI and SYO stations. Years with exceptionally high SR intensities in these field components (in comparison with neighboring years) are highlighted with grey background in Figs. 27c–j: 2016 at the SOU; 2005, 2012, 2013 and 2016 at the HRN; 2012, 2013 and 2016 at the ESK; 2005 and 2012 at the BEL; 2013 at the SHI; 2005, 2012 and 2014 at the VRN; 2014 and 2016 at the MAI and 2012 and 2013 at the SYO stations. These exceptional years in SR intensity, which can be found in the declining phase of the solar cycles (2005, 2015, 2016) or in the vicinity of the solar cycle maxima (2012, 2013, 2014), are in agreement with enhanced levels of EEP as indicated by the AE index and the 30–300 keV EEP fluxes. As the solar cycle modulation of SR intensity is clearly present at the two mid-high latitude stations (ESK and BEL) and at the one low latitude (SHI) station as well, the effect is not confined to high latitudes.

The magnitude of the annual variation in SR intensity tends to follow the solar cycle as well. This behavior is in keeping with the suggestion of the solar cycle modification of cavity height. Higher magnitudes can be identified in the years near the solar maxima and smaller ones near the solar minimum (see Figs. 27c–j). This observation had been noted earlier for the total horizontal magnetic field by Koloskov et al. (2020). To take a closer look at this phenomenon we have removed the yearly averages from the VRN records for each (H_{NS}, H_{EW}) field component and plotted the residuals (ΔI) in Fig. 28. The solar cycle modulation of the annual SR intensity variation is different for the two field components at the VRN station. It is clearly more pronounced in the H_{EW} component for the one and a half solar cycle between 2002 and 2020. At the VRN station the H_{EW} component also shows the stronger modulation in its overall level (as compared to the H_{NS} component) (see Fig. 27h). The magnitude of the annual variation in the H_{EW} component is the largest in 2012, second largest in 2014 and third largest in 2002. The smallest magnitude appears near the solar minimum in 2008. The solar cycle modulation of the H_{NS} component is considerably smaller. Nevertheless, the minimum in the magnitude of the annual variation near the solar minimum in 2008/2009 and the maximum near 2012 is clearly visible in the H_{NS} component as well.

In order to quantify the solar cycle modulation of SR intensity we derived yearly averages and normalized them with the intensity values corresponding to the solar minimum year 2009 (δI) for the four SR stations exhibiting the longest records: HRN, SHI, VRN and SYO (Fig. 29). It follows that the 100% corresponds to the year 2009 for each component of each station in the figure. When calculating the yearly averages some missing values were determined with interpolation using the SR intensity values of the neighboring months (in case of 1 missing month) or based on the same months measured in the neighboring years (in case of >1 adjacent missing months). If neither of these two approaches was feasible for any year, that year was omitted. The long-term records of spectral intensity at 11 Hz are also displayed for each (H_{NS}, H_{EW}) field component from the VRN station in the same format.

As we stated earlier in this section, solar radiation-related changes in the Earth–ionosphere cavity are expected to follow the solar cycle (as indicated by the sunspot number) while EEP-related changes are expected to deviate from that cycle and to show a common behavior with the AE index. Next we investigate the normalized yearly average intensities displayed in Fig. 29 in this aspect. The relative SR intensity values corresponding to the first resonance mode generally follow the dif-

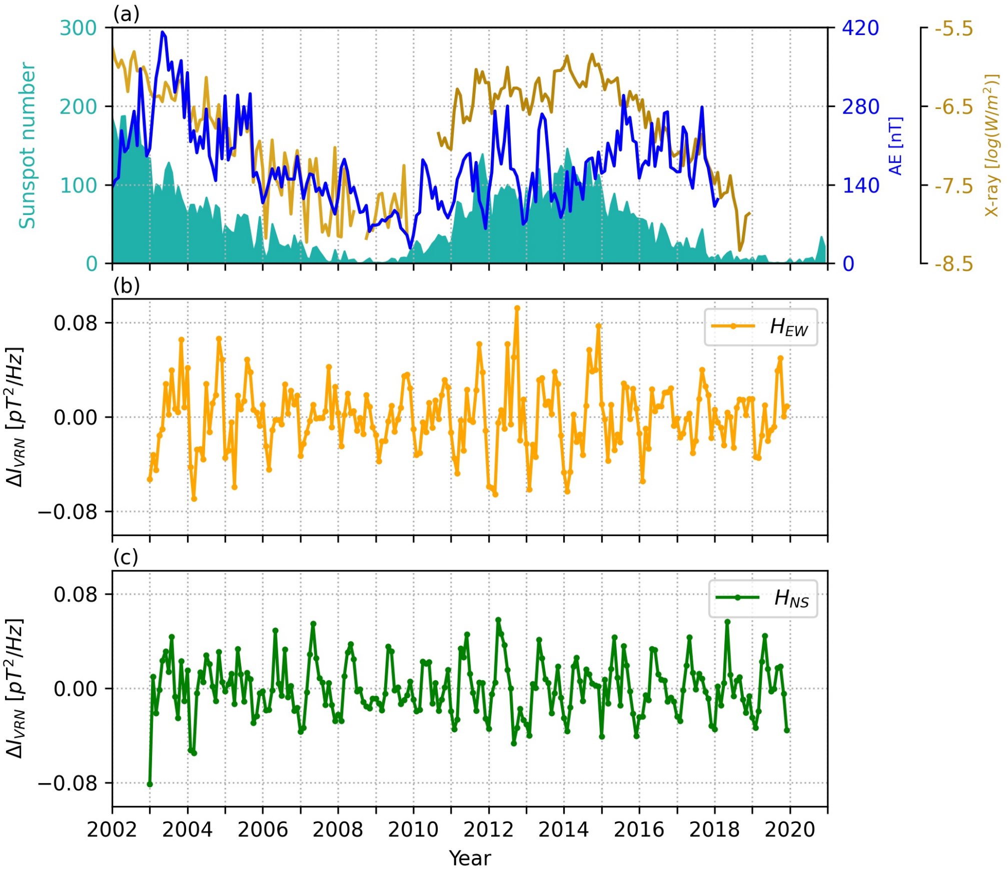

Figure 28: **(a)** Monthly average values of the sunspot number (turquoise), the AE index (blue) and the X-ray flux (GOES-10: gold, GOES-15: dark gold) as well as the residual monthly average SR intensities for the **(b)** H_{EW} and **(c)** H_{NS} components at the Vernadsky (VRN) station (see the main text for more details).

ferent phases of the solar cycle. However, this statement is mainly true for the field component exhibiting smaller long-term variability (H_{EW} at HRN and SYO, H_{NS} at SHI and VRN) while in the more variable field component (H_{NS} at HRN and SYO, H_{EW} at SHI and VRN) the largest intensity enhancements are present in years of AE extremities like in 2005, 2012 and 2015. In these years, intensity enhancements of ∼20–35% can be observed at the HRN, SHI and SYO stations while at the VRN station (showing the largest variation in intensity) the enhancements are as high as 40–60% (Table 4). We also note that the long-term record of the VRN station mirrors the magnitude difference between solar cycle 23 and 24, i.e. higher intensity values correspond to previous one. The year of 2012 yields the highest relative SR intensity values at all four SR stations. Regarding the relative SR intensity values corresponding to 11 Hz at VRN, the H_{EW} component shows enhanced values (∼20%) in the years of AE extremities (2005 and 2012) (Table 5) while the H_{NS} component exhibits a general decreasing trend throughout the investigated time period. The origin of this decreasing trend in the data is not clear at the moment.

Station	Component	2005 (%)	2009 (%)	2012 (%)	2015 (%)
HRN	H_{EW}	100	100	125	115
HRN	H_{NS}	120	100	135	130
SHI	H_{EW}	-	100	135	140
SHI	H_{NS}	-	100	120	120
SYO	H_{EW}	-	100	120	-
SYO	H_{NS}	-	100	135	-
VRN	H_{EW}	145	100	160	145
VRN	H_{NS}	120	100	110	125

Table 4: Normalized yearly averages of the first SR mode's intensity for the years 2005, 2009 (sol.min.), 2012 and 2015 (sol.max.).

Station	Component	2005 (%)	2009 (%)	2012 (%)	2015 (%)
VRN (11 Hz)	H_{EW}	120	100	120	115
VRN (11 Hz)	H_{NS}	105	100	100	90

Table 5: Normalized yearly averages of ELF intensity of 11 Hz at VRN for the years 2005, 2009 (sol.min.), 2012, 2015 (sol.max.).

Year-to-Year Comparisons

As confirmed by Fig. 29, it is not always the solar cycle maximum that yields the highest SR intensity values. This observation is in accordance with electron precipitation fluxes presented in Fig. 27b. In Fig. 30 we present the electron precipitation conditions for the Northern and Southern polar regions in the solar minimum year 2009, the solar maxima years 2002 and 2014 as well as in selected years with exceptionally high SR intensity values: 2005 and 2012, based on NOAA-15 electron precipitation fluxes. In general, the yearly averaged flux values go up and down together in all regions affected by EEP in the selected years. The year 2005 is in the declining phase of the 23^{rd} solar cycle while 2012 is close to the last solar maximum year of 2014. Electron precipitation is clearly the weakest in the solar minimum year of 2009 as expected. However, only a small (less than one order of magnitude) increase is noticeable from 2009 to the solar maximum year of 2014. The solar maximum year of 2002 yields larger fluxes than the solar maximum year of 2014 (around one order of magnitude larger compared to the solar minimum year of 2009). On the other hand, a remarkable increase of electron precipitation flux is identifiable in the selected years 2005 and 2012 yielding exceptionally high SR intensity values as well. The enhancement is around two orders of magnitude in 2005 as compared to the solar minimum year of 2009. This robust change in EEP flux is of the same order of magnitude as the variation of solar X-rays on the solar cycle timescale (Fig. 29a) (Satori et al., 2005; Williams and Satori, 2007).

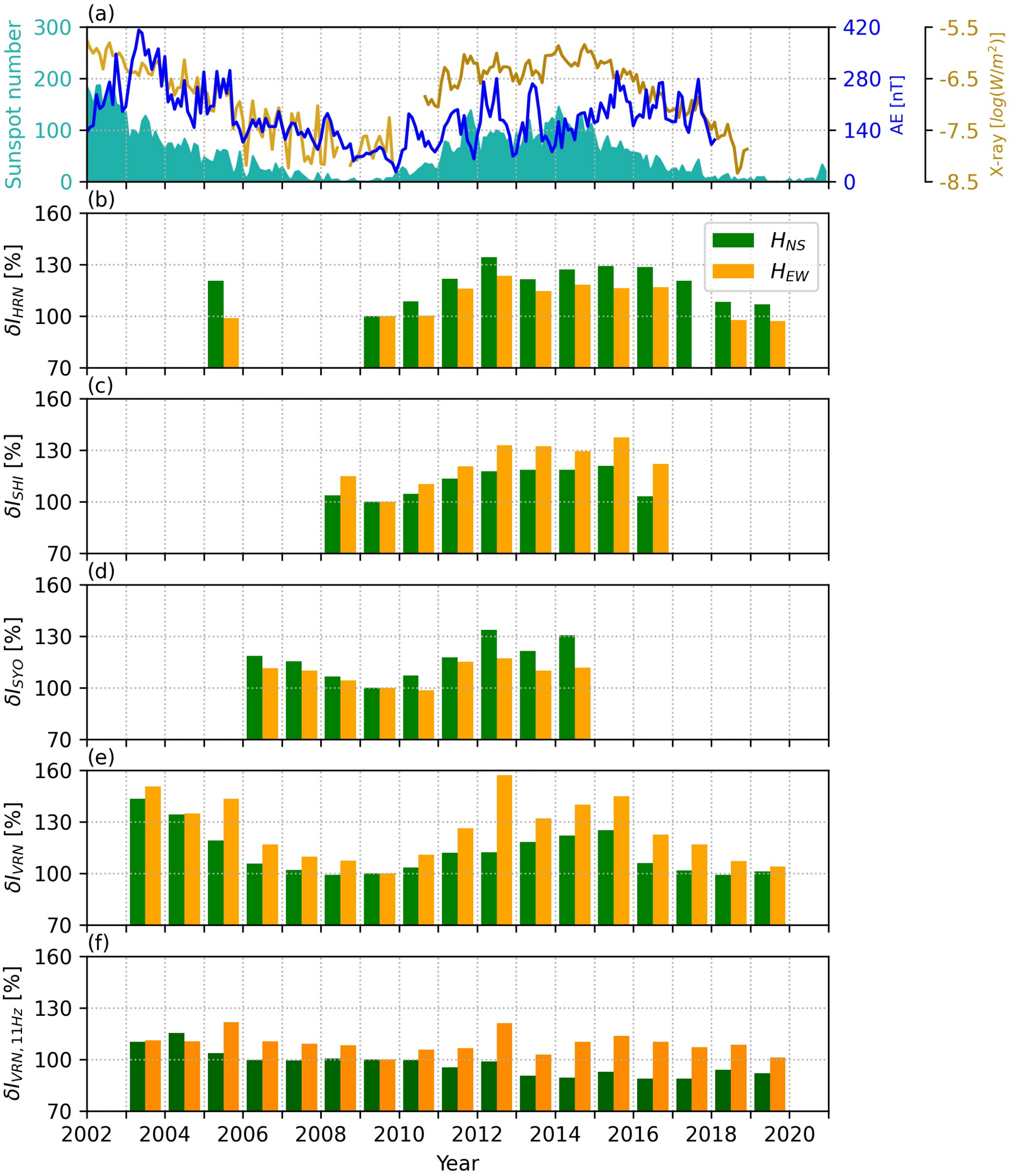

Figure 29: **(a)** Monthly average values of the sunspot number (turquoise), the AE index (blue) and the X-ray flux (GOES-10: gold, GOES-15: dark gold) as well as the normalized yearly averages of the first SR mode's intensity at the **(b)** HRN, **(c)** SHI, **(d)** SYO and **(e)** VRN stations and **(f)** of the intensity at 11 Hz at the VRN station.

Short-Term Variations Synchronous in Two Hemispheres

The well-organized motions of energetic electrons along the magnetic field lines suggest that EEP events and their associated cavity deformation may often be quasi-synchronous in the Northern and Southern Hemispheres. Figure 31 shows SR intensity records for two selected days from June 2011 (14 June and 23 June) together with independently identified EEP events based on Syowa East SuperDARN radar measurements from the event collection of Bland et al. (2019). To identify non-standard (not lightning-related) variations in the diurnal SR intensity records, quiet day diurnal SR intensity curves were determined for each field component of each station for June 2011. Quiet days were selected based on the AE index as days with AE values smaller than 400 nT. Figure 31 contains the average diurnal variation of these quiet days and in addition the corresponding standard deviations. In order to investigate whether EEP events are able to modify the global Q-factor of the Earth–ionosphere cavity resonator we applied the Lorentzian fitting technique (see e.g., Mushtak and Williams, 2002) on SR spectra from the Hornsund station. In Fig. 31 the extracted Q-factors are displayed in the same format as the SR intensity records.

On June 14, 2011 the strongest EEP event within the day can be observed between 09:20 and 14:30 UT at Syowa with radio wave absorption values greater than 2 dB (Fig. 31a). The event starts with a substantial increase of the AE index. SR intensity clearly increases during the event not only in the H_{NS} component at Syowa (so near the radar) but in the Northern Hemisphere under daytime conditions at the Hornsund (HRN) station as well where increased Q-factor values (by ∼10–30%) can be observed during the event. The relative increase of SR intensity is as large as 50–100% at Syowa during this event. On June 23, 2011 several strong (absorption > 3 dB) EEP events occured between 00:00 and 13:00 UT and one other event can be observed between 21:00 and 23:30 UT. The imprint of these events can be identified in both field components at SYO, in the H_{NS} component at HRN (with increased Q-factor values by ∼10–30%) as well as in the H_{EW} component at Vernadsky (VRN), even though the VRN station lies in a considerably different longitudinal sector than Syowa. This documented synchronous behavior provides evidence for the large spatial extents of the EEP events (∼4 h magnetic local time extent).

5.3.2 Results Based on DEMETER Measurements

The effective height of the Earth–ionosphere waveguide as inferred from DEMETER satellite measurements of the waveguide cutoff frequency at night-time (see Section 5.2.5 for details) can be regarded as a quantity providing an independent view on the deformation of the Earth–ionosphere waveguide. Figure 32 shows the

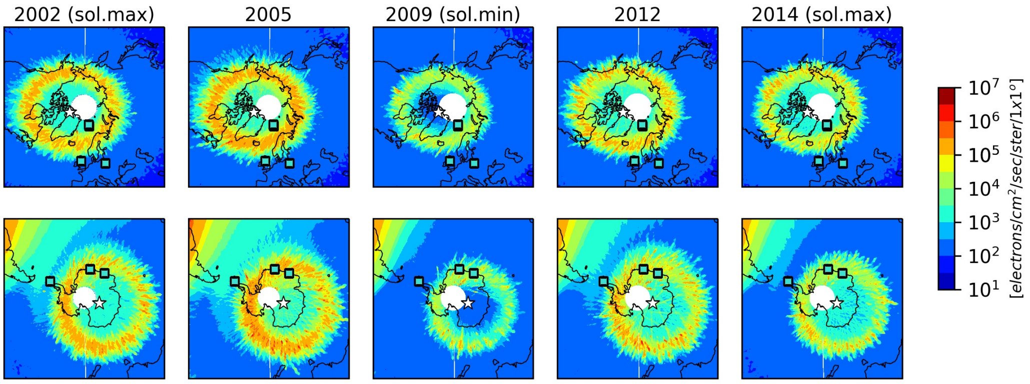

Figure 30: The distribution of precipitated 30–300 keV electrons for the Northern (top row) and Southern (bottom row) polar regions for the years 2002, 2005, 2009, 2012 and 2014, together with the location of the high and mid-high latitude SR stations and the geomagnetic poles (white stars).

yearly average values of the effective height from 2005 to 2010 corresponding to low-, mid- and mid-high geomagnetic latitudes. In general, the Earth–ionosphere waveguide height seems to be the lowest at mid-high latitudes while it is the highest at midlatitudes with average height values of 90.4 and 91.8 km, respectively. The effective height is also smaller at low latitudes (90.7 km) as compared to midlatitudes (91.8 km). Regarding the long-term trend in the data, the solar cycle variation is evident in all the investigated domains. Table 6 summarizes the relative height differences between 2005 and the solar minimum year of 2009 for low-, mid- and mid-high geomagnetic latitudes. The relative height difference is the greatest at mid-high latitudes (which represent the highest observed latitudes in this case) (2.2%) and the smallest at low latitudes (1.2%).

$\lvert \mathbf{mlat} \rvert < 20°$	$20° \leq \lvert \mathbf{mlat} \rvert < 50°$	$50° \leq \lvert \mathbf{mlat} \rvert \leq 65°$
1.2%	1.3%	2.2%

Table 6: Relative differences in the waveguide's effective height between 2005 and the solar minimum year of 2009 for low-, mid- and mid-high geomagnetic latitudes.

5.4 Discussion

In this section, we suggest a general interpretation for the results obtained, before attempting to estimate the height changes of the Earth–ionosphere cavity associated with EEP. Finally, we describe the most important characteristics of our SR- and DEMETER-based results.

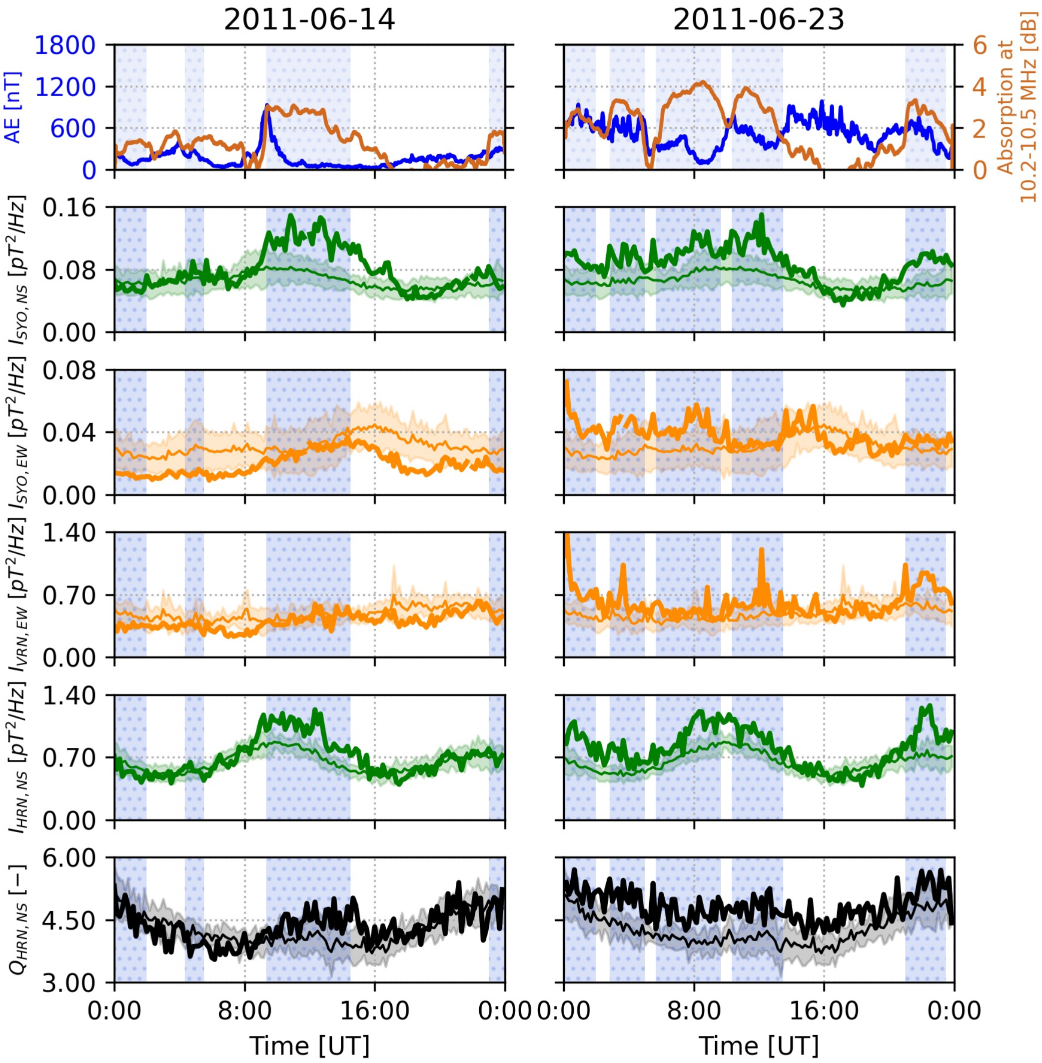

Figure 31: Comparison of EEP events (with respective time intervals shaded and dotted) identified in Syowa East SuperDARN radar measurements by Bland et al. (2019) and SR intensity records (H_{EW}: orange, H_{NS}: green) for June 14, 2011 (left column) and June 23, 2011 (right column). The top row shows the time variation of the AE index (blue) and the radio wave absorption values in the D-region (red) at 10.2–10.5 MHz as inferred from the radar measurements. SR intensity records from the SYO, VRN and HRN stations for the selected days (thick curves) are displayed together with the average diurnal variation of quiet days (thin curves in same color) and the corresponding standard deviations (same color shaded area) (see the main text for more details). The last row of the figure shows Q-factor records from the HRN station that tend to be enhanced during EEP events.

5.4.1 Solar X-Rays and EEP: The Two Main Effects to be Considered

In order to interpret correctly the obtained results it is first important to state that although SR intensity variations are generally connected with changes in the distribution and/or intensity of global lightning activity, satellite observations of lightning activity do not show any significant solar cycle variation on the global scale (Christian et al., 2003; Williams et al., 2014a). This is in line with the observation

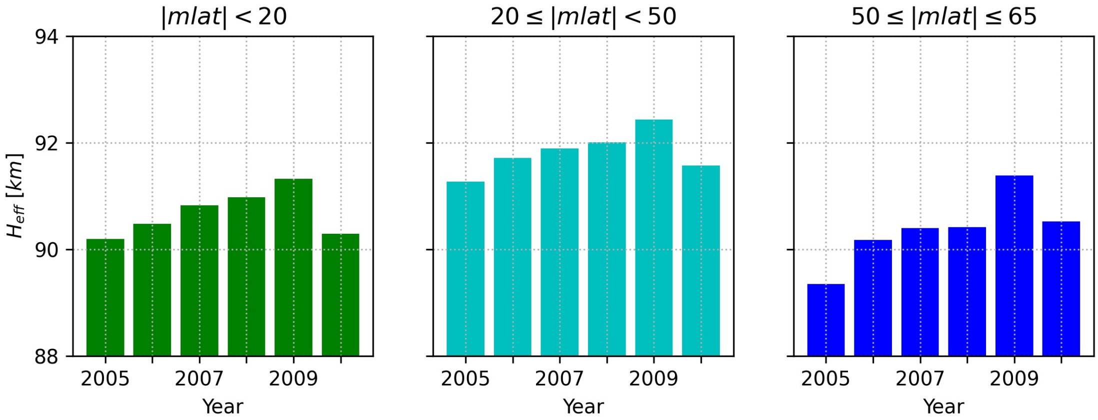

Figure 32: Yearly averages of the Earth–ionosphere waveguide's effective height based on DEMETER observations. A similar solar cycle modulation is evident in each of three latitude ranges.

that the total energy output from the Sun varies on the order of 0.1% throughout the solar cycle (Fröhlich and Lean, 1998). Therefore, the solar cycle modulation of SR intensity needs to be accounted for by long-term changes in the properties of the Earth–ionosphere cavity, i.e., by changes in the propagation conditions of ELF waves. As the solar cycle variations in Galactic Cosmic Rays (GCR) is considered to have only a negligible effect (<1%) on the intensity of SR (Satori et al., 2005) hereafter we discuss the possible effects related to the Sun.

Two fundamental mechanisms can be distinguished for the Sun-related impact on the near-Earth environment: one based on photons and the other on charged particles. The majority of solar photons arrive in the Earth's equatorial zone while charged particles precipitate in the upper atmosphere in the high latitude precipitation belts and in the South Atlantic Magnetic Anomaly (Fig. 26). The long-term behavior of these two effects is markedly different on the solar cycle timescale. While the flux of solar photons generally follows the solar cycle, the precipitation of charged particles does not (Asikainen and Ruopsa, 2016) (Fig. 27). We documented both of these behaviors in long-term SR intensity records of different field components at different stations (Fig. 29). Therefore, we suggest that a combined effect of photons and charged particles needs to be considered to account for all our SR-based observations (as illustrated in Fig. 33).

The long-term solar cycle modulation of the Earth–ionosphere cavity by solar X-rays had been first documented by Satori et al. (2005) based on long-term SR frequency records. Both SR frequencies and Q-factors observed at different stations exhibited maxima during the two solar maxima in 1992 and 2002 and minima in 1996. The observed variations were interpreted on the basis of a uniform cavity and the presence of two characteristic ionospheric layers (Greifinger and Greifinger, 1978; Mushtak and Williams, 2002). The height and scale height of the lower (electric) layer were considered to be invariant over the solar cycle while for the upper

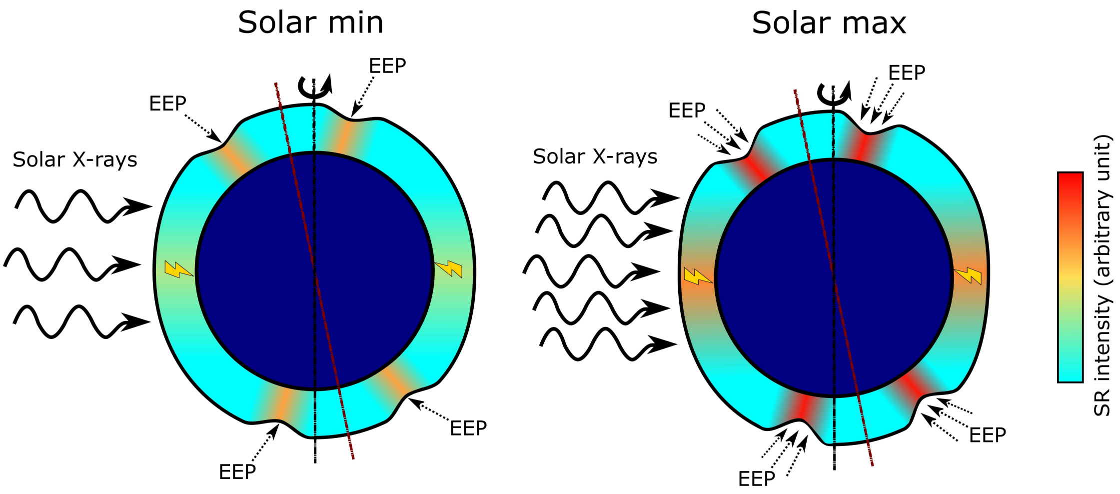

Figure 33: Illustration of the deformation of the Earth–ionosphere cavity at solar minimum (left) and solar maximum (right). At solar maximum X-rays and EEP reduce the cavity height more significantly (dominantly over low- and high latitudes, respectively) which results in enhanced SR intensity values beneath the deformed regions.

(magnetic) layer the authors inferred a height decrease of 4.7 km and a scale height decrease from 6.9 to 4.2 km for the first SR mode from solar maximum to solar minimum. These changes result in an increase of the resonator's Q-factor by 12–15% (Satori et al., 2005). The intensity of a damped simple harmonic oscillator is known to be proportional to the square of its Q-factor (Feynman et al., 2010), in agreement with the theoretical description of SR (Eqs. 2–24 in Nelson, 1967; Williams et al., 2006). It follows that a 12–15% change in the Q-factor of the Earth–ionosphere cavity can result in a 25–30% increase of the first SR mode's intensity. This estimate is in agreement with the relative SR intensity values corresponding to the H_{NS} component at the SHI and VRN stations (Fig. 29). As the Q-factor is a general property of the Earth–ionosphere cavity this effect should contribute to the long-term SR intensity variation at all SR stations around the globe.

The phenomenon involving charged particles deposited into the atmosphere through various heliophysical and geomagnetic processes is called energetic particle precipitation (EPP). EPP covers a wide variety of charged particles but protons and electrons are the two main constituents to be considered with significantly high fluxes (Mironova et al., 2015). As it has been stated in earlier works (Satori et al., 2016; Williams et al., 2014a) proton events are too sporadic in time to yield the observed persistent long-term modulation of SR intensity. Therefore, we consider the precipitation of electrons hereafter which is usually referred to as energetic electron precipitation (EEP).

The expected effect of EEP on SRs strongly depends on the characteristic penetration depth of the electrons into the atmosphere. SRs are primarily responsive to two specific altitude regions where the ionospheric dissipation is predominant (Satori et al., 2016). These are usually referred to as the electric (capacitive) and magnetic (inductive) heights (Greifinger and Greifinger, 1978; Madden and Thompson, 1965) to be found at around 50–60 km and 90–110 km altitudes, respectively (Greifinger and Greifinger, 1978; Kulak and Mlynarczyk, 2013; Mushtak and Williams, 2002). The main factor determining the penetration depth of precipitating electrons is their energy (Fig. 25). Model calculations show that the magnetic height can be affected by electrons in the 1–30 keV energy range while the electric height only by electrons with energy above 300 keV (Artamonov et al., 2017; Mironova et al., 2019a; Rees, 1989; Satori et al., 2016). However, EISCAT incoherent scatter radar measurements show that in connection with EEP the isopycnic surfaces of electron density can occasionally descend by some tens of kilometers in the high latitude D- and E-region (Belova et al., 2005; Miyoshi et al., 2015). To account for such a large decrease in the SR magnetic height the effect of 30–300 keV electrons needs to be considered as well. Generally, it is true that the lower the energy of electrons the higher the precipitated flux and the more continuous the precipitation in time (Lam et al., 2010). Therefore, to account for the long-term modulation of SR intensity, electrons in the 1–300 keV energy range (affecting the magnetic height of SR) are the best candidates. This energy range covers both auroral and radiation belt electrons (Mironova et al., 2015). EEP is expected to affect the height of the Earth–ionosphere cavity and the measured magnetic field locally where precipitation occurs consistent with the conservation of energy flux (Satori et al., 2016; Sentman and Fraser, 1991; Williams et al., 2014a). A permanent local decrease in the magnetic height is expected to modulate the amplitudes of all natural variations in SR intensity on all timescales as shown for the magnitudes of the annual variation in Fig. 28.

We also showed that EEP events are able to modify the Q-factor of the Earth–ionosphere cavity (Fig. 31) which is in line with our observation that they can affect both hemispheres as well as large longitudinal regions. This effect may result in globally observable changes in SR intensity but this aspect needs to be investigated further in the future. It is possible that the long-term 12–15% change in the Q-factor of the Earth–ionosphere cavity documented by Satori et al. (2005) may involve EEP-related changes as well.

Two important pieces of evidence were shown in this thesis for an EEP-related deformation of the Earth–ionosphere cavity. First, exceptional increases of SR intensities were documented in certain years, as in 2005 and 2012 (Fig. 29), which are not solar maximum years, but are characterized by enhanced electron fluxes (Fig. 30). Based on satellite observations Asikainen and Ruopsa (2016) reported on enhanced electron precipitation at >30 and >100 keV fluxes related to Coronal Mass Ejections (CMEs) in 2005 and 2012 which is in agreement with our findings. Second, direct observation of EEP-related SR intensity enhancements were presented at widely separated SR stations on two selected days in June 2011 (Fig. 31).

5.4.2 Estimating the Long-Term Ionospheric Height Changes Associated with EEP

In this section we estimate the long-term average ionospheric height changes associated with EEP for the H_{EW} component at the VRN station yielding the highest intensity variation on the solar cycle timescale (40–60%) (Table 7). If we accept that 25–30% of the observed SR intensity enhancement is attributable to a global change of the cavity's Q-factor (independently of whether this change is related solely to X-rays or to EEP as well) the remaining 15–30% in years with the largest enhancement can be considered to be related to the local waveguide deformation caused by EEP.

	Observed (%)	**Q-factor related (%)**	**Height change related (%)**
First SR mode	40–60	25–30	15–30
11 Hz	20–25	∼0	20–25

Table 7: Observed SR intensity variations at the VRN station in the H_{EW} field component and the predicted contributions of global Q-factor- and local ionospheric height changes.

We estimate the EEP-related height changes of the waveguide from the intensity at 11 Hz (the first minimum between the first and second resonance peaks) which can be considered to be mostly unaffected by the Q-factor of the cavity. Greifinger et al. (2005) have made predictions for changes in the SR amplitude as a function of the ionospheric height above the source and above the observer in the form of symbolic equations. According to these equations the measured magnetic intensity at a given frequency is proportional to the reciprocal value of the squared local magnetic height. It follows that the 20–25% intensity enhancements documented at 11 Hz in 2005 and 2012 (which are in a good agreement with the resonance mode-based estimation of 15–30%) correspond to an average magnetic height decrease of ∼10% at VRN.

This average decrease in the magnetic height is considerably smaller than the decrease of isopycnic surfaces during an EEP event as observed by the EISCAT radar, with enhanced ionization down to ∼70 km (e.g., Miyoshi et al., 2015). Although EEP events are very common especially near solar maximum and can result in SR intensity enhancements in order of 50–100% (as shown in Fig. 31), they are not permanent and each event is often confined to a limited longitudinal range (Bland et al., 2021; Clilverd et al., 2007). Therefore, the smaller percentage average increase of SR intensity and the inferred decrease in the magnetic height is reasonable on the interannual timescale.

5.4.3 Interpretation of SR-Based Results

As can be seen in Fig. 29 and Table 4 the solar cycle modulation of SR intensity can be different station-to-station depending on the station location and on the wave propagation path corresponding to the measured field component. A deformation in the Earth–ionosphere cavity is expected to affect SR intensity locally where the deformation occurs, whereas a change in its Q-factor is expected to affect SR intensity (I) globally, for all propagation paths that cross the affected area(s). We aim to describe these effects by two simple formulas:

$$I \sim Q^2 \,, \tag{88}$$

and

$$I \sim (1/H_m^2) \,, \tag{89}$$

where Q and H_m denote the Q-factor of the cavity and its local magnetic height, respectively. The solar cycle modulation of the H_{NS} field component at the SHI and VRN stations can be well described by the X-ray-related global variation of the cavity's Q-factor and the H_{EW} field component at the VRN station by the combined effect of the Q-factor variation and an EEP-related height decrease of ~10%.

At different SR stations the wave propagation directions corresponding to the perpendicular magnetic coils are differently affected by EEP. It seems to be generally true that the longer the propagation path crosses the precipitation-affected area(s) the larger the solar cycle modulation of SR intensity. It is usually the H_{NS} coil, sensitive to the east-west propagation direction, which yields propagation paths with greater extents beneath the precipitation belt. This is the case for the high latitude SOU, HRN, MAI and SYO stations (see Figs. 26a,e,f) where the solar cycle modulation is indeed larger in the H_{NS} component as compared to the H_{EW} component (Figs. 27 and 29). The H_{NS} coil is also more responsive at the two mid-high latitude SR stations ESK and BEL in spite the fact that the GCPs corresponding to the H_{NS} component at these two stations do not cross the northern precipitation belt according to Figs. 26b and c. This result may indicate that the precipitation belts are more extended towards lower latitudes as shown by the POES data. Towards lower latitudes the flux of precipitating 30–300 keV electrons decreases and POES is known to underestimate flux values below ~10^4–10^5 electrons/cm^2/sec/ster (van de Kamp et al., 2018, 2016).

The magnetic height of SRs is affected by electrons with energies lower than 30 keV (the lowest channel of POES satellites) and these electrons may form wider precipitation belts. At the VRN and SHI stations the SR response is more pronounced in the H_{EW} coil, sensitive to the north-south propagation direction. At SHI the H_{EW} is the one field component with a GCP crossing the precipitation belts (Fig. 26g) while at VRN the propagation path corresponding to the H_{EW} component meets not only the southern precipitation belt but the South Atlantic Magnetic Anomaly as well (Fig. 26b). Besides the dominant response of the H_{EW} component as compared to the H_{NS} component this fact may account for the observation that the H_{EW} component at the VRN station yields the highest response among all the investigated records. Another factor that should be important for this observation is that the longitudinal sector including America is shown to be affected by harder electron precipitation spectrum than the other parts of the globe which can be attributed to the tilted-offset dipole magnetic field of Earth (Clilverd et al., 2007). We note that 2012 shows the highest relative SR intensity values at the HRN and VRN stations (Fig. 29; Table 4) despite the observation that POES measurements show larger EEP fluxes in 2005 as compared to 2012 (Fig. 30). We can explain this observation by the fact that in 2012 both X-rays and EEP show enhanced values while 2005 is in the declining phase of the solar cycle characterized by a lower X-ray flux (Figs. 27a,b).

As we noted earlier in Section 5.3 EEP is known to have seasonal dependence (Bland et al., 2019; Clilverd et al., 2007; Suvorova, 2017), i.e., June/July maxima in its occurrence rate can be identified in both hemispheres. We note that rocket measurements at polar stations also showed maximum electron density in June/July at the 80 km height of the ionospheric D-region in both hemispheres (Danilov and Vanina, 1999). We suggest that this seasonal dependence may contribute to the observed modulation of the magnitude of the annual SR intensity variation (Fig. 28).

5.4.4 Interpretation of DEMETER-Based Results

DEMETER observations showed that the effective height of the Earth–ionosphere waveguide is generally the highest at mid geomagnetic latitudes, lower at low geomagnetic latitudes and the very lowest at the highest observed geomagnetic latitudes (in proximity to the precipitation belts) (Table 6) which is in a general agreement with our SR-based findings that the Earth–ionosphere cavity is deformed by solar X-rays (dominantly over lower latitudes) and by EEP (dominantly over higher latitudes) (as illustrated in Fig. 33). The deformation effect of EEP has a larger variability on the solar cycle timescale which results in a larger height reduction at higher latitudes, as shown by the effective heights. This finding is in keeping with the high latitude location of the precipitation belts. Although the documented 2.2% height decrease between 2005 and 2009 corresponding to mid-high latitudes is considerably smaller than the ∼10% value inferred for the VRN station, one needs to keep in mind that 1) DEMETER data are restricted to geomagnetic latitudes lower than 65° , 2) the South Atlantic Magnetic Anomaly (which is in close vicinity to VRN) is excluded from the dataset, 3) electromagnetic waves with higher ELF, lower VLF frequencies are responsive at different altitude regions than the magnetic height of SRs and 4) this is an integrated value for all longitudes while the longitudinal sector including America is shown to be affected by harder electron precipitation.

It is to be noted as well that the inferred effective height values were measured exclusively on the nightside by DEMETER at 22:30 LT where solar X-rays are absent. We can explain this seeming contradiction by assuming that lightning impulses may propagate in the dayside hemisphere of the EIWG before escaping the waveguide on the nightside (but close to the local sunset).

5.5 Conclusions

In the present study, long-term records of the first SR magnetic mode intensity from eight different stations were compared with the fluxes of precipitating medium energy electrons and with independently identified EEP events to confirm that the long-term solar cycle modulation of SR intensity (documented originally at high latitude stations) is caused by the EEP-related local deformation of the Earth–ionosphere cavity. Although our results generally confirmed the presence of EEP-related deformations in the Earth–ionosphere cavity, we also found that the EEP-effect alone cannot account for all our SR-based observations and that the combined effect of solar X-rays and EEP needs to be considered. We have identified four distinct factors that can play important role in shaping long-term SR intensity records: 1) X-ray related deformations of the cavity, 2) X-ray related changes in the Q-factor of the cavity, 3) EEP-related deformations of the cavity and 4) EEP-related changes in the Q-factor of the cavity. The exact interplay of these factors depends on the location of the SR station and the orientation of the magnetic coils, i.e., on the wave propagation path corresponding to the actual measurement. The deformation of the cavity is expected to affect SR intensity locally beneath the deformed area(s) whereas Q-factor variations are expected to introduce globally observable changes in SR intensity.

In connection to EEP we showed that there is a very good phase agreement between certain SR intensity records and the long-term variation of 30–300 keV EEP fluxes as provided by the POES NOAA-15 satellite which is most conspicuous in years not exactly coincident with the solar maximum, as in for example 2005 and 2012 when both the EEP flux and SR intensity showed exceptional values. We documented SR intensity and Q-factor enhancements connected to individual EEP events on the daily timescale in June 2011 by comparing the corresponding records with EEP events independently identified by Bland et al. (2019) in the measurements of the Syowa East SuperDARN radar. We showed that the effect of certain EEP events can be identified in SR intensity records from both the Southern and Northern Hemispheres (under different sunlit conditions), from different longitudinal sectors and the EEP-related relative enhancement of SR intensity can attain values as high as 50–100%. The solar cycle modulation of the magnitude of the annual SR intensity variation was demonstrated and efforts were made to quantify the ionospheric height changes associated with EEP. It has been shown that near the Antarctic station Vernadsky (yielding the largest long-term SR intensity variation) the upper (magnetic) characteristic height of the Earth–ionosphere cavity resonator decreased by ~10% in the most conspicuous years of EEP activity.

Bozoki et al. (2021) is the first paper to show that the solar cycle variation of SR intensity is consistently observable all around the globe and gives a qualitative explanation for this observation. Quantitative conclusions were made as well based on simple SR intensity-cavity height, SR intensity-Q-factor relations, which describe the identified effects reasonably well. To achieve a more detailed interpretation of our observation-based results it is necessary to apply a full model of the SRs. We hope that our work will motivate and assist such works in the future.

The effective height of the Earth–ionosphere waveguide as inferred from DEMETER measurements provided an independent view on the long-term deformation of the Earth–ionosphere cavity. We showed that the largest height of the cavity can be found at mid (geomagnetic) latitudes while the waveguide is depressed at low and high (geomagnetic) latitudes which is in a general agreement with our general conclusion that the Earth–ionosphere cavity is deformed by solar X-rays dominantly over lower latitudes and by EEP dominantly over higher latitudes. It has also been demonstrated that effective height of the waveguide varies on the solar cycle timescale at all (geomagnetic) latitudes and this effect is stronger at high (geomagnetic) latitudes where energetic electrons can precipitate into the upper boundary region of the Earth-ionosphere cavity.

We suggest that SR measurements may be suitable to collect information and thus to monitor changes in the lower ionosphere associated with EEP which would be highly valuable for investigating space weather processes and their impact on atmospheric chemistry (see e.g., Mironova et al., 2015). Such measurements could yield quasi-continuous information on EEP in a global sense in contrast to the space and time limitations of satellite and radar observations.

Finally, the value of high latitude stations for SR-based research should be emphasized. Due to their remote locations, these SR stations have usually much lower cultural noise contamination than stations at low- and mid-latitudes. And because they are also remote from thunderstorm activity they are not subjected to the interference caused by nearby lightning. These two properties make high latitude stations extremely valuable for SR-connected research aims, such as the reconstruction of global lightning activity by inversion methods. However, because of the extra-terrestrial effects on the SR cavity at higher latitude as documented in this work, it is of vital importance to consider all possible masking effects when analyzing these data-sets in connection with lightning-related climate research.

6 Summary

The focus of the present PhD dissertation is on Schumann resonances (SRs), which are the global electromagnetic (EM) resonances of the Earth-ionosphere cavity. In the lowest part (<100 Hz) of the extremely low frequency (ELF; 3 Hz - 3 kHz) band EM waves radiated by lightning can propagate with very low attenuation ($\sim$0.5 dB/Mm) in the waveguide formed by the Earth's surface and the lowest part of the ionosphere, and can travel a number of times around the globe before losing most of their energy. It is the constructive interference of these waves propagating in opposite directions (direct and antipodal waves) that creates the SRs which can be observed at $\sim$8, $\sim$14, $\sim$20, etc. Hz. The approximate number of 30–100 lightning strokes per second worldwide maintains SRs quasi-continuously. SRs are known as a powerful tool to investigate global lightning activity and large-scale changes in the state of the lower ionosphere. More generally, SRs can be considered as a research tool to study both the Earth's climate and space weather.

SRs can be measured in the vertical electric and in the horizontal magnetic field. At the Széchenyi István Geophysical Observatory (SZIGO) (also known as the Nagycenk Geophysical Observatory) near Sopron in Hungary, both the electric and magnetic field components are measured using a vertical ball antenna and a pair of induction coil magnetometers. I presented an up-to-date description of these measurements. The SR measurements in the SZIGO were used in this dissertation to study the El Nino–Southern Oscillation (ENSO) phenomenon.

The forward and inverse modeling parts of an inversion algorithm aimed to infer the intensity and global distribution of lightning activity based on SR measurements were described. In modeling SRs the transmission surface approach was followed which means that the Earth-ionosphere cavity was considered as a two-dimensional transmission line and the telegraph equations were solved. This is a valid approach as the wavelengths of the guided ELF waves are much longer than the distance between the Earth's surface and the ionosphere. First, the 2D telegraph equation (TDTE) was formulated and solved analytically for an ideal (lossless) case. Later, the analytical solution has been modified to take into consideration losses connected to the imperfect conductivity of the ionosphere and the conductance of air. These solutions were given for the uniform Earth-ionosphere cavity which was then followed by the description of an analytical and a numerical approach that can take into consideration the day-night asymmetry of the Earth-ionosphere cavity. The cause of this asymmetry is that the ionization sources (Lyman-series, UV, EUV, X-ray) on the sunlit side are missing in the nightside hemisphere and the characteristic height of the cavity increases due to the high neutralization rate. Finally, I showed how to model the incoherently superimposed EM field of multiple lightning sources.

I presented my implementation of the `schupy` open source python package and its first function `forward_tdte`, which enables the simulation of SRs generated by given lightning sources and return the theoretical electric and magnetic fields at an arbitrary geographical location. The `forward_tdte` function applies the analytical solution corresponding to the lossy, uniform cavity and can simulate point as well as extended sources. Schupy is available via the pip package manager system and the project's Github page. I presented three case studies based on the `schupy.forward_tdte` function where I investigated the convergence of the theoretical spectra, the spectra of antipodal sources as well as the spectra of an extended source. These case studies demonstrated the usefulness of `schupy` in investigating SR-related scientific questions.

I presented three numerical tests to compare the analytical and numerical solutions of the TDTE. In both approaches some inaccuracy of the algorithms can be expected and this is particularly true for the non-uniform case where the day-night asymmetry of the Earth-ionosphere cavity is taken into consideration. The results showed excellent agreement between the output of the analytical and numerical models (also in the non-uniform case). This agreement is a strong validation of both models. Since the two solutions are completely independent, the result proves the correctness not only of the formalisms but also of the implementations (the coding).

I introduced our SR inversion model aimed to determine the distribution and intensity of global lightning activity in absolute units ($\mathrm{C}^2\,\mathrm{km}^2/\mathrm{s}$) from a few SR receiving stations. This parameter could serve as an important indicator of the Earth's changing climate. In the inversion process the logarithm of the source term has been used in order to avoid negative source intensities. As a consequence the forward modeling became nonlinear, and so a linearized inversion algorithm has been introduced which is based on the singular value decomposition (SVD) of the Jacobian. The applicability of the inversion algorithm was tested via synthetic data.

I presented my results related to the ENSO phenomenon. Multi-station observations of SR intensity documented common behavior in the evolution of continental-scale lightning activity in two super El Niño events, occurring in 1997/98 and 2015/16. The vertical electric field component of SR at Nagycenk, Hungary and the two horizontal magnetic field components in Rhode Island, USA in 1997, and in 2014–2015, the two horizontal magnetic field components at Hornsund, Svalbard and Eskdalemuir, United Kingdom as well as in Boulder Creek, California and Alberta, Canada exhibited considerable increases in SR intensity from some tens of percent up to a few hundred percents in the transition months preceding the two super El Niño events. The UT time distribution of anomalies in SR intensity indicated that in 1997 the lightning activity increased mainly in Southeast Asia, the Maritime Continent and India, i.e. the Asian chimney region. On the other hand, a global response in lightning was indicated by the anomalies in SR intensity in 2014 and 2015. I found that SR intensity records also mirror some of the important differences between the onset mechanisms of the two super El Niño events. The increase in SR intensity during the transition months was concentrated over a 2-3 month period for the 1997/98 super El Niño event. However, the 2015/16 event was built up in two stages, and in line with this, two transition periods can be identified in the SR intensity data. I confirmed the SR-based results by comparing them with independent lightning observations from the Optical Transient Detector (OTD) and the World Wide Lightning Location Network (WWLLN), which also showed increased lightning activity during the transition months. The increased lightning was attributable to increased instability due to thermodynamic disequilibrium between the surface and the midtroposphere during the transition. The main conclusion of the research was that variations in SR intensity may act as a precursor for the occurrence and magnitude of these extreme climate events, and in keeping with earlier findings, as a precursor to maxima in global surface air temperature.

I analysed the changes in the properties of the Earth-ionosphere cavity on the solar cycle timescale. The aim of the study was to confirm the theory that the modulation of SR intensity on the solar cycle timescale (documented originally at high latitude stations) is caused by the local deformation (decreasing height) of the Earth-ionosphere cavity associated with precipitating electrons. To this end, I compared the long-term records of the first SR magnetic mode intensity from eight different stations with the fluxes of precipitating medium energy electrons and with independently identified energetic electron precipitation (EEP) events. Although the results generally confirmed the role of EEP, I also found that the EEP-effect alone cannot account for all the SR-based observations. I concluded that the combined effect of solar X-rays and EEP must be taken into account to interpret the observations. I identified four distinct factors that can play important role in shaping long-term SR intensity records: 1) X-ray related deformation of the cavity, 2) X-ray related changes in the Q-factor of the cavity, 3) EEP-related deformation of the cavity and 4) EEP-related changes in the Q-factor of the cavity. The deformation of the cavity is expected to affect SR intensity locally beneath the deformed area(s) whereas Q-factor variations are expected to introduce globally observable changes in SR intensity. I documented SR intensity and Q-factor enhancements connected to individual EEP events on the daily timescale and showed that the effect of certain EEP events can be identified in SR intensity records from both the Southern and Northern Hemispheres (under different sunlit conditions), from different longitudinal sectors and the EEP-related relative enhancement of SR intensity can attain values as high as 50–100%. I demonstrated the solar cycle modulation of the magnitude of the annual SR intensity variation and made efforts to quantify the ionospheric height changes associated with EEP. I showed that the largest height of the cavity can be found at mid (geomagnetic) latitudes while the waveguide is depressed at low and high (geomagnetic) latitudes which is in a general agreement with the general conclusion that the Earth–ionosphere cavity is deformed by solar X-rays dominantly over lower latitudes and by EEP dominantly over higher latitudes. I also demonstrated that the effective height of the waveguide varies on the solar cycle timescale at all (geomagnetic) latitudes and this effect is stronger at high (geomagnetic) latitudes where energetic electrons can enter the upper atmosphere along magnetic field lines. The results suggested that SR measurements can be used to monitor EEP-related changes in the lower ionosphere. On the other hand, SR intensity changes associated with space weather phenomena need to be identified and removed/corrected to get a realistic estimation for the intensity and distribution of global lightning activity.

7 Összefoglaló

Jelen doktori értekezés középpontjában a Schumann-rezonanciák (SR-ák) állnak, melyek a Föld–ionoszféra üreg globális elektromágneses (EM) rezonanciái. A villámok által kisugárzott EM hullámok az extrém alacsony frekvenciasáv (ELF sáv; 3 Hz – 3 kHz) legalsó részén (<100 Hz) nagyon kis csillapítással (∼0.5 dB/Mm) terjednek a Föld felszíne és az alsó ionoszféra által alkotott hullámvezetőben, és többször is körbekerülik a Földet, mielőtt energiájuk nagy részét elveszítenék. Ezeknek az ellentétes irányban terjedő (direkt és antipodális) hullámoknak a konstruktív interferenciája hozza létre a SR-ákat, melyek ∼8, ∼14, ∼20 stb. Hz-en figyelhetőek meg. A globális villámtevékenység, amely másodpercenként hozzávetőlegesen 30–100 villámlást jelent, folyamatosan fenntartja ezt az EM rezonanciateret. A SR-ák a globális villámtevékenység és az alsó ionoszféra állapotában bekövetkező nagyléptékű változások vizsgálatának hatékony eszközeként ismertek. Általánosabban fogalmazva, a SR-ák a Föld éghajlatának és az űridőjárásnak tanulmányozására szolgáló kutatási eszköznek tekinthetőek.

A SR-ák a vertikális elektromos és a horizontális mágneses térben mérhetőek. A Sopronhoz közeli Széchenyi István Geofizikai Obszervatóriumban (SZIGO) (más néven Nagycenki Geofizikai Obszervatórium) mind az elektromos, mind a mágneses térkomponenseket mérik, egy gömbantennával, illetve indukciós magnetométerekkel. A dolgozatban bemutattam ezeknek a méréseknek a naprakész leírását. A SZIGO-ban végzett SR méréseket az El Niño–Déli Oszcilláció (El Niño–Southern Oscillation; ENSO) jelenség tanulmányozására használtam fel az értekezésben.

Ismertettem annak az inverziós algoritmusnak az előre- és inverz-modellezési részét, amelynek célja a villámtevékenység intenzitásának és globális eloszlásának SR-mérések alapján történő meghatározása. A SR-ák modellezésénél az ún. távvezeték felület (transmission surface) megközelítést követtük, ami azt jelenti, hogy a Föld–ionoszféra üregrezonátort egy kétdimenziós távvezetéknek tekintettük, és a távíró egyenleteket oldottuk meg erre a rendszerre. Ez egy helytálló megközelítés, mivel a vezetett ELF-hullámok hullámhossza sokkal nagyobb, mint a Föld felszíne és az ionoszféra közötti távolság. Először bemutattam a kétdimenziós távíró egyenletet (TDTE) és annak analitikus megoldását egy ideális (veszteségmentes) esetre. Ezt követően ismertettem az analitikus megoldás egy olyan módosítását, amely figyelembe veszi az ionoszféra és a légkör vezetőképességéhez kapcsolódó veszteségeket. Ezek a megoldások a homogén Föld–ionoszféra üregrezonátorra vonatkoztak, melyet egy olyan analitikus és numerikus megközelítés leírása követett, amely figyelembe veszi a Föld–ionoszféra üregrezonátor nappali-éjszakai aszimmetriáját. Ennek az aszimmetriának az az oka, hogy a nappali oldalon lévő ionizációs források (Lyman-sorozat, UV, EUV, röntgen) nincsenek jelen az éjszakai félgömbön, és ezért az üreg jellemző magassága a magas rekombinációs ráta miatt megnő. Végül megmutattam, hogy hogyan lehet modellezni több villámforrás inkoherens módon szuperponálódó EM terét.

Bemutattam az általam implementált `schupy` nyílt forráskódú python csomagot és annak első függvényét a `forward_tdte`-t, amely lehetővé teszi megadott villámforrások által generált SR-ák szimulálását, és visszaadja az elméleti elektromos és mágneses tereket egy tetszőleges földrajzi helyen. A `forward_tdte` függvény a veszteséges, homogén üregrezonátort leíró analitikus megoldást tartalmazza, és képes pont-, valamint kiterjedt források szimulálására. A `schupy` elérhető a pip csomagkezelő rendszeren és a projekt Github oldalán keresztül. Bemutattam három rövid esettanulmányt a `schupy.forward_tdte` függvény segítségével, amelyekben az elméleti spektrumok konvergenciáját, antipodális források spektrumait, valamint egy kiterjedt forrás spektrumát vizsgáltam. Ezek az esettanulmányok bizonyították a `schupy` hasznosságát SR-val kapcsolatos tudományos kérdések vizsgálatában.

Elvégeztem és bemutattam három numerikus tesztet a TDTE analitikus és numerikus megoldásainak összehasonlítására. Mindkét megközelítés esetében várható némi pontatlanság, és ez különösen igaz az inhomogén esetre, amikor a Föld–ionoszféra üregrezonátor nappali-éjszakai aszimmetriáját is figyelembe vesszük. Ennek ellenére a vizsgálatok kiváló egyezést mutattak az analitikus és a numerikus modellek által szolgáltatott eredmények között (az inhomogén esetben is). Ez az egyezés egy erős validációja mindkét modellnek. Mivel a két megoldás teljesen független, az eredmény nemcsak a formalizmusok, hanem az implementációk (a kódolás) helyességét is igazolja.

Bemutattam az inverziós modellünket, amelynek célja a globális zivatartevékenység eloszlásának és intenzitásának meghatározása néhány SR-vevőállomás alapján egy abszolút fizikai mennyiség segítségével ($\mathrm{C}^2\,\mathrm{km}^2/\mathrm{s}$). Ez a paraméter a Föld változó éghajlatának fontos indikátoraként szolgálhat. Az inverziós folyamat során a forrás erősségének logaritmusát használtuk a negatív forrásintenzitások elkerülése érdekében. Ennek következtében az előremodellezés egy nemlineáris problémává vált, amit a Jakobi-mátrix szinguláris értékfelbontásán alapuló linearizált inverziós eljárással oldottunk meg. Az inverziós algoritmus alkalmazhatóságát szintetikus adatok segítségével teszteltem.

Bemutattam az ENSO-jelenséghez kapcsolódó kutatási eredményeimet. A SR-intenzitás több állomáson történő megfigyelése hasonló viselkedést mutat a kontinentális léptékű villámtevékenység alakulásában az 1997/98-as és a 2015/16-os szuper El Niño események során. A két szuper El Niño eseményt megelőző átmeneti hónapokban a SR-intenzitás jelentős (néhány tíztől néhány száz százalékig terjedő) megnövekedést mutatott 1997-ben Nagycenken az elektromos-, és Rhode Island-en (USA) a mágneses térkomponensben, csakúgy, mint 2014–2015-ben Hornsundon (Svalbard), Eskdalemuirban (Egyesült Királyság), Boulder Creekben (Kalifornia, USA) és Albertában (Kanada) a mágneses térkomponensben. A SR-intenzitás anomáliáinak világidőben mutatkozó eloszlása alapján kimutattam, hogy 1997-ben a villámtevékenység főként Délkelet-Ázsiában és Indiában, azaz az ázsiai zivatarrégióban nőtt meg. Ugyanakkor a villámtevékenység globális változását jelezték 2014-ben és 2015-ben a SR-intenzitás anomáliái. Megállapítottam, hogy a SR-intenzitás adatok tükrözik a két szuper El Niño esemény kialakulása közötti fontos különbségeket is. Az átmeneti időszakra jellemző SR-intenzitás növekedés egy 2-3 hónapos időszakra koncentrálódik az 1997/98-as szuper El Niño eseménynél. Ugyanakkor a 2015/16-os esemény két részletben épült fel, és ezzel összhangban két átmeneti időszak azonosítható a SR-intenzitás adatokban. A SR-alapú eredményeket megerősítettem az Optical Transient Detector (OTD) és a World Wide Lightning Location Network (WWLLN) független villámmegfigyeléseivel való összehasonlítással, amelyek szintén fokozott villámtevékenységet mutattak az átmeneti hónapokban. Az átmeneti időszak során megnövekedett villámlás a felszín és a középtroposzféra közötti termodinamikai egyensúly hiánya miatt megnövekedett instabilitásnak tulajdonítható. A kutatás fő következtetése az volt, hogy a SR intenzitásának változása előrejelzője lehet e szélsőséges éghajlati események előfordulásának és nagyságának, és a korábbi eredményekkel összhangban a globális felszíni levegőhőmérséklet maximumait is előrejelezheti.

Elemeztem a Föld–ionoszféra üregrezonátor tulajdonságaiban napciklus-időskálán bekövetkező változásokat. A kutatás célja annak az elméletnek a megerősítése volt, hogy a SR intenzitásának napciklus-időskálán történő modulációját (melyet eredetileg csak magas szélességű állomásokon mutattak ki), a Föld–ionoszféra üregrezonátor kiszóródó elektronokhoz kapcsolódó helyi deformációja (csökkenő magassága) okozza. Ennek érdekében az első mágneses SR-módus intenzitásának nyolc távoli állomáson mért hosszútávú idősorait kiszóródó, közepes energiájú elektronok fluxusával és független mérésekben azonosított energetikus elektronkiszóródási (EEK) eseményekkel hasonlítottam össze. Bár az eredmények megerősítették az EEK-hoz kapcsolódó deformáció szerepét, ugyanakkor az EEK önmagában nem magyarázta az összes SR-alapú megfigyelést. Arra a következtetésre jutottam, hogy a Nap röntgensugárzásának és az EEK-nak az együttes hatását kell figyelembe venni a megfigyelések értelmezéséhez. Négy különböző tényezőt azonosítottam, amelyek fontos szerepet játszanak a hosszútávú SR-intenzitás idősorok alakításában: 1) az üreg röntgensugárzással összefüggő deformációja, 2) az üreg jósági tényezőjének röntgensugárzással összefüggő változása, 3) az üreg EEK-al összefüggő deformációja és 4) az üreg jósági tényezőjének EEK-al összefüggő változása. Az üreg helyi deformációja (magasságváltozása) várhatóan lokálisan befolyásolja a SR-intenzitást a deformált terület(ek) alatt, míg a jósági tényező változása várhatóan globálisan megfigyelhető változásokat okoz a SR-intenzitásban. Dokumentáltam egyedi EEK-eseményekhez kapcsolódó SR-intenzitás és jósági tényező növekedéseket napi időskálán, és kimutattam, hogy bizonyos EEP-események hatása jól azonosítható mind a déli-, mind az északi félteken (éjszakai és nappali oldalon), különböző hosszúsági szektorokból származó SR-intenzitás adatokban, és a SR-intenzitás EEK-hoz kapcsolódó relatív növekedése elérheti az 50-100%-ot is. Bemutattam az éves SR-intenzitásváltozás nagyságának napciklus-időskálán jelentkező modulációját, és erőfeszítéseket tettem az EEK-hoz kapcsolódó ionoszférikus magasságváltozások számszerűsítésére. A Föld–ionoszféra hullámvezető effektív magasságának a DEMETER műhold méréseiből származtatott értékei független képet nyújtottak a Föld–ionoszféra üreg hosszútávú deformációjáról. Megmutattam, hogy az üreg legnagyobb magassága közepes (geomágneses) szélességen található, míg a hullámvezető alacsony és magas (geomágneses) szélességen alacsonyabb, ami egybevág azzal az általános következtetésemmel, hogy a Föld–ionoszféra üreget alacsonyabb szélességen a Nap röntgensugárzása, míg magasabb szélességen az EEK deformálja. Azt is kimutattam, hogy a hullámvezető effektív magassága napciklus-időskálán minden (geomágneses) szélességen változik, és ez a hatás erősebb magas (geomágneses) szélességen, ahol a kiszóródó elektronok a mágneses erővonalak mentén belépnek a felsőlégkörbe. Az eredmények alapján a SR-mérések alkalmasak lehetnek EEK-hoz kapcsolódó változások nyomonkövetésére az alsó ionoszférában.

Acknowledgement

(in Hungarian)

Nagyon sokan vannak azok, akiknek sokat köszönhetek, akik jelentősen hozzájárultak ahhoz, hogy elkészüljön ez a doktori értekezés. Első körben három embert szeretnék kiemelni: témavezetőmet, Dr. Sátori Gabriellát, édesapámat, Dr. Bozóki Zoltánt és feleségemet, Bozóki-Kecskés Boglárkát. Ők hárman mindvégig nyomon követték a dolgaim alakulását, mellettem álltak, meghallgattak, támogattak, segítettek, és meghatározó módon hozzájárultak ahhoz, hogy az elmúlt négy év ilyen fantasztikusan szép, élvezetes és produktív legyen. Rengeteget tanultam témavezetőmtől, aki nyugdíjas korba lépve is hihetetlen lelkesedéssel, érdeklődéssel és alázattal áll a világ működésének megértéséhez. Lenyűgöző számomra, hogy mennyi mindent elárul számára egy-egy mérési adatsor. Nagyon jó szívvel gondolok vissza azokra az időszakokra, amikor egy-egy kérdés olyannyira izgatott minket, hogy függetlenül attól, hogy éppen hétvége vagy szünet volt, folyamatos levelezésbe álltunk, és igyekeztünk megfejteni az éppen aktuális ”feladványt”. Nagyon simán összejött néhány 10 e-mail egyetlen nap alatt... Hálás vagyok a gondviselésnek, hogy én is fizikus lettem, csakúgy, mint édesapám. A kutatói életforma gyerekkorom óta kézzelfogható közelségben van számomra, és hogy ez micsoda előnyt jelent, csak mostanában értem meg úgy igazán. Azt gondolom, hogy mindkettőnknek rengeteget jelent, hogy van kivel megbeszélni az éppen aktuális szakmai történéseket. Nagyon köszönöm feleségemnek, hogy elviseli a kutatói élettel járó nehézségeket, és segített nekem abban, hogy egy élhető munkaritmust tudjak mostanra kialakítani. Köszönöm neki, hogy érdeklődéssel meghallgat minden apró-cseprő fejleményt a szakmámmal kapcsolatban, és hogy mindig számíthatok rá, ha valamilyen nehézségben tanácsra van szükségem. Köszönöm fizikus (Dálya Gergely, Kapás Kornél, Takátsy János) és geofizikus (Bozsó István, Buzás Attila) barátaimnak a sok jó közös élményt, szép emléket, beszélgetést az elmúlt négy évből. Nagyon szerencsésnek érzem magam azért, hogy egy csónakban evezhettünk. Köszönöm Wesztergom Viktornak, hogy odacsábított a soproni intézethez és igazgatóként folyamatosan egyengette utamat, valamint Dr. Bór Józsefnek és Dr. Steinbach Péternek, hogy sokat formálták a gondolkodásomat, és hogy bármikor fordulhattam hozzájuk segítségért.

(in English)

I am very grateful to all the colleagues I worked with during my doctoral studies. I would especially like to thank Dr. Earle Williams, who gave me a lot of guidance and help. Many thanks also to Ciaran Beggan for proofreading this thesis.

References

Ádám, A. and Bencze, P. (1963). Study of natural energy sources in the low frequency band (in Hungarian). *Magyar Geofizika*, 4:29–35.

Ahmad, A. and Ghosh, M. (2017). Variability of lightning activity over India on ENSO time scales. *Advances in Space Research*, 60(11):2379–2388.

Aich, V., Holzworth, R., Goodman, S. J., Kuleshov, Y., Price, C., and Williams, E. (2018). Lightning: A new essential climate variable. *EOS*, 99.

Albrecht, R. I., Goodman, S. J., Buechler, D. E., Blakeslee, R. J., and Christian, H. J. (2016). Where Are the Lightning Hotspots on Earth? *Bulletin of the American Meteorological Society*, 97(11):2051 – 2068.

Allen, R., Lindesay, J., and Parker, D. (1996). *El Nino Southern Oscillation and Climatic Variability.* CSIRO Publishing, Clayton, Australia.

Ando, Y. and Hayakawa, M. (2007). Use of generalized cross validation for identification of global lightning distribution by using Schumann resonances. *Radio Science*, 42(2).

Ando, Y., Hayakawa, M., Shvets, A. V., and Nickolaenko, A. P. (2005). Finite difference analyses of Schumann resonance and reconstruction of lightning distribution. *Radio Science*, 40(2).

Artamonov, A., Mironova, I., Kovaltsov, G., Mishev, A., Plotnikov, E., and Konstantinova, N. (2017). Calculation of atmospheric ionization induced by electrons with non-vertical precipitation: Updated model CRAC-EPII. *Advances in Space Research*, 59(9):2295–2300.

Asikainen, T. and Ruopsa, M. (2016). Solar wind drivers of energetic electron precipitation. *Journal of Geophysical Research: Space Physics*, 121(3):2209–2225.

Baker, D., Erickson, P., Fennell, J., Foster, J., Jaynes, A., and Verronen, P. (2018). Space Weather Effects in the Earth's Radiation Belts. *Space Science Reviews*, 214.

Balser, M. and Wagner, C. (1960). Observations of Earth–Ionosphere Cavity Resonances. *Nature*, pages 638–641.

Barr, R., Jones, D., and Rodger, C. (2000). ELF and VLF radio waves. *Journal of Atmospheric and Solar-Terrestrial Physics*, 62(17):1689–1718.

Beggan, C. D. and Musur, M. (2018). Observation of Ionospheric Alfvén Resonances at 1–30 Hz and Their Superposition With the Schumann Resonances. *Journal of Geophysical Research: Space Physics*, 123(5):4202–4214.

Beggan, C. D. and Musur, M. A. (2019). Is the Madden–Julian Oscillation reliably detectable in Schumann Resonances? *Journal of Atmospheric and Solar-Terrestrial Physics*, 190:108–116.

Beirle, S., Koshak, W., Blakeslee, R., and Wagner, T. (2014). Global patterns of lightning properties derived by OTD and LIS. *Natural Hazards and Earth System Sciences*, 14(10):2715–2726.

Belova, E., Kirkwood, S., Ekeberg, J., Osepian, A., Häggström, I., Nilsson, H., and Rietveld, M. (2005). The dynamical background of polar mesosphere winter echoes from simultaneous EISCAT and ESRAD observations. *Annales Geophysicae*, 23(4):1239–1247.

Berthelier, J., Godefroy, M., Leblanc, F., Malingre, M., Menvielle, M., Lagoutte, D., Brochot, J., Colin, F., Elie, F., Legendre, C., Zamora, P., Benoist, D., Chapuis, Y., Artru, J., and Pfaff, R. (2006). ICE, the electric field experiment on DEMETER. *Planetary and Space Science*, 54(5):456–471. First Results of the DEMETER Micro-Satellite.

Blakeslee, R. J., Mach, D. M., Bateman, M. G., and Bailey, J. C. (2014). Seasonal variations in the lightning diurnal cycle and implications for the global electric circuit. *Atmospheric Research*, 135-136:228–243.

Bland, E., Tesema, F., and Partamies, N. (2021). D-region impact area of energetic electron precipitation during pulsating aurora. *Annales Geophysicae*, 39(1):135–149.

Bland, E. C., Heino, E., Kosch, M. J., and Partamies, N. (2018). SuperDARN Radar-Derived HF Radio Attenuation During the September 2017 Solar Proton Events. *Space Weather*, 16(10):1455–1469.

Bland, E. C., Partamies, N., Heino, E., Yukimatu, A. S., and Miyaoka, H. (2019). Energetic Electron Precipitation Occurrence Rates Determined Using the Syowa East SuperDARN Radar. *Journal of Geophysical Research: Space Physics*, 124(7):6253–6265.

Boccippio, D. J., Koshak, W., Blakeslee, R., Driscoll, K., Mach, D., Buechler, D., Boeck, W., Christian, H. J., and Goodman, S. J. (2000). The Optical Transient Detector (OTD): Instrument Characteristics and Cross-Sensor Validation. *Journal of Atmospheric and Oceanic Technology*, 17(4):441 – 458.

Boccippio, D. J., Williams, E. R., Heckman, S. J., Lyons, W. A., Baker, I. T., and Boldi, R. (1995). Sprites, ELF Transients, and Positive Ground Strokes. *Science*, 269(5227):1088–1091.

Boldi, R., Williams, E., and Guha, A. (2018). Determination of the Global-Average Charge Moment of a Lightning Flash Using Schumann Resonances and the LIS/OTD Lightning Data. *Journal of Geophysical Research: Atmospheres*, 123(1):108–123.

Bor, J., Satori, G., Barta, V., Szabone-Andre, K., Szendroi, J., Wesztergom, V., Bozoki, T., Buzas, A., and Koronczay, D. (2020). Measurements of atmospheric electricity in the Széchenyi István Geophysical Observatory, Hungary. *History of Geo- and Space Sciences*, 11(1):53–70.

Bozoki, T., Pracser, E., Satori, G., Dalya, G., Kapas, K., and Takatsy, J. (2019). Modeling Schumann resonances with schupy. *Journal of Atmospheric and Solar-Terrestrial Physics*, 196:105144.

Bozoki, T., Satori, G., Williams, E., Mironova, I., Steinbach, P., Bland, E. C., Koloskov, A., Yampolski, Y. M., Budanov, O. V., Neska, M., Sinha, A. K., Rawat, R., Sato, M., Beggan, C. D., Toledo-Redondo, S., Liu, Y., and Boldi, R. (2021). Solar Cycle-Modulated Deformation of the Earth–Ionosphere Cavity. *Frontiers in Earth Science*, 9.

Bronshtein, I. N. and Semendyayev, K. A. (1997). *Handbook of Mathematics (3rd Ed.)*. Springer-Verlag, Berlin, Germany.

Bürgesser, R. E. (2017). Assessment of the World Wide Lightning Location Network (WWLLN) detection efficiency by comparison to the Lightning Imaging Sensor (LIS). *Quarterly Journal of the Royal Meteorological Society*, 143(708):2809–2817.

Cecil, D. J., Buechler, D. E., and Blakeslee, R. J. (2014). Gridded lightning climatology from TRMM-LIS and OTD: Dataset description. *Atmospheric Research*, 135-136:404–414.

Chapman, F. W., Jones, D. L., Todd, J. D. W., and Challinor, R. A. (1966). Observations on the Propagation Constant of the Earth-Ionosphere Waveguide in the Frequency Band 8 c/s to 16 kc/s. *Radio Science*, 1(11):1273–1282.

Chaudhari, H. S., Ranalkar, M. R., Kumkar, Y. V., Oh, J. H., and Singh, G. P. (2010). *Study of Lightning Activity over Indian Subcontinent*, pages 121–131. World Scientific Publishing Company.

Chen, L., Li, T., Wang, B., and Wang, L. (2017). Formation Mechanism for 2015/16 Super El Niño. *Sci Rep*, 7.

Chisham, G., Lester, M., Milan, S. E., Freeman, M. P., Bristow, W. A., and Grocott, A., e. a. (2007). A Decade of the Super Dual Auroral Radar Network (SuperDARN): Scientific Achievements, New Techniques and Future Directions. *Surv. Geophys.*, 28:33–109.

Christian, H. J., Blakeslee, R. J., Boccippio, D. J., Boeck, W. L., Buechler, D. E., Driscoll, K. T., Goodman, S. J., Hall, J. M., Koshak, W. J., Mach, D. M., and Stewart, M. F. (2003). Global frequency and distribution of lightning as observed from space by the Optical Transient Detector. *Journal of Geophysical Research: Atmospheres*, 108(D1):ACL 4–1–ACL 4–15.

Christofilakis, V., Tatsis, G., Votis, C., Contopoulos, I., Repapis, C., and Tritakis, V. (2019). Significant ELF perturbations in the Schumann Resonance band before and during a shallow mid-magnitude seismic activity in the Greek area (Kalpaki). *Journal of Atmospheric and Solar-Terrestrial Physics*, 182:138–146.

Chronis, T. G., Goodman, S. J., Cecil, D., Buechler, D., Robertson, F. J., Pittman, J., and Blakeslee, R. J. (2008). Global lightning activity from the ENSO perspective. *Geophysical Research Letters*, 35(19).

Clilverd, M. A., Meredith, N. P., Horne, R. B., Glauert, S. A., Anderson, R. R., Thomson, N. R., Menk, F. W., and Sandel, B. R. (2007). Longitudinal and seasonal variations in plasmaspheric electron density: Implications for electron precipitation. *Journal of Geophysical Research: Space Physics*, 112(A11).

Coughlin, M. W., Christensen, N. L., Rosa, R. D., Fiori, I., Gołkowski, M., Guidry, M., Harms, J., Kubisz, J., Kulak, A., Mlynarczyk, J., Paoletti, F., and Thrane, E. (2016). Subtraction of correlated noise in global networks of gravitational-wave interferometers. *Classical and Quantum Gravity*, 33(22):224003.

Coughlin, M. W., Cirone, A., Meyers, P., Atsuta, S., Boschi, V., Chincarini, A., Christensen, N. L., De Rosa, R., Effler, A., Fiori, I., Gołkowski, M., Guidry, M., Harms, J., Hayama, K., Kataoka, Y., Kubisz, J., Kulak, A., Laxen, M., Matas, A., Mlynarczyk, J., Ogawa, T., Paoletti, F., Salvador, J., Schofield, R., Somiya, K., and Thrane, E. (2018). Measurement and subtraction of Schumann resonances at gravitational-wave interferometers. *Phys. Rev. D*, 97:102007.

Cummer, S. (2000). Modeling electromagnetic propagation in the Earth-ionosphere waveguide. *IEEE Transactions on Antennas and Propagation*, 48(9):1420–1429.

Danilov, A. and Vanina, L. (1999). Comparison of the polar D-region behavior in the Arctic and Antarctic. *Advances in Space Research*, 24(12):1655–1664. The Antarctic and Arctic Middle Atmospheres: Their Differences and Similarities.

Davis, T. N. and Sugiura, M. (1966). Auroral electrojet activity index AE and its universal time variations. *Journal of Geophysical Research (1896-1977)*, 71(3):785–801.

Dong, L. and McPhaden, M. (2018). Unusually warm Indian Ocean sea surface temperatures help to arrest development of El Niño in 2014. *Sci Rep*.

Dowdy, A. (2016). Seasonal forecasting of lightning and thunderstorm activity in tropical and temperate regions of the world. *Sci Rep*, 6.

Dyrda, M., Kulak, A., Mlynarczyk, J., and Ostrowski, M. (2015). Novel analysis of a sudden ionospheric disturbance using Schumann resonance measurements. *Journal of Geophysical Research: Space Physics*, 120(3):2255–2262.

Dyrda, M., Kulak, A., Mlynarczyk, J., Ostrowski, M., Kubisz, J., Michalec, A., and Nieckarz, Z. (2014). Application of the Schumann resonance spectral decomposition in characterizing the main African thunderstorm center. *Journal of Geophysical Research: Atmospheres*, 119(23):13,338–13,349.

Elhalel, G., Price, C., D., F., and A., S. (2019). Cardioprotection from stress conditions by weak magnetic fields in the Schumann Resonance band. *Sci Rep.*

Erdelyi, A. (1953). *Higher Transcendential Functions.* McGraw-Hill, New York, USA.

Ferencz, O. E., Ferencz, C., Steinbach, P., Lichtenberger, J., Hamar, D., Parrot, M., Lefeuvre, F., and Berthelier, J.-J. (2007). The effect of subionospheric propagation on whistlers recorded by the DEMETER satellite - observation and modelling. *Annales Geophysicae*, 25(5):1103–1112.

Feynman, R. P., Leighton, R. B., and Sands, M. (2010). *The Feynman lectures on physics; New millennium ed.* Basic Books, New York, USA.

Fornieles-Callejón, J., Salinas, A., Toledo-Redondo, S., Portí, J., Méndez, A., Navarro, E. A., Morente-Molinera, J. A., Soto-Aranaz, C., and Ortega-Cayuela, J. S. (2015). Extremely low frequency band station for natural electromagnetic noise measurement. *Radio Science*, 50(3):191–201.

Fraser-Smith, A. C., Ogawa, T., McGill, P. R., Bernardi, A., Ladd, M. E., and Helliwell, R. A. (1991). *Measurements of ELF/VLF Radio Noise in Japan*, pages 201–207. Springer Japan, Tokyo.

Fröhlich, C. and Lean, J. (1998). The Sun's total irradiance: Cycles, trends and related climate change uncertainties since 1976. *Geophysical Research Letters*, 25(23):4377–4380.

Füllekrug, M., Fraser-Smith, A. C., and Schlegel, K. (2002). Global ionospheric D-layer height monitoring. *Europhysics Letters (EPL)*, 59(4):626–632.

Galejs, J. (1972). *Terrestrial propagation of long electromagnetic waves.* Pergamon Press, New York, USA.

Galuk, Y., Nickolaenko, A., and Hayakawa, M. (2018). Amplitude variations of ELF radio waves in the Earth-Ionosphere cavity with the day-night nonuniformity. *Journal of Atmospheric and Solar Terrestrial Physics*, 169:23–36.

Galuk, Y. P., Kudintseva, I. G., Nickolaenko, A. P., and Hayakawa, M. (2019). Scattering of ELF radio waves by a localized non-uniformity in the lower ionosphere. *Journal of Atmospheric and Solar-Terrestrial Physics*, 194:105093.

Goodman, S. J., Blakeslee, R. J., Koshak, W. J., Mach, D., Bailey, J., Buechler, D., Carey, L., Schultz, C., Bateman, M., McCaul, E., and Stano, G. (2013). The GOES-R Geostationary Lightning Mapper (GLM). *Atmospheric Research*, 125-126:34–49.

Goodman, S. J., Buechler, D. E., Knupp, K., Driscoll, K., and McCaul Jr., E. W. (2000). The 1997–98 El Nino event and related wintertime lightning variations in the southeastern United States. *Geophysical Research Letters*, 27(4):541–544.

Greenwald, R., Baker, K., Dudeney, J., Pinnock, M., Jones, T., and Thomas, E. e. a. (1995). A global view of the dynamics of high-latitude convection. *Space Sci Rev*, 71:761–796.

Greifinger, C. and Greifinger, P. (1978). Approximate method for determining ELF eigenvalues in the earth-ionosphere waveguide. *Radio Science*, 13(5):831–837.

Greifinger, P., Mushtak, V., and Williams, E. (2005). The Lower Characteristic ELF Altitude of the Earth–Ionosphere Waveguide: Schumann Resonance Observations and Aeronomical Estimates. In *IEEE 6th International Symposium on Electromagnetic Compatibility and Electromagnetic Ecology*, pages 250–254, St. Petersburg, Russia. IEEE.

Guha, A., Banik, T., Roy, R., and De, B. K. (2017). The effect of El Nino and La Nina on lightning activity: its relation with meteorological and cloud microphysical parameters. *Nat Hazards*, 85:403–424.

Halpert, M. S. and Ropelewski, C. F. (1992). Surface Temperature Patterns Associated with the Southern Oscillation. *Journal of Climate*, 5(6):577 – 593.

Hamid, E. Y., Kawasaki, Z.-I., and Mardiana, R. (2001). Impact of the 1997–98 El Niño Event on lightning activity over Indonesia. *Geophysical Research Letters*, 28(1):147–150.

Hansen, J. and Lebedeff, S. (1987). Global trends of measured surface air temperature. *Journal of Geophysical Research: Atmospheres*, 92(D11):13345–13372.

Hayakawa, M., Nickolaenko, A. P., Galuk, Y. P., and Kudintseva, I. G. (2020). Scattering of Extremely Low Frequency Electromagnetic Waves by a Localized

Seismogenic Ionospheric Perturbation: Observation and Interpretation. *Radio Science*, 55(12):e2020RS007130.

Heckman, S. J., Williams, E., and Boldi, B. (1998). Total global lightning inferred from Schumann resonance measurements. *Journal of Geophysical Research: Atmospheres*, 103(D24):31775–31779.

Hutchins, M. L., Holzworth, R. H., Brundell, J. B., and Rodger, C. J. (2012). Relative detection efficiency of the World Wide Lightning Location Network. *Radio Science*, 47(6).

Jackson, D. D. (1972). Interpretation of Inaccurate, Insufficient and Inconsistent Data. *Geophysical Journal International*, 28(2):97–109.

Kandalgaonkar, S. S., Tinmaker, M. I. R., Kulkarni, J. R., and Nath, A. (2003). Diurnal variation of lightning activity over the Indian region. *Geophysical Research Letters*, 30(20).

Kandalgaonkar, S. S., Tinmaker, M. I. R., Kulkarni, J. R., Nath, A., Kulkarni, M. K., and Trimbake, H. K. (2005). Spatio-temporal variability of lightning activity over the Indian region. *Journal of Geophysical Research: Atmospheres*, 110(D11).

Kirillov, V. V. and Kopeykin, V. N. (2002). Solving a Two-Dimensional Telegraph Equation with Anisotropic Parameters. *Radiophysics and Quantum Electronics*, 45(12):929–941.

Kirilov, V., Kopeikin, V., and Mushtak, V. (1997). ELF Electromagnetic Waves in the Earth-Ionosphere Waveguide Channel. *Geomagnetism and Aeronomy*, 37(3):341–345.

Koloskov, A., Nickolaenko, A., Yampolsky, Y. M., Hall, C., and Budanov, O. (2020). Variations of global thunderstorm activity derived from the long-term Schumann resonance monitoring in the Antarctic and in the Arctic. *Journal of Atmospheric and Solar-Terrestrial Physics*, 201:105231.

Kowalska-Leszczynska, I., Bizouard, M.-A., Bulik, T., Christensen, N., Coughlin, M., Gołkowski, M., Kubisz, J., Kulak, A., Mlynarczyk, J., Robinet, F., and Rohde, M. (2017). Globally coherent short duration magnetic field transients and their effect on ground based gravitational-wave detectors. *Classical and Quantum Gravity*, 34(7):074002.

Kudintseva, I. G., Galuk, Y. P., Nickolaenko, A. P., and Hayakawa, M. (2018). Modifications of Middle Atmosphere Conductivity During Sudden Ionospheric Disturbances Deduced From Changes of Schumann Resonance Peak Frequencies. *Radio Science*, 53(5):670–682.

Kulak, A. and Mlynarczyk, J. (2013). ELF Propagation Parameters for the Ground-Ionosphere Waveguide With Finite Ground Conductivity. *IEEE Transactions on Antennas and Propagation*, 61(4):2269–2275.

Kulak, A., Mlynarczyk, J., Zieba, S., Micek, S., and Nieckarz, Z. (2006). Studies of ELF propagation in the spherical shell cavity using a field decomposition method based on asymmetry of Schumann resonance curves. *Journal of Geophysical Research: Space Physics*, 111(A10).

Kulak, A., Zieba, S., Micek, S., and Nieckarz, Z. (2003). Solar variations in extremely low frequency propagation parameters: 1. A two-dimensional telegraph equation (TDTE) model of ELF propagation and fundamental parameters of Schumann resonances. *Journal of Geophysical Research: Space Physics*, 108(A7).

Kulkarni, M. and Siingh, D. (2014). The relation between lightning and cosmic rays during ENSO with and without IOD — A statistical study. *Atmospheric Research*, 143:129–141.

Kumar, P. R. and Kamra, A. (2012). Variability of lightning activity in South/-Southeast Asia during 1997–98 and 2002–03 El Nino/La Nina events. *Atmospheric Research*, 118:84–102.

Lam, M. M., Horne, R. B., Meredith, N. P., Glauert, S. A., Moffat-Griffin, T., and Green, J. C. (2010). Origin of energetic electron precipitation ¿30 keV into the atmosphere. *Journal of Geophysical Research: Space Physics*, 115(A4).

Lanczos, C. (1960). *Linear Differential Operators.* Dover Publications Inc, Mineola, New York, USA.

Lanczos, C. (1964). A Precision Approximation of the Gamma Function. *Journal of the Society for Industrial and Applied Mathematics: Series B, Numerical Analysis*, 1:86–96.

Lim, Y.-K., Kovach, R. M., Pawson, S., and Vernieres, G. (2017). The 2015/16 El Niño Event in Context of the MERRA-2 Reanalysis: A Comparison of the Tropical Pacific with 1982/83 and 1997/98. *Journal of Climate*, 30(13):4819 – 4842.

Lockwood, M., Owens, M. J., Barnard, L. A., Haines, C., Scott, C. J., McWilliams, K. A., and Coxon, J. C. (2020). Semi-annual, annual and Universal Time variations in the magnetosphere and in geomagnetic activity: 1. Geomagnetic data. *J. Space Weather Space Clim.*, 10:23.

Madden, T. and Thompson, W. (1965). Low-frequency electromagnetic oscillations of the Earth-ionosphere cavity. *Reviews of Geophysics*, 3(2):211–254.

Manu, S., Rawat, R., Sinha, A. K., Gurubaran, S., and Jeeva, K. (2015). Schumann Resonances Observed at Maitri, Antarctica: Diurnal Variation and its Interpretation in Terms of Global Thunderstorm Activity. *Curr. Sci.*, 109:784–790.

Märcz, F., Sátori, G., and Zieger, B. (1997). Variations in Schumann resonances and their relation to atmospheric electric parameters at Nagycenk station. *Annales Geophysicae*, 15(12):1604–1614.

Melnikov, A., Price, C., Satori, G., and Füllekrug, M. (2004). Influence of solar terminator passages on Schumann resonance parameters. *Journal of Atmospheric and Solar-Terrestrial Physics*, 66(13):1187–1194. SPECIAL - Space Processes and Electrical Changes in Atmospheric L ayers.

Mironova, I., Aplin, K., Arnold, F., Bazilevskaya, G., Harrison, R., and Krivolutsky, A. e. a. (2015). Energetic Particle Influence on the Earth's Atmosphere. *Space Sci Rev*, 194:1–94.

Mironova, I., Bazilevskaya, G., Kovaltsov, G., Artamonov, A., Rozanov, E., Mishev, A., Makhmutov, V., Karagodin, A., and Golubenko, K. (2019a). Spectra of high energy electron precipitation and atmospheric ionization rates retrieval from balloon measurements. *Science of The Total Environment*, 693:133242.

Mironova, I. A., Artamonov, A. A., Bazilevskaya, G. A., Rozanov, E. V., Kovaltsov, G. A., Makhmutov, V. S., Mishev, A. L., and Karagodin, A. V. (2019b). Ionization of the Polar Atmosphere by Energetic Electron Precipitation Retrieved From Balloon Measurements. *Geophysical Research Letters*, 46(2):990–996.

Miyoshi, Y., Oyama, S., Saito, S., Kurita, S., Fujiwara, H., Kataoka, R., Ebihara, Y., Kletzing, C., Reeves, G., Santolik, O., Clilverd, M., Rodger, C. J., Turunen, E., and Tsuchiya, F. (2015). Energetic electron precipitation associated with pulsating aurora: EISCAT and Van Allen Probe observations. *Journal of Geophysical Research: Space Physics*, 120(4):2754–2766.

Mushtak, V. C. and Williams, E. R. (2002). ELF propagation parameters for uniform models of the Earth–ionosphere waveguide. *Journal of Atmospheric and Solar-Terrestrial Physics*, 64(18):1989–2001.

Musur, M. A. and Beggan, C. D. (2019). Seasonal and Solar Cycle Variation of Schumann Resonance Intensity and Frequency at Eskdalemuir Observatory, UK. *Sun and Geosphere*, 14(1).

Märcz, F. and Satori, G. (2005). Long-term changes in atmospheric electricity and the multivariate ENSO index. *Acta Geodaetica et Geophysica Hungarica*, 40(3-4):379–390.

Nelson, P. (1967). *Ionospheric perturbations and Schumann resonance data (PhD dissertation).* PhD thesis, Massachusetts Institute of Technology.

Neska, M., Czubak, P., , and Reda, J. (2019). Schumann Resonance Monitoring in Hornsund (Spitsbergen) and Suwałki (Poland). *Publs. Inst. Geophys. P.A.S.*, page 41–45.

Neska, M., Satori, G., Szendroi, J., Marianiuk, J., Nowozynski, K., and Tomczyk, S. (2007). Schumann Resonance Observation in Polish Polar Station at Spitsbergen and Central Geophysical Observatory in Belsk. *Publs. Inst. Geophys. Pol. Acad. Sc.*, page 398.

Nickolaenko, A. and Hayakawa, M. (2014). *Schumann Resonance for Tyros.* Springer, Japan.

Nickolaenko, A., Hayakawa, M., and Hobara, Y. (1996). Temporal variations of the global lightning activity deduced from the Schumann resonance data. *Journal of Atmospheric and Terrestrial Physics*, 58(15):1699–1709.

Nickolaenko, A. and Rabinowicz, L. (1974). Speeding up the convergence of the zonal harmonic series representation in the Schumann resonance problem. *Journal of Atmospheric and Terrestrial Physics*, 36(6):979 – 987.

Nickolaenko, A. P. and Hayakawa, M. (2002). *Resonances in the Earth-Ionosphere Cavity.* Kluwer, Dordrecht, The Netherlands.

Nickolaenko, A. P., Koloskov, A. V., Hayakawa, M., Yampolski, Y. M., Budanov, O. V., and Korepanov, V. E. (2015). 11-Year Solar Cycle in Schumann Resonance Data as Observed in Antarctica. *Sun and Geosphere*, 10:39–50.

Nickolaenko, A. P., Kudintseva, I. G., Pechony, O., Hayakawa, M., Hobara, Y., and Tanaka, Y. T. (2012). The effect of a gamma ray flare on Schumann resonances. *Annales Geophysicae*, 30(9):1321–1329.

Ogawa, T., Tanaka, Y., Yasuhara, M., Fraser-Smith, A., and Gendrin, R. (1967). Worldwide Simultaneity of Occurrence of a Q-type ELF Burst in the Schumann Resonance Frequency Range. *Journal of geomagnetism and geoelectricity*, 19(4):377–384.

Ondrásková, A., Kostecký, P., Ševčík, S., and Rosenberg, L. (2007). Long-term observations of Schumann resonances at Modra Observatory. *Radio Science*, 42(2).

Pazos, M., Mendoza, B., Sierra, P., Andrade, E., Rodríguez, D., Mendoza, V., and Garduño, R. (2019). Analysis of the effects of geomagnetic storms in the Schumann Resonance station data in Mexico. *Journal of Atmospheric and Solar-Terrestrial Physics*, 193:105091.

Pracser, E. and Bozoki, T. (2021). Schumann-rezonancia-mérések modellezése inhomogén hullámvezetőre. *Magyar Geofizika*, 62(2).

Pracser, E., Bozoki, T., Satori, G., Takatsy, J., Williams, E., and Guha, A. (2021). Two Approaches for Modeling ELF Wave Propagation in the Earth-Ionosphere Cavity With Day-Night Asymmetry. *IEEE Transactions on Antennas and Propagation*, 69(7):4093–4099.

Prácser, E., Bozóki, T., Sátori, G., Williams, E., Guha, A., and Yu, H. (2019). Reconstruction of Global Lightning Activity Based on Schumann Resonance Measurements: Model Description and Synthetic Tests. *Radio Science*, 54(3).

Price, C. (2016). ELF Electromagnetic Waves from Lightning: The Schumann Resonances. *Atmosphere*, 7(9).

Price, C. and Federmesser, B. (2006). Lightning-rainfall relationships in Mediterranean winter thunderstorms. *Geophysical Research Letters*, 33(7).

Price, C. and Melnikov, A. (2004). Diurnal, seasonal and inter-annual variations in the Schumann resonance parameters. *Journal of Atmospheric and Solar-Terrestrial Physics*, 66(13):1179–1185. SPECIAL - Space Processes and Electrical Changes in Atmospheric L ayers.

Price, C., Williams, E., Elhalel, G., and Sentman, D. (2021). Natural ELF fields in the atmosphere and in living organisms. *Int J Biometeorol*, pages 85–92.

Rawat, R., Singh, A. K., Pathan, B. M., Sinha, A. K., Jeeva, K., and Labde, S., e. a. (2012). Diurnal and Seasonal Characteristics of Schumann Resonance. In *39th COSPAR Scientific Assembly*, Mysore, India.

Rees, M. H. (1989). *Physics and Chemistry of the Upper Atmosphere*. Cambridge University Press, Cambridge, UK.

Reeves, G. D., McAdams, K. L., Friedel, R. H. W., and O'Brien, T. P. (2003). Acceleration and loss of relativistic electrons during geomagnetic storms. *Geophysical Research Letters*, 30(10).

Rodger, C. J., Clilverd, M. A., Green, J. C., and Lam, M. M. (2010). Use of POES SEM-2 observations to examine radiation belt dynamics and energetic electron precipitation into the atmosphere. *Journal of Geophysical Research: Space Physics*, 115(A4).

Roldugin, V. C., Maltsev, Y. P., Vasiljev, A. N., Schokotov, A. Y., and Belyajev, G. G. (2004a). Diurnal variations of Schumann resonance frequency in NS and EW magnetic components. *Journal of Geophysical Research: Space Physics*, 109(A8).

Roldugin, V. C., Maltsev, Y. P., Vasiljev, A. N., Schokotov, A. Y., and Belyajev, G. G. (2004b). Schumann resonance frequency increase during solar X-ray bursts. *Journal of Geophysical Research: Space Physics*, 109(A1).

Roldugin, V. C., Maltsev, Y. P., Vasiljev, A. N., Shvets, A. V., and Nikolaenko, A. P. (2003). Changes of Schumann resonance parameters during the solar proton event of 14 July 2000. *Journal of Geophysical Research: Space Physics*, 108(A3).

Said, R. K., Inan, U. S., and Cummins, K. L. (2010). Long-range lightning geolocation using a VLF radio atmospheric waveform bank. *Journal of Geophysical Research: Atmospheres*, 115(D23).

Salinas, A., Toledo-Redondo, S., Navarro, E. A., Fornieles-Callejón, J., and Portí, J. A. (2016). Solar storm effects during Saint Patrick's Days in 2013 and 2015 on the Schumann resonances measured by the ELF station at Sierra Nevada (Spain). *Journal of Geophysical Research: Space Physics*, 121(12):12,234–12,246.

Sato, M. and Fukunishi, H. (2005). New evidence for a link between lightning activity and tropical upper cloud coverage. *Geophysical Research Letters*, 32(12).

Satori, G. (1989). Kvázi real-time digitális mérő-feldolgozó rendszer a Schumann-rezonanciák tanulmányozására. In Bencze, P., editor, *A XVI. Ionoszféra- és Magnetoszféra-fizikai Szeminárium előadásaiból: Bozsok, 1988. október 24-27.*, pages 120–124, Budapest, Hungary. MTESZ Központi Asztronautikai Szakosztály.

Satori, G. (1992). Preliminary results on the studies related to Schumann resonance observations (in Hungarian). In Bencze, P., editor, *A XVII. és a XVIII. Ionoszféra- és Magnetoszféra-fizikai Szeminárium előadásaiból*, pages 165–170, Budapest, Hungary. Magyar Asztronautikai Társaság.

Satori, G. (1993). Schumann resonances and geomagnetic activity. In Weszter-gom, V. and Steiner, T., editors, *On the Automatic Classification of Transient Geomagnetic Variations*, volume 55, pages 201–206. IAGA 7th Sci. Assembly.

Satori, G. (1996). Monitoring Schumann resonances - II. Daily and seasonal frequency variations. *Journal of Atmospheric and Terrestrial Physics*, 58(13):1483–1488.

Satori, G. (2011). *Schumann-rezonancia, mint Globális Változások Jelzőrendszere (in Hungarian).* MTA doctoral dissertation, MTA Geodéziai és Geofizikai Kutatóintézet.

Satori, G., Neska, M., Williams, E., and Szendroi, J. (2007). Signatures of the day-night asymmetry of the Earth-ionosphere cavity in high time resolution Schumann resonance records. *Radio Science*, 42(2).

Satori, G., Rycroft, M., Bencze, P., Märcz, F., Bor, J., Barta, V., Nagy, T., and Kovács, K. (2013). An Overview of Thunderstorm-Related Research on the Atmospheric Electric Field, Schumann Resonances, Sprites, and the Ionosphere at Sopron, Hungary. *Surveys in Geophysics*, 34:255–292.

Satori, G., Szendroi, J., and Vero, J. (1996). Monitoring Schumann resonances - I. Methodology. *Journal of Atmospheric and Terrestrial Physics*, 58(13):1475–1481.

Satori, G., Williams, E., and Lemperger, I. (2009). Variability of global lightning activity on the ENSO time scale. *Atmospheric Research*, 91(2):500–507. 13th International Conference on Atmospheric Electricity.

Satori, G., Williams, E., and Mushtak, V. (2005). Response of the Earth–ionosphere cavity resonator to the 11-year solar cycle in X-radiation. *Journal of Atmospheric and Solar-Terrestrial Physics*, 67(6):553–562.

Satori, G., Williams, E., Price, C., Boldi, R., Koloskov, A., Yampolski, Y., Guha, A., and Barta, V. (2016). Effects of Energetic Solar Emissions on the Earth–Ionosphere Cavity of Schumann Resonances. *Surv Geophys*, 37:757–789.

Satori, G. and Zieger, B. (1996). Spectral characteristics of Schumann resonances observed in central Europe. *Journal of Geophysical Research: Atmospheres*, 101(D23):29663–29669.

Satori, G. and Zieger, B. (1999). El Niňo related meridional oscillation of global lightning activity. *Geophysical Research Letters*, 26(10):1365–1368.

Schlegel, K. and Füllekrug, M. (1999). Schumann resonance parameter changes during high-energy particle precipitation. *Journal of Geophysical Research: Space Physics*, 104(A5):10111–10118.

Schumann, W. O. (1952). Über die strahlungslosen Eigenschwingungen einer leitenden Kugel, die von einer Luftschicht und einer Ionosphärenhülle umgeben ist. *Zeitschrift für Naturforschung A*, 7(2):149–154.

Sentman, D. D. and Fraser, B. J. (1991). Simultaneous observations of Schumann resonances in California and Australia: Evidence for intensity modulation by the local height of the D region. *Journal of Geophysical Research: Space Physics*, 96(A9):15973–15984.

Shvets, A. (2001). A technique for reconstruction of global lightning distance profile from background Schumann resonance signal. *Journal of Atmospheric and Solar-Terrestrial Physics*, 63(10):1061–1074.

Shvets, A. and Hayakawa, M. (2011). Global Lightning Activity on the Basis of Inversions of Natural ELF Electromagnetic Data Observed at Multiple Stations around the World. *Surv Geophys*.

Shvets, A., Hayakawa, M., Sekiguchi, M., and Ando, Y. (2009). Reconstruction of the global lightning distribution from ELF electromagnetic background signals. *Journal of Atmospheric and Solar-Terrestrial Physics*, 71(12):1405–1412.

Shvets, A., Nickolaenko, A., and Chebrov, V. (2017). Effect of Solar Flares on the Schumann-Resonance Frequences. *Radiophys Quantum El*, page 186–199.

Shvets, A. V., Hobara, Y., and Hayakawa, M. (2010). Variations of the global lightning distribution revealed from three-station Schumann resonance measurements. *Journal of Geophysical Research: Space Physics*, 115(A12).

Singh, B., Tyagi, R., Hobara, Y., and Hayakawa, M. (2014). X-rays and solar proton event induced changes in the first mode Schumann resonance frequency observed at a low latitude station Agra, India. *Journal of Atmospheric and Solar-Terrestrial Physics*, 113:1–9.

Sukhov, V., Sukhova, E., Sinitsyna, Y., Gromova, E., Mshenskaya, N., Ryabkova, A., Ilin, N., Vodeneev, V., Mareev, E., and Price, C. (2021). Influence of Magnetic Field with Schumann Resonance Frequencies on Photosynthetic Light Reactions in Wheat and Pea. *Cells*, 10(1).

Suvorova, A. V. (2017). Flux Enhancements of ¿ 30 keV Electrons at Low Drift Shells L ¡ 1.2 During Last Solar Cycles. *Journal of Geophysical Research: Space Physics*, 122(12):12,274–12,287.

Tatsis, G., Christofilakis, V., Chronopoulos, S., Baldoumas, G., Sakkas, A., Paschalidou, A., Kassomenos, P., Petrou, I., Kostarakis, P., Repapis, C., and Tritakis, V. (2020). Study of the variations in the Schumann resonances parameters measured in a southern Mediterranean environment. *Science of The Total Environment*, 715:136926.

Tatsis, G., Sakkas, A., Christofilakis, V., Baldoumas, G., Chronopoulos, S., Paschalidou, A., Kassomenos, P., Petrou, I., Kostarakis, P., Repapis, C., and Tritakis, V. (2021). Correlation of local lightning activity with extra low frequency detector for Schumann Resonance measurements. *Science of the Total Environment*, 787.

Thomas, L. (1971). The lower ionosphere. *Journal of Atmospheric and Terrestrial Physics*, 33(2):157 – 195.

Tikhonov, A. N. and Arsenin, V. Y. (1977). *Methods for Solving Ill-Posed Problems*. John Wiley, New York, USA.

Tinmaker, M., Aslam, M., Ghude, S., and Chate, D. (2017). Lightning activity with rainfall during El Nino and La Nina events over India. *Theor Appl Climatol*, 130:391–400.

Toledo-Redondo, S., Parrot, M., and Salinas, A. (2012a). Variation of the first cut-off frequency of the Earth-ionosphere waveguide observed by DEMETER. *Journal of Geophysical Research: Space Physics*, 117(A4).

Toledo-Redondo, S., Parrot, M., and Salinas, A. (2012b). Variation of the first cut-off frequency of the Earth-ionosphere waveguide observed by DEMETER. *Journal of Geophysical Research: Space Physics*, 117(A4).

Trenberth, K. E., Caron, J. M., Stepaniak, D. P., and Worley, S. (2002). Evolution of El Niño–Southern Oscillation and global atmospheric surface temperatures. *Journal of Geophysical Research: Atmospheres*, 107(D8):AAC 5–1–AAC 5–17.

Tritakis, V., Contopoulos, I., Florios, C., Tatsis, G., Christofilakis, V., Baldoumas, G., and Repapis, C. (2021). Anthropogenic Noise and Its Footprint on ELF Schumann Resonance Recordings. *Frontiers in Earth Science*, 9.

van de Kamp, M., Rodger, C. J., Seppälä, A., Clilverd, M. A., and Verronen, P. T. (2018). An Updated Model Providing Long-Term Data Sets of Energetic Electron Precipitation, Including Zonal Dependence. *Journal of Geophysical Research: Atmospheres*, 123(17):9891–9915.

van de Kamp, M., Seppälä, A., Clilverd, M. A., Rodger, C. J., Verronen, P. T., and Whittaker, I. C. (2016). A model providing long-term data sets of energetic electron precipitation during geomagnetic storms. *Journal of Geophysical Research: Atmospheres*, 121(20):12,520–12,540.

Wait, J. (1996). *Electromagnetic waves in stratified media.* Institute of Electrical and Electronics Engineers, New York, USA.

Welch, P. (1967). The use of fast Fourier transform for the estimation of power spectra: A method based on time averaging over short, modified periodograms. *IEEE Transactions on Audio and Electroacoustics*, 15(2):70–73.

Williams, E. (2016). Comments on: “11-year Cycle in Schumann Resonance Data as Observed in Antarctica”. *Sun and Geosphere*, 1:75–76.

Williams, E., Bozoki, T., Satori, G., Price, C., Steinbach, P., Guha, A., Liu, Y., Beggan, C. D., Neska, M., Boldi, R., and Atkinson, M. (2021). Evolution of Global Lightning in the Transition From Cold to Warm Phase Preceding Two Super El Niño Events. *Journal of Geophysical Research: Atmospheres*, 126(3).

Williams, E., Guha, A., Boldi, R., Christian, H., and Buechler, D. (2019). Global lightning activity and the hiatus in global warming. *Journal of Atmospheric and Solar-Terrestrial Physics*, 189:27–34.

Williams, E., Guha, A., Boldi, R., Satori, G., Koloskov, A., and Yampolski, Y. (2014a). Global Circuit Response to the 11-Year Solar Cycle: Changes in Source or in Medium? In *XV International Conference on Atmospheric Electricity*, Norman, Oklahoma, USA.

Williams, E. and Mareev, E. (2014). Recent progress on the global electrical circuit. *Atmospheric Research*, 135-136:208–227.

Williams, E., Rothkin, K., Stevenson, D., and Boccippio, D. (2000). Global Lightning Variations Caused by Changes in Thunderstorm Flash Rate and by Changes in the Number of Thunderstorms. *Journal of Applied Meteorology*, 39(12):2223 – 2230.

Williams, E. and Satori, G. (2004). Lightning, thermodynamic and hydrological comparison of the two tropical continental chimneys. *Journal of Atmospheric and Solar-Terrestrial Physics*, 66(13):1213–1231. SPECIAL - Space Processes and Electrical Changes in Atmospheric L ayers.

Williams, E. R. (1992). The Schumann Resonance: A Global Tropical Thermometer. *Science*, 256(5060):1184–1187.

Williams, E. R., Mushtak, V., Guha, A., Boldi, R., Bor, J., Nagy, T. G., and Satori, G. (2014b). Inversion of multi-station Schumann resonance background records for global lightning activity in absolute units. In *AGU Fall Meeting*, San Francisco, USA. AGU.

Williams, E. R., Mushtak, V. C., and Nickolaenko, A. P. (2006). Distinguishing ionospheric models using Schumann resonance spectra. *Journal of Geophysical Research: Atmospheres*, 111(D16).

Williams, E. R. and Satori, G. (2007). Solar radiation-induced changes in ionospheric height and the Schumann resonance waveguide on different timescales. *Radio Science*, 42(2).

Wu, Y. J., Chen, A. B., Hsu, H. H., Chou, J. K., Chang, S. C., Lee, L. J., Lee, Y. J., Su, H. T., Kuo, C. L., Hsu, R. R., Frey, H. U., Mende, S. B., Takahashi, Y., and Lee, L. C. (2012). Occurrence of elves and lightning during El Niño and La Niña. *Geophysical Research Letters*, 39(3).

Yang, H., Pasko, V. P., and Satori, G. (2009). Seasonal variations of global lightning activity extracted from Schumann resonances using a genetic algorithm method. *Journal of Geophysical Research: Atmospheres*, 114(D1).

Yang, J., Zhang, Z., Wei, C., Lu, F., and Guo, Q. (2017). Introducing the New Generation of Chinese Geostationary Weather Satellites, Fengyun-4. *Bulletin of the American Meteorological Society*, 98(8):1637 – 1658.

Yoshida, S., Morimoto, T., Ushio, T., and Kawasaki, Z. (2007). ENSO and convective activities in Southeast Asia and western Pacific. *Geophysical Research Letters*, 34(21).

Yuan, T., Di, Y., and Qie, K. (2016). Variability of lightning flash and thunderstorm over East/Southeast Asia on the ENSO time scales. *Atmospheric Research*, 169:377–390.

Zhou, H. and Qiao, X. (2015). Studies of the variations of the first Schumann resonance frequency during the solar flare on 7 March 2012. *Journal of Geophysical Research: Atmospheres*, 120(10):4600–4612.

Zhou, H., Yu, H., Cao, B., and Qiao, X. (2013). Diurnal and seasonal variations in the Schumann resonance parameters observed at Chinese observatories. *Journal of Atmospheric and Solar-Terrestrial Physics*, 98:86–96.